UNIVERSITÀ DEL SALENTO
FACOLTÀ DI SCIENZE MM. FF. NN.

Dott.ssa Maria Rita COLUCCIA

PhD Thesis

# Electron Drift Velocity and Amplification in Resistive Plate Counters (RPC) operating with the ATLAS Gas Mixture

Supervisors:
Prof. Edoardo GORINI

Dott.ssa Margherita PRIMAVERA

Dottorato di Ricerca in Fisica XIX Ciclo
Settore Scientifico FIS/04

# Index

# Introduction

This work is mainly devoted to the measurements of electron transport and amplification properties of the gas mixture used for the Resistive Plate Counters (RPC's) in the ATLAS experiment at the Large Hadron Collider (LHC) under construction at CERN in Geneva, where RPC are employed as muon trigger detectors.

This gas mixture has three components: 94.7 % of Tetrafluoroethane ($C_2H_2F_4$) as main component, 5 % isobutane ($C_4H_{10}$) as photons quencher and 0.3 % $SF_6$, in order to inhibit streamers development and it allows to operate the detector in the so called saturated avalanche mode, instead of the more conventional streamer mode, until now and presently widely adopted by experiments. The reason for operating in this regime is to increase the detector rate capability up to $\sim$1 kHz/cm$^2$ (about one order of magnitude of the usual values reached by RPC operating in streamer), to reduce aging phenomena and to maintain good efficiency and time resolution.

The knowledge of the underlying physical processes in the RPC detectors allows for developing Montecarlo simulations of their behavior to be compared with experimental data. This is crucial in order to predict detector performances and to optimize detector designs. In literature, several authors made Montecarlo simulations of RPC's operating in LHC [1, 2]. In these works the input fundamental gas parameters where extracted by the widely used program MAGBOLTZ [3, 4], that allows to compute them for electron in various gases. In addition, these authors simulated avalanche fluctuations in saturated avalanche regime with ad hoc assumption or by using specific models.

We measured directly the gas parameters and the avalanche fluctuation spectra in RPC ATLAS-like prototypes in Lecce INFN and Physics Departments laboratory. A comparison of the measurement results with MAGBOLTZ calculation has been performed and a satisfying agreement

has been found for both electron drift velocity and effective Townsend's coefficient.

A $N_2$ ($\lambda = 337$ nm) pulsed laser has been used to induce ionization in the RPC prototype gas gap, since the use such source has the advantages to generate primary electron (from a single up to hundred depending on the beam intensity) localized in a small area around a lens focus. All the studies presented here have been performed by using two small size RPC ($10 \times 20$ $cm^2$) prototypes, RPC I and RPC II, having a 2 mm gas gap delimited by 2mm-thick linseed-oil-treated Bakelite plates with a resistivity of about $1.4 \times 10^{11}$ $\Omega$ cm and of about $1.71 \times 10^{10}$ $\Omega$ cm respectively.

The measurement setup has been designed to take advantage of an existing facility, but completely new dedicated Data Acquisition System (DAQ), Detector Control System (DCS) and on-line (offline analysis) software have been implemented.

This thesis is organized in 5 chapters.

The first two chapters are dedicated to the description of the LHC physics programs and to a brief overview of the ATLAS and CMS experiments, with more emphasis in the description of the ATLAS Muon Spectrometer yo which this work is in ultimate analysis finalized; a full description of the RPC detectors structure is presented in chapter 3, together with the physics phenomena underlying their behavior.

Chapters 4 describes the laser ionization technique and its fruitful employment in calibrating gas detectors and the experimental setup in all its components, hardware and software.

Finally, Chapter 5 is dedicated to the discussion of the experimental results.

An appendix reports the quality assurance tests performed on the so called special RPC detectors (S2 and S3) of the barrel trigger system and before their final installation in the ATLAS Muon Spectrometer. This work has been entirely performed at CERN and represents a relevant part of the research activity during PHD period.

# Chapter 1

# The Large Hadron Collider at CERN

## 1.1 The Large Hadron Collider

The Large Hadron Collider (LHC) is the new superconducting proton-proton accelerator [5] currently being installed ∼100 m deep below the countryside of Geneva (Switzerland) at the CERN laboratory (*"Centre Europeenne pour la Recherche Nucleaire"*). It is now in its final installation and commissioning phase and it is made by two coaxial rings housed in the 27 km tunnel previously constructed for the Large Electron Positron Collider (LEP). The accelerator has been designed to provide proton-proton collisions with the unprecedented luminosity $\mathcal{L}$ of $10^{34} cm^{-2} s^{-1}$, where $\mathcal{L}$ is given by the formula:

$$\mathcal{L} = f \frac{N^2}{4\pi\sigma_x\sigma_y} F, \tag{1.1}$$

with: $N$ number of protons per bunch, $f$ bunch collision frequency, $\sigma_x$ and $\sigma_y$ characterize the Gaussian beam transverse profile in the horizontal and vertical directions respectively, $F$ geometric reduction factor due to the beam crossing angle. Proton beams will collide with an energy of 7 TeV per beam, providing a center-of-mass energy of 14 TeV, which is one order of magnitude higher than the one reached in any previous collider. The main design parameters of the LHC machine are shown in table 1.1.

In addition to the p-p operation, LHC will be able to collide heavy nuclei e.g. Pb-Pb with a center-of-mass energy of 2.76 TeV/nucleons at an initial

| | |
|---|---|
| Circumference | 26.7 km |
| Luminosity | $10^{34} cm^{-2} s^{-1}$ |
| Beam energy at collision | 7 TeV |
| Beam energy at injection | 0.45 TeV |
| Dipole field at 7 TeV | 8.33 T |
| Coil aperture | 56 mm |
| Beam current | 0.56 A |
| Protons per bunch | $1.1 \times 10^{11}$ |
| Number of bunch | 2808 |
| Nominal bunch spacing | 24.95 ns |
| Bunch spacing | 7.48 m |
| Normalized transverse emittance | 3.75 $\mu$m |
| R.M.S. bunch length | 75 mm |
| Filling time per ring | 4.3 min |
| Luminosity life time | 10 h |
| Total crossing angle | 300 $\mu$rad |
| Energy loss per turn | 6.7 keV |
| Critical synchrotron energy | 44.1 eV |
| Radiated power per beam | 3.8 kW |
| Stored energy per beam | 350 MJ |
| Stored energy in magnets | 11 GJ |
| Operating temperature | 1.9 $^o$K |

Table 1.1: Main design parameters of the LHC

luminosity of $10^{27} cm^{-2} s^{-1}$.

Two main luminosity scenarios are foreseen for the LHC in p-p operation:

- an initial "low luminosity scenario"with a peak luminosity of about $10^{33} cm^{-2} s^{-1}$, corresponding to an integrated luminosity of $\sim$10 fb$^{-1}$/per year.
- the design "high luminosity scenario"to be reached approximately 3 years after the startup, with a peak value of about $10^{34} cm^{-2} s^{-1}$, corresponding to an integrate luminosity of 100 fb$^{-1}$/per year.

At high luminosity, the beam will be arranged in 2808 bunches of $1.1 \times 10^{11}$ protons per bunch, which will be collide each 25 ns in the interaction

regions (IR). Given a p-p inelastic cross section of about 100 mb at 14 TeV, about 23 p-p interactions per crossing and a total of about 700 charged particles with $P_T > 150$ MeV will be produced.

Fig. 1.1 shows the injection system layout for LHC. Protons are produced and accelerated up to 50 MeV by a proton linac before being injected into the 1.4 GeV Proton Synchrotron Booster (PSB). A Proton Synchrotron (PS) will accelerate protons up to 26 GeV and, finally, the 450 GeV Super Proton Synchrotron (SPS) will inject protons into LHC, where they will be finally accelerate up to 7 TeV.

The high luminosity required excludes the use of an anti-proton beam (which would take several hours to cool and accumulate them before injection) and, consequently, a common vacuum and magnet system for both circulating beams. To collide two beams of equally charged particles requires opposite magnet dipole fields, then LHC is designed as a proton-proton collider with separate magnet fields and vacuum chambers in the main arcs and with common pipes, about 130 m long, at the intersection regions (IR), where the experimental detectors are located. The two beams are separated along the IR in order to avoid parasitic collision points.

Since there was not enough space in the LEP tunnel to accommodate two separate rings of magnets, LHC uses twin bore magnets, which consist of two sets of coils and beam channels within the same mechanical structure and cryostat (see Fig. 1.2). 7 TeV peak beam energy implies a 8.33 T peak dipole field and the use of a superconducting magnet technology.

### 1.1.1 Lattice layout

The layout of LHC ring (see Fig. 1.3) is realized with eight arcs (ARC) and eight long straight sections (LSS). Each straight section is approximately 528 m long and it can serve as an experimental or utility insertion point. The two high luminosity intersection points on the ring are located diametrically opposite: point 1, where the ATLAS experiment will operate, and point 5, where the CMS experiment is installed. Two other experiments, ALICE and LHCb, are respectively located at point 2 and point 8, which also contain the injection system for the two beams. The beams cross from one magnet bore to the other only in correspondence of these four locations. The remaining straight sections are not equipped with beam crossing regions. Insertion points 3 and 7 contain two collimation systems, insertion point 4 contains two Radio Frequency (RF) systems, one system for each beam, and insertion

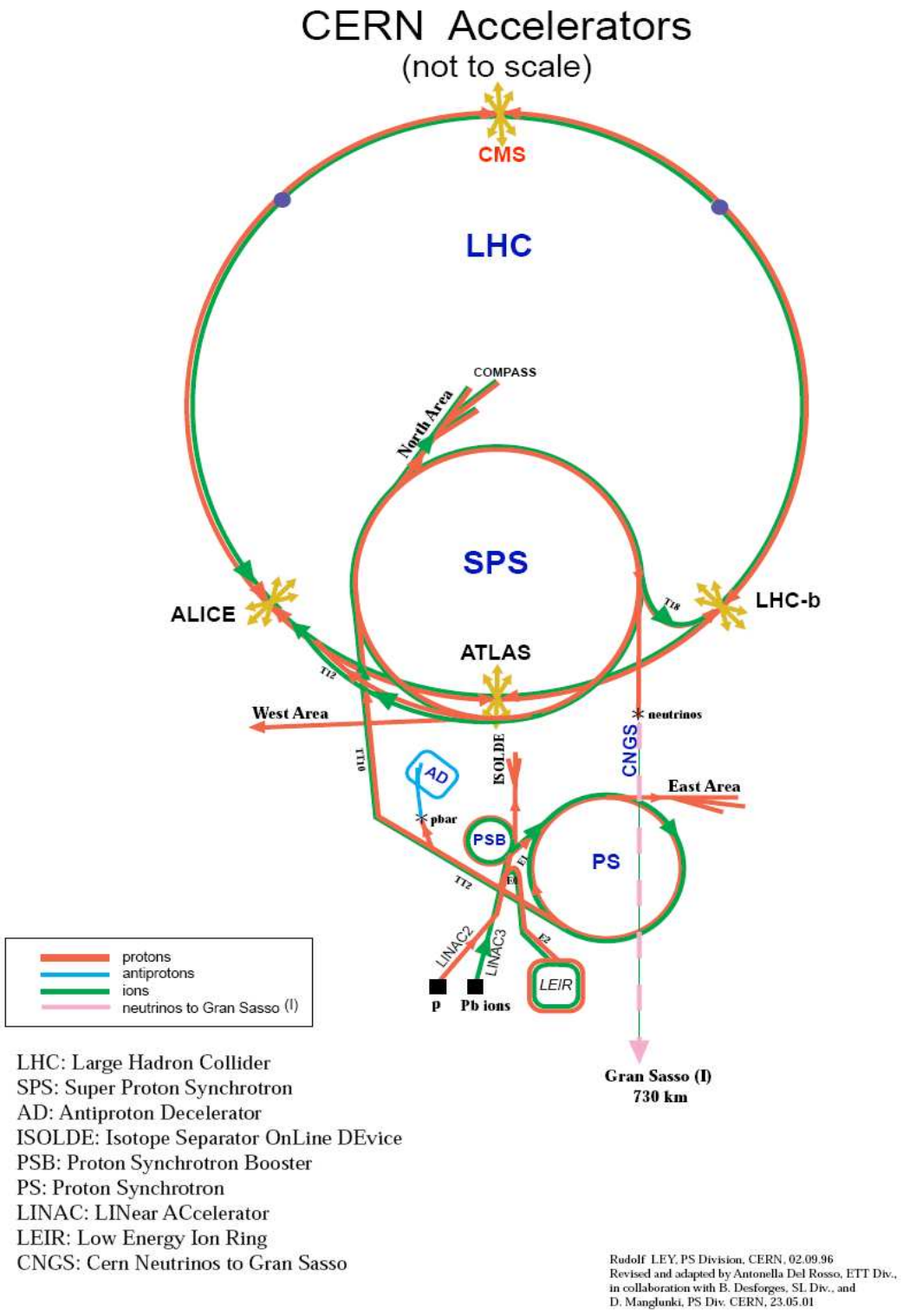


Figure 1.1: *Accelerator complex at CERN*

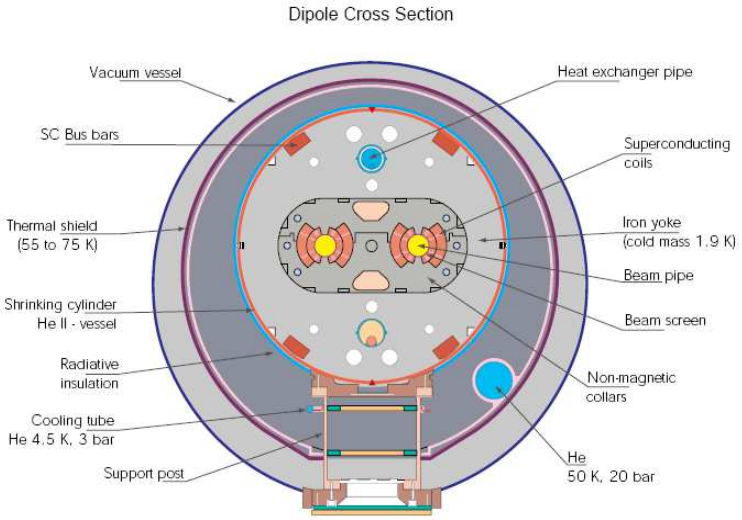


Figure 1.2: *Cross section of a twin-bore magnet for LHC*

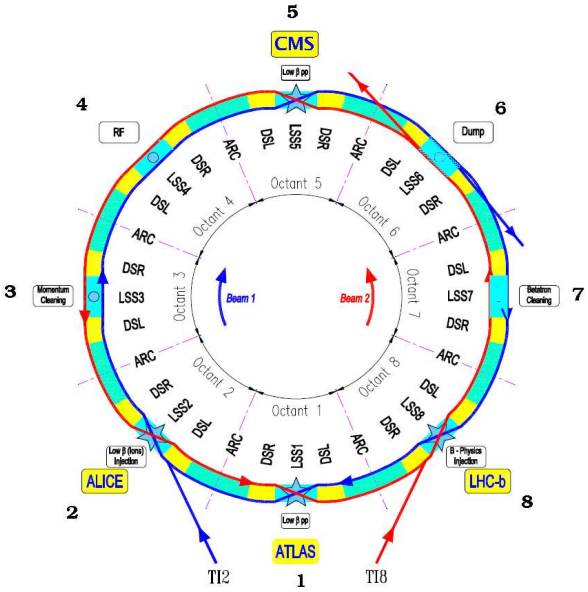


Figure 1.3: *LHC layout scheme*

point 6 contains the beam dumps, ensuring an independent abort system for the two beams.

In order to focus the beams in both horizontal and vertical planes, a succession of focusing and defocusing quadrupole magnets is required: FODO structures. The LHC lattice is composed of 23 regular FODO cells per arc. Each cell is 106,9 m long and is made of six dipoles 15 m long and two short straight sections 6.6 m long containing the main quadrupoles and multipoles correctors.

### 1.1.2 Accelerator Magnets

LHC contains more than 7000 superconducting magnets. The most technologically challenging are the 1232 superconducting dipoles and the 392 quadrupoles in the arcs.

The challenge for the LHC dipole magnets is to have the highest bending strength making use of the well-proven technology based on Nb-Ti superconducting cable. To increase the performance of Nb-Ti, the cooling of the superconductors to a temperature below 2 $^o$K, using super-fluid helium, is required. In such a way, an extra 20% gain is attainable in the central field value, with respect to nowadays operating superconductor accelerators, cooled with super-fluid helium at a temperature slightly above 4.2 $^o$K. On the other hand, at such a low temperature, the superconducting cable heat capacity decreases almost an order of magnitude, making easier to trigger a quench.

### 1.1.3 Radio-frequency Acceleration System

The Radio-Frequency (RF) system provides the longitudinal electric field for proton acceleration and is located at insertion point 4.

It is made of single-cell superconducting cavities with large beam tube very similar to those designed for the high current $e^+e^-$ factories. There are two RF systems (one for each beam), each one composed by eight 400 MHz cavities, which are grouped by four in the two cryogenic modules.

## 1.2 The LHC Physics Program

LHC can be thought as a parton-parton collider with a large spread in collision energy. The effective luminosity of the proton collisions falls off rapidly with the center of mass energy. With an expected proton beam energy of 7 TeV, LHC will study physics at the 1 TeV scale in the parton-parton system, extending the accessible energy range approximately by a factor of ten with respect to the one reached by previous collider.

The fundamental goal is to explore the physics processes underlying the electroweak symmetry breaking. This new high energy regime also offers a unique opportunity to search for New Physics. In addition, the high luminosity and cross sections make the LHC a unique factory for the production of heavy particles like the top quark.

The search for the Higgs boson [6], responsible of the mass generation mechanism in the Standard Model (SM), has motivated much of the design of the two general purpose experiments at LHC. Our knowledge about the SM Higgs boson can be summarized as follows:

- its mass is not specified by the theory, which provides only an upper bound of $\sim 1$ TeV;
- direct searches performed at LEP have set a lower limit of $m_H > 114.4$ GeV [7];
- a global fit of the SM parameters to the data collected by various machines (LEP, Tevatron, SLC) gives a 95% C.L. upper bound on $m_H$ of about 250 GeV [8];
- the current experimental knowledge favor a light Higgs boson.

### 1.2.1 Higgs Search

#### SM Higgs

The Higgs production is an electroweak process and the cross section is small. Therefore, the search involves either low rates or low signal-to-background ratios. Fig.1.5 shows the expected p-p production cross-sections at LHC for the SM Higgs boson as a function of its mass. There are several Higgs production mechanisms at LHC, but the most important are the gluon-gluon fusion ($gg \rightarrow H$) and vector boson fusion $qq \rightarrow qqH$ at very high mass (see Fig.

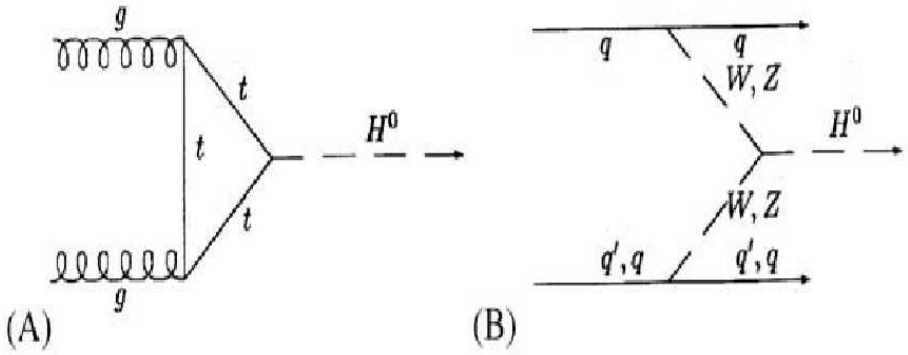


Figure 1.4: *EMain Feynman diagrams contributing to the production of a SM Higgs boson at LHC: (a) g-g fusion, (b) WW and ZZ fusion.*

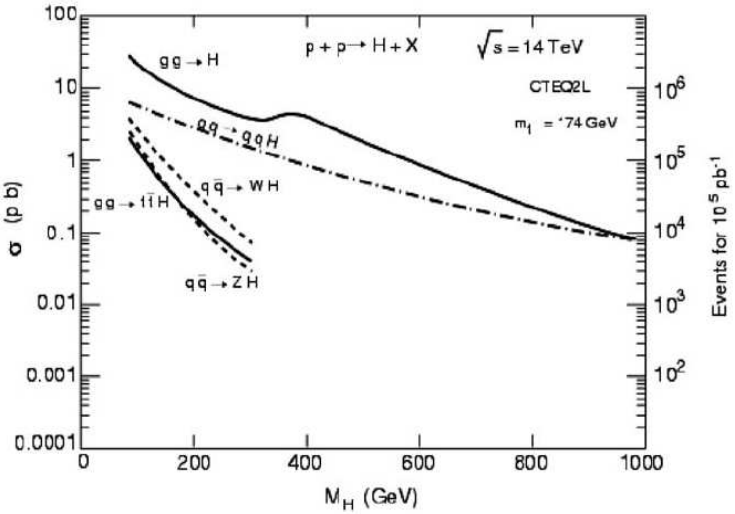


Figure 1.5: *Expected production cross-sections for the SM Higgs boson at LHC as a function of its mass, for the expected production processes.*

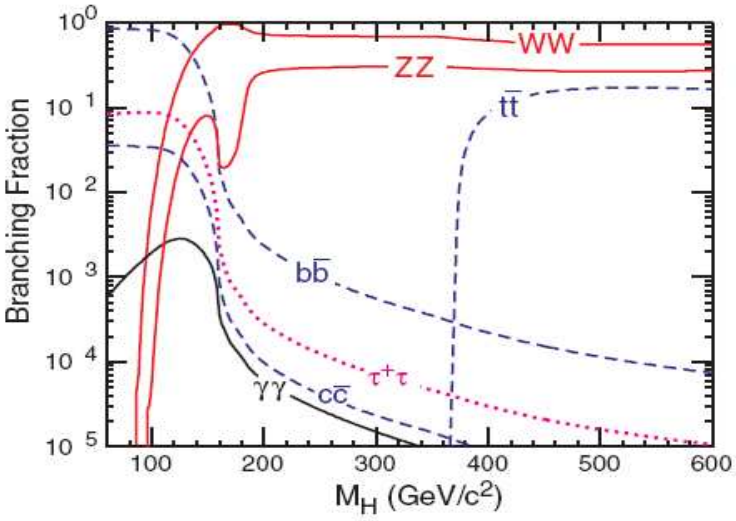


Figure 1.6: *Branching ratios of the Standard Model Higgs boson decay channels as a function of its mass.*

1.4). The searches mainly relies on different final states according to the Higgs mass (see Fig. 1.6). The most important ones are: $\gamma\gamma$ in the low mass region, $4\ell$ in the intermediate and high mass region and $2\ell\nu\overline{\nu}$ at very high mass.

LHC at full luminosity will be able to probe the entire range of Higgs masses from the lower limit set by LEP up to the value where the Higgs is so large that is inappropriate to speak of an elementary field. Failure to find a Higgs boson over this range would seriously compromise the Standard Model as it is.

**Low-mass Higgs**

Just above the LEP limit, the Higgs mainly decays to $b\overline{b}$, but it is practically hopeless to identify the signal amongst the very copious production of $b\overline{b}$ from standard QCD processes. For this reason, the most promising channel is the decay to $\gamma\gamma$, which has a tiny branching ratio but a very narrow mass peak above the smooth QCD background (see Fig. 1.7).

Excellent photon energy and angular resolutions are thus required to observe this signal. These requirements drive the very high-quality electromagnetic calorimetry of both ATLAS and CMS experiments. For an integrated luminosity of 100 fb$^{-1}$ it is possible to discover the SM Higgs up

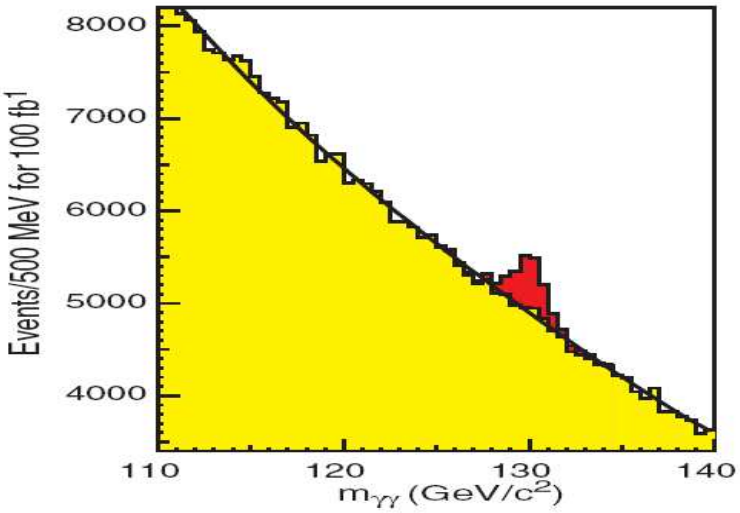


Figure 1.7: *Simulated invariant mass distribution of the $\gamma\gamma$ candidates with a Higgs boson mass of 130 GeV at 100 fb$^{-1}$ from the CMS experiment.*

to a mass of about 140 GeV ($5\sigma$ significance). A signal can also be observed over a more limited mass range for an integrated luminosity of 10 fb$^{-1}$.

**Intermediate-mass Higgs**

In the range from 130 GeV to $2M_Z$ the decay $H \rightarrow ZZ^* \rightarrow 4l$ is used. The event rate is small and the background reduction is difficult since one of the $Z$ is off-shell. In this mass region the Higgs natural width is small ($\leq$ 1GeV), then lepton energy and momentum resolutions are important. The irreducible background arise from the continuum $ZZ^{(*)}/Z\gamma^{(*)}$ production. The reducible background $t\bar{t}$ can be suppressed by lepton isolation and by lepton pair invariant mass cuts, while the reducible background $Zb\bar{b}$ can be suppressed by isolation requirements. The signals obtained are very significant (Fig. 1.8): ATLAS expects signals at the level of 10.3 (7.0), 22.6 (15.5) and 6.5 (4.3) standard deviation respectively for $M_H$ = 130, 150, and 170 GeV in 100 fb$^{-1}$ (30 fb$^{-1}$).

The decay $H \rightarrow WW^{(*)} \rightarrow l^+\nu l^-\overline{\nu}$ can provide valuable information in the mass region around 170 GeV where the four-leptons mode branching ratio has a deep minimum. The dominant background arises from the production of $W$ pairs surviving the cuts to remove the $t\bar{t}$ background.

**High-mass Higgs**

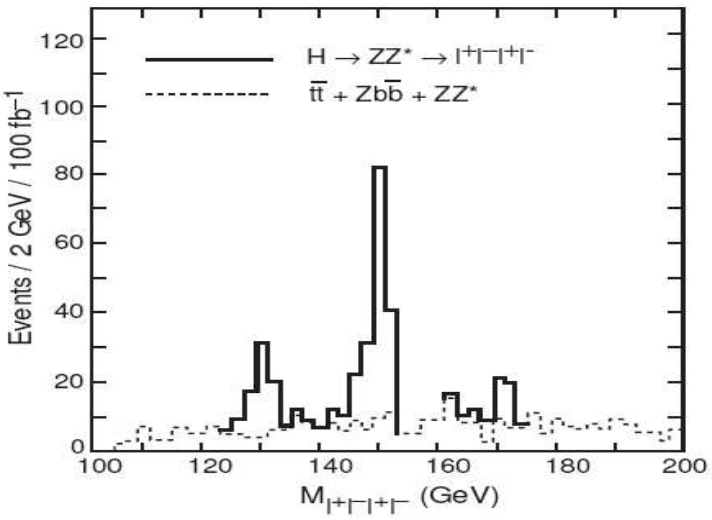


Figure 1.8: *Simulated 4-leptons invariant mass distribution for various Higgs masses (130, 150 and 170 GeV) with the sum of all backgrounds for 100 fb$^{-1}$ in ATLAS.*

The "golden" decay mode $H \rightarrow ZZ \rightarrow 4l$ has a signal excess of six standard deviation over a wide range of Higgs masses from $2M_Z$ to about 600 GeV at 100 fb$^{-1}$.

Electron and muon resolutions and selection cuts are similar as for the $ZZ^*$ channel. As the Higgs mass is increased, its width increases and its production rate falls. Decay channels with larger branching fraction are $H \rightarrow WW/ZZ \rightarrow ll/\nu\overline{\nu} + jets$. The enormous $W + jets$ and $Z + jets$ background must be reduced tagging on one or two forward jets associated to the boson fusion production.

### MSSM Higgs

The Minimal Supersymmetric Model (MSSM) [9] represents the most simple extension of the SM to the Supersimmetry theories. It expects three neutral (h,H and A) and one charged ($H^{\pm}$) Higgs bosons since the model needs two Higgs doublets to generate masses. In the MSSM two parameters are needed to fix the Higgs sector. Usually, they are taken to be the A mass and the ratio $\tan\beta = v_1/v_2$ of the vacuum expectation values of the two Higgs fields.

The phenomenological consequences of these parameters are:

- if $\tan\beta$ is $\mathcal{O}(1)$, the coupling of the top quarks to Higgs bosons is much larger than that of the bottom quarks as is the case of the Standard Model;
- the charged Higgs boson $H^{\pm}$ is heavier than $A$ ($M_H^2 \sim M_A^2 + M_W^2$);
- $H$ is heavier than $A$ and, at large value of $M_A$, the two bosons, $A$ and $H$ are almost degenerate;
- the mass of the lightest boson, $h$, increases with the mass of $A$ and reaches a plateau for $A$ heavier than about 200 GeV;
- in the limit of large mass $A$, the couplings of $h$ become like those of the SM Higgs (decoupling limit);
- the couplings of $A$ and $H$ to charge 1/3 quarks and leptons are enhanced at large $\tan\beta$ relatively to those of a SM Higgs boson of the same mass;
- $A$ does not couple to gauge boson pairs at lowest order and the coupling of $H$ to them is suppressed at large $\tan\beta$ and large $M_A$.

The decay modes used above in the case of the Standard Model Higgs boson can also be exploited in the SUSY Higgs case. $h$ can be searched in the final state $\gamma\gamma$, as the branching ratio approaches that for the Standard Model Higgs for large $M_A$ values, and in $h \to b\overline{b}$. The decay $A \to \gamma\gamma$ can also be exploited. This has the advantage that, because $A \to ZZ, WW$ do not occur, the branching ratio is large enough for the signal to be usable for values of $M_A$ less than $2m_t$ [10].

The decay $H \to ZZ^*$ can be exploited but, at large values of $M_H$, the decay $H \to ZZ$, which provides a very clear signal for the Standard Model Higgs, is useless owing to its very small branching ratio.

In addition to these decay channels, several other possibilities are open up due to the larger number of Higgs bosons and possibly enhanced branching ratios. The most important are the decays of $H/A$ to $\tau^+\tau^-$ (strongly enhanced if $\tan\beta$ is large) and $H/A$ to $\mu^+\mu^-$ (suppressed by a factor $(m_\mu/m_\tau)^2$ but with better resolution than $H/A$ to $\tau^+\tau^-$), $H \to hh$, $A \to Zh$ and $A \to t\overline{t}$.

#### Search for Charged Higgs

It is possible to search for Charged Higgs. The decay $t \to bH^{\pm}$ may compete with the standard $t \to bW^{\pm}$ if it kinetically allowed. The $H^{\pm}$ decays to $\tau\nu$ or $c\overline{s}$ depend on the value of the $\tan\beta$. Over most of the range $1 < \tan\beta < 50$, the decay mode $H^{\pm} \to \tau\nu$ dominates. The signal for $H^{\pm}$ production is thus an excess of tau's produced in the $t\overline{t}$ events.

### 1.2.2 New Physics Search

#### Strong EWSB Dynamics

The precision electroweak measurements are consistent with a light Higgs boson but ElectroWeak Symmetry Breaking (EWSB) by new strong dynamics at the TeV scale cannot be excluded.

The couplings of longitudinally polarized gauge bosons at low energy will violate $WW$ scattering amplitude unitarity around 1.5 TeV at which point new physics must enter. In the Standard Model and its minimal supersymmetric version, this is the perturbative coupling of the Higgs bosons. If no Higgs-like particle exists, then 1 TeV non-perturbative dynamics must enter in the vector boson scattering amplitudes or new meson-like resonances (Technicolor).

In case of strongly interacting WW, WZ and ZZ, the signal appears as an excess of events over the Standard Model prediction of gauge boson pairs at large invariant mass. The favorite channel is $q\overline{q} \to W^{\pm}W^{\pm}$, which doesn't have standard model background and the charge misidentification probability is negligible.

In case of Technicolor [11], theories predict Techni-resonances decay into vector boson pairs (or its longitudinal components) and quark pairs. These signals are striking since they are produced with large cross sections. There are several signals to look for resonance mass peaks, such as Techni-rho ($\varrho_T \to WZ \to 3l\nu$, $\varrho_{T8} \to jet - jet$ and $\varrho_T \to W(\ell\nu)\pi_T(b\overline{b})$) and Techni-mesons ($\eta_T \to t\overline{t}$).

#### Supersymmetry (SUSY)

If SUSY is relevant to electroweak symmetry breaking, gluino and squarks masses are less than $\mathcal{O}(1$ TeV), although squarks might be heavier [12]. As

many supersymmetric particles can be produced simultaneously at the LHC a model must be picked-up to simulate the events:

- SUGRA model [13] assumes that gravity is responsible for the mediation of supersymmetry breaking and provides a natural candidate for cold dark matter;
- GMSB model [14] assumes that the gauge interactions are responsible for the mediation of supersymmetry breaking and explains why flavour changing neutral current effects are small;
- AMSB model assumes that anomaly mediation of supersymmetry breaking, which is always present [15], is dominant.

Gluinos and squarks usually dominate the LHC SUSY production cross section, which is of the order of 10 pb. Since these are strongly produced, it should be easy to separate SUSY from Standard Model backgrounds. In the minimal SUGRA (mSUGRA) model decays produce transverse missing energy $\not\!\!E_T$ from the undetected neutralino $\tilde{\chi}^0{}_1$'s (Lightest Supersimmetric Particle, LSP), multiple jets and several numbers of leptons from the intermediate gauginos. A typical distribution featuring these signatures is the one of the "effective mass":

$$M_{eff} = \not\!\!E_T + \sum_{i=1}^{4} p_{T,i} \tag{1.2}$$

computed from the missing transverse energy and four the hardest jets in the event (see Fig. 1.9).

GMSB models can give in the event additional photons or leptons or long-lived sleptons with high $p_T$ but $\beta < 1$, making the search easier. For $R$-parity violating [1] model the decay $\tilde{\chi}^0{}_1 \rightarrow qqq(lll)$ gives signals at the LHC with very large jet and leptons multiplicity. In all cases, SUSY can be discovered at the LHC if the sparticle masses are in the expected range, and simple kinematic distributions can be used to estimate the approximate mass scale [16].

[1] $R$-parity is a multiplicative quantum number defined as $R = (-1)^{2S+3B+L}$, where $S$ is the spin, $B$ is the baryon number and $L$ is the lepton number. All SM particles have R=1, while superpartners have R= -1. If $R$-parity is conserved, than a single SUSY particle cannot decay into just SM particles. In this case, LSP is absolutely stable. Anyway, it is possible that either baryon number or lepton number is violate, allowing the LSP to decay.

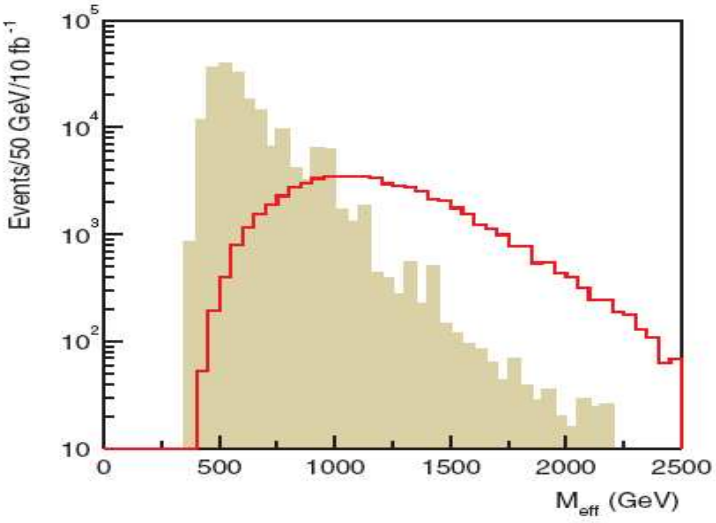


Figure 1.9: *Distribution [17] of $M_{eff}$ for a SUGRA point with gluino and squarks masses of about 700 GeV (lined histogram) and for the total Standard Model background (shaded histogram).*

### Compositeness

If leptons and/or quarks are composite objects at a scale $\Lambda < 30$ TeV [18], than deviations of angular distributions of Drell-Yan dilepton and QCD dijet from standard model predictions will be observed at LHC. Systematic effects like theoretical QCD uncertainties (10% level) and detector effects (20% level due to the energy resolution and nonlinearities) will dominate this type of measurements.

### New Gauge Bosons

There are strong motivations to search for additional $W'$ and $Z'$ bosons, like those predicted in superstring theories [19]. Leptonic decays of these bosons lead to particularly clean signatures and forward-background asymmetry of the charged leptons in the final state would provide important information on its nature. For standard model couplings, sensitivity up to a mass of the new bosons of 6 TeV is get with an integrated luminosity of 100 fb$^{-1}$.

# Chapter 2

# Experiments at LHC and the ATLAS Muon Spectrometer

In the previous chapter the primary motivations to investigate physics at the TeV scale with the Large Hadron Collider have been described. Two out of four LHC detectors, ATLAS[16] and CMS[20], have been designed to exploit the full potential of the collider. Next sections are dedicated to a synthetic description of these two experiments, with the main focus on ATLAS Muon Spectrometer, which is strictly related to the work described in this thesis. The other two LHC experiments are: LHCb[21] a dedicated $B$-physics experiment designed to study CP violating and other rare phenomena in decays of hadrons with heavy flavours, in particular B mesons; ALICE[22] a dedicated heavy ions experiment designed to study the physics of strongly interacting matter and quark-gluon plasma in nucleus-nucleus collision.

## 2.1 Experimental challenges at LHC

The proton-proton inelastic cross-section at $\sqrt{s} = 14$ TeV is roughly 100 mb. At the design luminosity of $10^{34}$ cm$^{-2}$s$^{-1}$ general-purpose detectors will therefore observe an event rate of $6.5 \times 10^8$ inelastic events/s. This leads to a number of formidable experimental challenges[23].

The event selection process ("trigger") must reduce the $\sim$ billion interactions/s to no more than $\sim 10^2$ events/s, for storage and subsequent analysis. The short time between bunch crossings, 25 ns, has major implications for the design of the readout and trigger system. It is not feasible

to make a trigger decision in this 25 ns, then new events may occur on every crossing and, in order to avoid dead-time in the interval taken to make a decision, *pipelined* trigger processing and readout architectures are required where data from many bunch crossing are processed concurrently by a chain of processing elements. The first ("Level-1") trigger decision takes about 3 $\mu$s. During this time, more than 50% of which spent in signal transmission, the data must be stored in pipelines.

At the design luminosity a mean of 20 minimum-bias events will be superimposed on the event of interest. This implies that around 1000 charged particles will emerge from the interaction region every 25 ns. The product of an interaction under study may be confused with those from other interactions in the same bunch crossing. This problem, known as *pileup*, clearly becomes more severe when the response time of a detector element and its electronic signal is longer than 25 ns. The effect of pileup can be reduced by using highly granular detectors with good time resolution, giving low *occupancy* at the expense of having large number of detector channels. The resulting millions of detector electronic channels require very good synchronization.

The particles coming from the interaction region lead to high radiation levels in the experimental area requiring radiation-hard detectors and front-end electronics.

Access for maintenance will be very difficult, time consuming and highly restricted. Hence, a long-term operational reliability is required.

The on-line trigger system has to analyze information that is continuously generated at a rate of 40,000 $\mathrm{Gbs}^{-1}$ and reduce it to hundreds of $\mathrm{Mbs}^{-1}$ for storage. The many petabytes of data that will be collected per year per experiment have to be distributed for offline analysis to scientists located across the globe. Data management problems deriving from this, have motivated the application in this field of the Computing Grid techniques [24], with specific developments for LHC experiments [25].

## 2.2 General Purpose Experiments at LHC

ATLAS and CMS experiments are progressing in their construction to be ready to take collision data in the spring 2008. Most of the experimental challenges come from the industries, that are trying to meet the schedules from mass-production of components with the stringent quality requirements

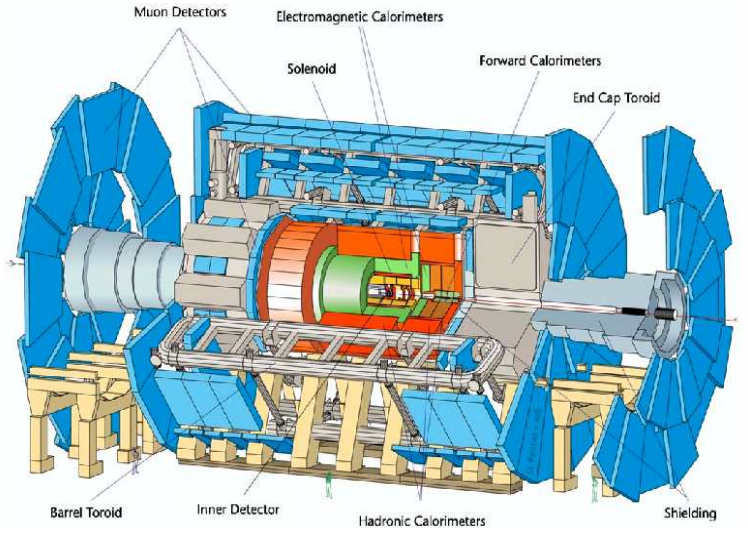


Figure 2.1: *A 3-D view of the ATLAS detector displaying the various sub-detectors.*

on these components.

Important aspect of the detector designs and layouts is their magnetic field configuration for the measurement of the muon momentum. Large bending power is needed to measure precisely the momentum of charged particles, forcing a choice of superconducting technology. In the following the two experiments will be briefly described, then we shall focus on the ATLAS Muon Spectrometer which is related to this thesis work.

### 2.2.1 A Toroidal LHC Apparatus (ATLAS)

The overall detector layout is shown in Fig.2.1 [16]. The magnet system of the muon spectrometer consists of large superconducting air-core toroids consisting of independent coils arranged with an eight-fold symmetry outside the calorimetry, while magnet field for the inner tracking is provided by a "thin" superconducting solenoid generating a field of 2T.

The inner tracking detector [26] has a cylindrical length of 6.8 m and of radius 1.15 m. It comprises combination of few layers of high resolution Si pixel and micro-strip detectors in the inner part and many layers of straw-tube tracking detectors with transition radiation capability in the outer part

of the tracking volume.

Highly granular lead/liquid-argon (LAr) sampling electromagnetic calorimetry covers the pseudo-rapidity range $\mid \eta \mid < 3.2$. A novel absorber/electrode layout, named 'accordion', has been developed. In the end-caps, a copper/LAr sampling structure is used for the hadronic calorimeter (HCAL). The forward tungsten/LAr calorimeter, extending the coverage to $\mid \eta \mid = 4.9$, is also housed in the same cryostat of the end-cap electromagnetic calorimeter (ECAL). The barrel part of the hadronic calorimetry is provided by Fe/scintillator-tile sampling calorimeter using a wavelength-shifting (WLS) fibers readout. The scintillator tiles are also arranged in a novel way, in planes perpendicular to the beam line. Calorimetric system is surrounded by the muon spectrometer. A detailed description of the muon system will be presented in sec. 2.3.

The air core toroid system encloses a large field volume. The muon chambers, grouped into three stations, are placed in an open and light structure to minimize the effect of multiple scattering. A significant challenge, for ATLAS and indeed the other LHC muon detectors, is the manufacture of chambers covering a very large area (muon spectrometer in ATLAS has a total surface of about 10,000 $m^2$) and the high precision desired in the measurements (ATLAS requires a precision of 80 $\mu$m/measured point) over a large volume. Quality control during chamber manufacture and precise alignment during run are therefore critical.

The muon spectrometer defines the overall dimensions of the ATLAS detector, with a diameter of 22 m and a length of 46 m. The weight of the detector is about 7000 tons.

### 2.2.2 The Compact Muon Solenoid (CMS)

The overall layout of CMS is shown in Fig.2.2. In the center of CMS experiment sits a 13 m-long, 5.9 m inner diameter, 4T superconducting solenoid. In order to achieve good momentum resolution within a compact spectrometer, without making stringent demands on muon-chamber resolution and alignment, an high magnetic field was chosen. The return field is large enough to saturate 1.5 m of iron, which accommodates four muons stations. Each muon station consists of several layers of aluminum drift tubes (DT) in the barrel region and Cathode Strip Chambers (CSC) in the end-cap region complemented by Resistive Plate Chambers (RPC).

The bore of the magnet coil is also large enough to accommodate the

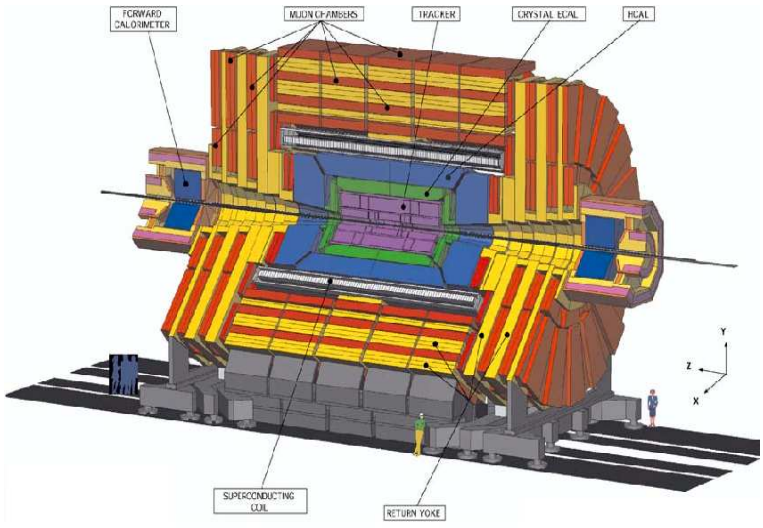


Figure 2.2: *A 3-D view of the CMS detector displaying the various sub-detectors.*

inner tracker and the calorimetry inside. The tracking volume is given by a cylinder of 6 m length and 2.6 m diameter. In order to deal with high track multiplicity, CMS employs ten layers of silicon micro-strip detectors which provide the required granularity and precision. As in ATLAS, silicon pixel detectors placed close to the interaction region improve the measurements of the impact parameter of charged-particle tracks as well as the position of secondary vertexes. The EM calorimeter (ECAL) uses lead tungstate ($PbWO_4$) crystals. The scintillation light is detected by novel Si avalanche photo-diodes in the barrel region and vacuum photo-triodes in the end-cap region. The ECAL is surrounded by a brass/scintillator sampling hadron calorimeter. The scintillation light is covered by WLS fibers embedded in the scintillator tiles and channeled to photo-detectors via clear fibers. The light is detected by novel photo-detectors (hybrid photo-diodes) that can provide gain and operate in high axial magnetic fields. Coverage up to pseudo-rapidity of 5.0 is provided by an iron/quartz-fiber calorimeter. The Cerenkov light emitted in the quartz fibers is detected by photo-multipliers. The forward calorimeters ensure full geometric coverage for the measurement of the transverse energy in the event.

The overall dimensions of the CMS detector are length of 21.6 m, a

diameter of 14.6 m and a total weight of 12,500 tons.

## 2.3 The ATLAS Muon Spectrometer

The ATLAS Muon Spectrometer[27] design, based on a system of three large superconducting air core toroids, was driven by the need of having a very high quality stand-alone muon measurement, with large acceptance both for muon triggering and measuring, to achieve the physics goals discussed in the first chapter. Precision tracking in the Muon Spectrometer is guaranteed by the use of high precision drift and multi-wire proportional chambers. Great emphasis has been given in the design phase to system issues such as the alignment of the tracking detectors. Triggering is accomplished using dedicated fast detectors, that allow bunch crossing identification, with limited spatial accuracy. These detectors provide also the measurement of the coordinate in the non-bending plane.

In the following sections we shall discuss the spectrometer design, the trigger system and the tracking system with their different detector technologies.

### 2.3.1 The Muon Spectrometer Design

As discussed in the first chapter, the experiments at LHC have a very rich physics potential e.g. the discovery of the Higgs bosons, the discovery of new supersymmetric particles, and accurate study of the CP violation in the Beauty sector[28]. Most of these processes imply the presence of muons in the final states and the ATLAS Muon Spectrometer is an essential device to enhance the discovery potential of the experiment. The momentum range spanned by the muons produced in the interesting reactions is very wide, going from few GeV/c of the muons produced in $B$ decays to TeV/c of muons produced in new heavy gauge bosons decays. Then the muon system has to satisfy the following requirements:

- a transverse-momentum resolution of 1% in the low $p_T$ region. This limit is set by the requirements to detect the $H \rightarrow ZZ^*$ decay in the muon channel with high background suppression;
- at the highest $p_T$ the muon system should have sufficient momentum resolution to give good charge identification for $Z' \rightarrow \mu^+\mu^-$ decay;

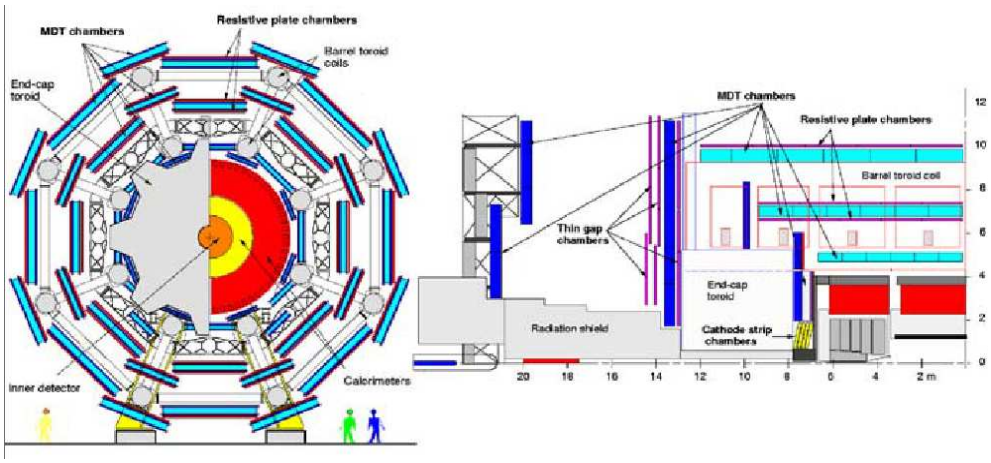


Figure 2.3: *Conceptual design of the ATLAS Muon Spectrometer*

- a pseudo-rapidity coverage $|\eta|<3$. This condition guarantees a good detection efficiency for high-mass objects decaying into muons with all of them within the acceptance region;
- an hermetic system to prevent particles escaping through detector cracks;
- a 3-dimensional measurement of spatial coordinates;
- a low rate of both punch-through hadrons and fake tracks;
- a trigger system for almost all physics channels. For B physics a maximal coverage for muons with transverse momentum down to 5 GeV is required.

The spectrometer design has been optimized to reach an high stand-alone resolution and robust muon identification and it is illustrated in Fig.2.3.

Fig.2.4a shows the different contributions to the muon transverse momentum resolution. For momenta below 10 GeV/c, the fluctuation on the energy loss of muons in the calorimeters limits the resolution to about 6-8%. For momenta up to 250 GeV/c the multiple scattering in the materials, present in the spectrometer, limits the resolution to about 2%, while for higher momenta, the spatial accuracy of the chambers and the knowledge of their calibration and alignment give the largest contribution to the resolution.

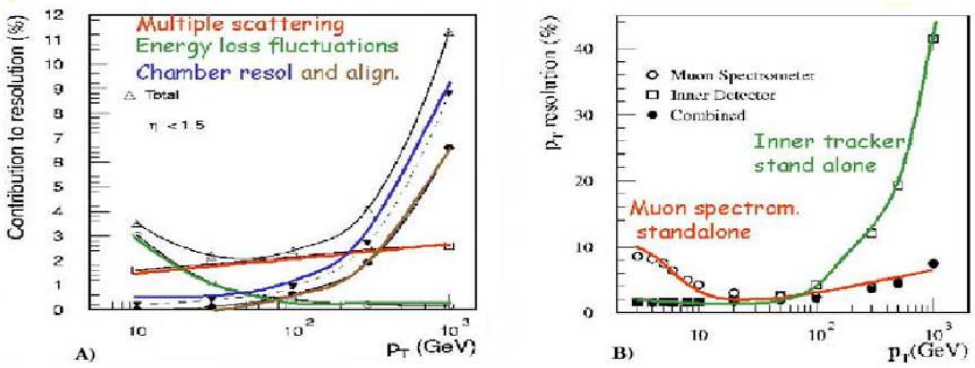


Figure 2.4: **a** *Resolution as a function of the muon momentum for the stand-alone Muon Spectrometer. Also displayed are the different contribution to the resolution.* **b** *Resolution as a function of the muon momentum for the stand-alone Muon Spectrometer, stand-alone Inner tracker and combined measurement.*

A 1 TeV/c momentum muon is measured with 10% resolution, which was one of the more stringent requirements on the spectrometer design. Muon momentum resolution at low momenta (below 100 GeV/c) is improved by using a combined reconstruction of the muon trajectory exploiting the Inner Tracker measurement. In this case the Muon Spectrometer is used mainly for the identification of the muon. In Fig.2.4b the measurements in the Inner Detectors are included for the over-all determination of the transverse momentum: the resolution of the muon spectrometer dominates for $p_T >$ 50 GeV/c. In ATLAS the muon momentum is measured with a precision of about 2% up to 250 GeV/c.

The spectrometer is divided into three regions: Barrel, in the rapidity region $\mid \eta \mid \leq 1.$ and two End-Caps, covering the rapidity regions $1<\mid \eta \mid <2.7$. In the Barrel, the toroidal field is produced by eight very large superconducting coils arranged in a open geometry. The field integral in the Barrel varies between 2 and 5 T m, with large variation as a function of the azimuth angle. The muon momentum is obtained measuring the sagitta of the muon trajectory produced by the magnetic field. The muon trajectory is sampled in three high precision measuring stations placed inside the toroid, equipped with Monitored Drift Tubes (MDT, see Sec.2.3.2) and arranged in three cylindrical layers around the beam axis. Each station measures the

muon positions with a precision of about 50 $\mu$m. In the two outer stations of the Barrel spectrometer, specialized trigger detectors (Resistive Plate Counters, RPCs) are present. An exhaustive description of these detectors will be presented in the next chapter. In the middle station two layers, each comprising two RPC detectors (RPC doublet), are used to form a low $p_T$ trigger ($p_T$>6 GeV/c). In the outer station only one layer with a RPC doublet is used to form the high $p_T$ trigger ($p_T$>20 GeV/c), together with the low $p_T$ station. The RPCs measure both the bending and non-bending coordinate in the magnetic field. Trigger formation requires fast (< 25 ns) coincidences pointing to the interaction region both in the bending and in the non-bending planes.

In the End-Cap regions, two identical air core toroids are placed inside the barrel toroid with the same axis (corresponding to the beam direction). The measurement of the muon momentum is accomplished using three measuring stations of chambers mounted to form three big disks called 'wheels', normal to the beam direction and measuring the angular displacement of the muon track when passing in the magnetic field (the toroids are placed between the first and the second tracking stations). In this case the toroids' volume is not instrumented: a sagitta measurements is not possible and a point-angle measurement is performed. MDT chambers are used for precise tracking in the full angular acceptance, with the exception of the inner station where the region 2<| $\eta$ |<2.7 is equipped with Cathode Strip Chambers (CSC, see Sec.2.3.2) which exhibit a smaller occupancy. The CSCs have spatial resolution in the range of 50 $\mu$m.

The trigger acceptance in the End-Cap is limited to | $\eta$ |<2.4 where Thin Gap Chambers (TGC, see sec.2.3.3) are used to provide the trigger. The TGCs are arranged in two stations: one made of two doublets of two layers each, used for the low $p_T$ trigger, and one made of three layers used in the high $p_T$ trigger in conjunction with the low $p_T$ stations. The high $p_T$ station is placed in front of the middle precision tracking wheel and the low $p_T$ station is behind it. The TGCs provide also the measurement of the second coordinate and for this reason there is a TGC layer also in the first tracking wheel.

One of the main concern comes from the background. The main source in the ATLAS Muon Spectrometer is the large number of photons and neutrons, with energy typically below 1 MeV and 100 KeV respectively, which interact in the active volume of the tracking and trigger detectors. Typical fluence values in the Barrel sector are below 20 Hz/cm$^2$ for almost all the chambers,

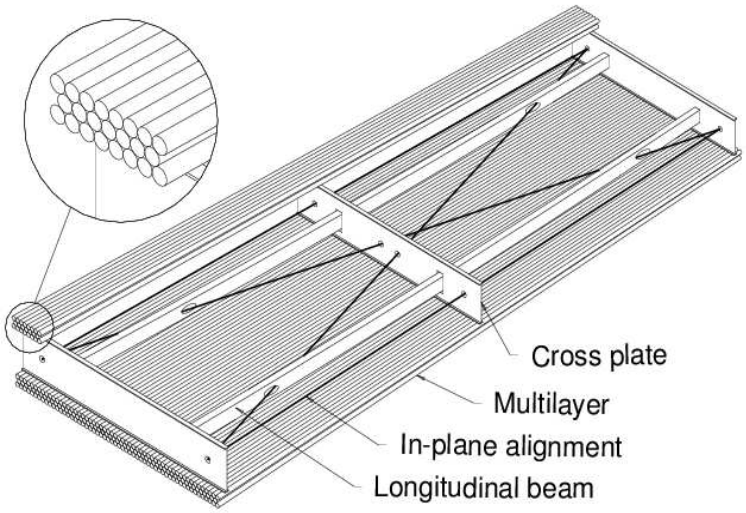


Figure 2.5: *Scheme of a Monitored Drift Tube chamber*

but it increases fast with rapidity: fluences of the order of 1 kHz/cm$^2$ are foreseen at the largest rapidity. Increasing by a factor 20 is expected in the inner stations of the End-Cap. The corresponding hit rates for the tracking detectors are expected to be roughly in the range of 20-500 Hz/cm$^2$, and they impose constraints on the detector design, both in terms of performance (efficiency and resolution) and long-term stability (aging).

### 2.3.2 Tracking Chambers

#### Monitored Drift Tubes: MDT

The precision tracking is performed, in almost all the spectrometer, by the Monitored Drift Tubes (MDTs). The basic detection element is an aluminum tube of 30 mm diameter and 400 $\mu$m wall thickness, with a 50 $\mu$m diameter central W-Re wire [29]. The lengths of the tubes vary in the spectrometer from 0.9 to 6.2 m. In each measuring station (barrel or end-cap), tubes are assembled in two multi-layers, which are kept separated by a rigid support structures (spacer frames) that provides accurate positioning of the drift tubes with respect to each other and support to the components of the alignment system (see Fig.2.5).

Multi-layers are formed by 3 or 4 layers of tubes, four-layer chambers being used in the inner stations. The mechanical accuracy in the construction of these chambers is extremely tight to meet the momentum resolution requirements of the spectrometer. Using an X-Ray Tomography [30], which measure the wire position with an accuracy of less than 5 $\mu$m, the precision in wire position inside a chamber has been checked to be higher than 20 $\mu$m r.m.s. The required high $p_T$ resolution crucially depends also on the single tube resolution, defined by the operating point, the accurate knowledge of the calibration and the chambers' alignment.

The MDT chambers use a mixture of Ar-$CO_2$ (93%-7%), kept at 3 bar absolute pressure, and are operated with a gas gain of $2\times10^4$. These parameters were chosen in order to match the running condition of the experiment: the MDTs can sustain high rates without aging [31], and with little sensitivity to space charge. The single tube resolution is below 100 $\mu$m for most of the range in drift distance, and the resolution of a multi-layer is approximately equal to 50 $\mu$m.

In order to take advantage of such tracking accuracy covering a surface per chamber up to 10 $m^2$, an extremely accurate mechanical construction is needed. Furthermore, precise monitoring of the operating conditions is required for best performance. Among these issues, very important is an excellent alignment system that enables the monitoring of the position of the different chambers in the spectrometer with a precision higher than 30 $\mu$m. Regarding this system, the aluminum frame supporting the multi-layers is equipped with RASNIK [32] optical straightness monitors. These monitors are formed by three elements along a view line: a laser that illuminates a coded target mask at one end, a lens in the middle and a CCD (Charged Coupled Device)sensors at the other end. This system provides a very accurate measurement of the relative alignment of three objects (1 $\mu$m r.m.s.) and is used both for checking the chamber deformation (in-plane alignment), and the relative displacement of different chamber (projective alignment). The chambers are also equipped with temperature monitors (in order to correct for the thermal expansion of the tubes, and for the temperature of the gas), and with magnetic field sensors, in order to predict the E×B effect on the drift time.

#### Cathode Strip Chambers: CSC

The background rate in the $2 <| \eta |< 2.7$ region of the inner tracking wheel of the End-Cap is large enough to demand the use of a precision detector with high granularity. A multi-wire proportional chamber with cathode strip read-out is used (the Cathode Strip Chamber) [27]. The anode wire pitch is 2.54 mm, and the pitch of the read-out strip is 5.08 mm. Cathode planes are equipped with strips orthogonal to the wires and the precision coordinate is obtained measuring the charge induced on the strips making charge interpolation between neighboring strips. Typical resolution obtained with this readout scheme is about 50 $\mu$m. The smallness of the basic cell implies also small maximum drift time (about 30 ns) which is beneficial to keep the chamber occupancy low. The gas mixture is based on Ar (30%), $CO_2$ (50%) and $CF_4$ (20%) and the wires are supplied by 2.6 kV, resulting in a gas gain of $10^4$. In ATLAS the CSCs are arranged in two layers, each containing 4 layers of cells, enabling 8 high precision measured points on a single track.

### 2.3.3 Trigger chambers

The ATLAS physics program demands for a highly flexible trigger scheme with different programmable transverse momentum thresholds. At low luminosity a 6 GeV/c threshold for two or more muons is adequate for Beauty physics, while higher transverse momentum thresholds (20 GeV/c) will be used for Higgs search and high $p_T$ physics measurements. The muon trigger in ATLAS is organized in three level. The first level trigger (LVL1), implemented in hardware, uses reduced-granularity data, coming only from the trigger detectors. The second level (LVL2) trigger uses software algorithms exploiting the full granularity and precision data from most of the detectors, but examines only the region on the detector flagged at the LVL1 as containing interesting information (Region of Interest, RoI). The third level trigger (LVL3) or Event Filter (EF) reconstructs muons applying the same refined algorithms of the offline reconstruction in the RoI identified by LVL2. Typical rates at the three trigger levels are 75 kHz (LVL1), 1 kHz (LVL2) and 100Hz (LVL3).

The LVL1 trigger uses specialized trigger detectors: RPCs in the Barrel and TGCs in the End-Caps. They are both characterized by fast response, needed to handle background and to associate tracks to the LHC bunch

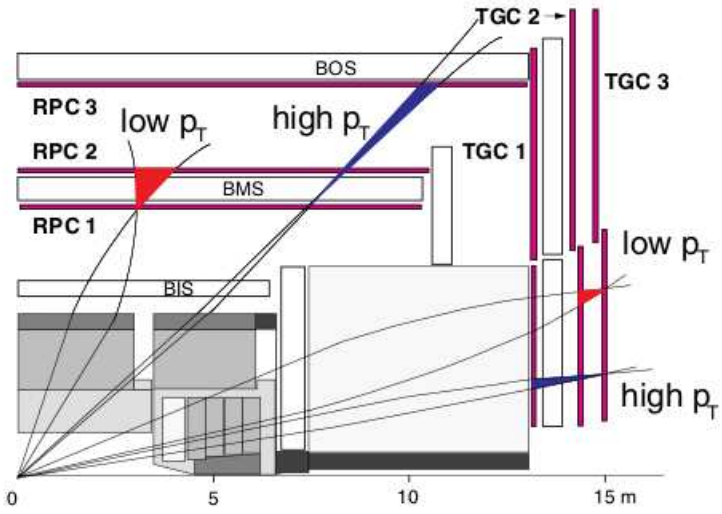


Figure 2.6: *Trigger scheme for high and low $p_T$ thresholds in the Barrel and in the End-Cap*

crossing. The trigger scheme used in both the Barrel and the End-Caps is illustrated in Fig.2.6.

Three layers of detectors are used. In the barrel the low $p_T$ trigger uses predefined coincidence patterns, in both projections, using the RPC middle station. The momentum resolution is about 20% and is limited mainly by multiple scattering and by fluctuation of the energy loss in the calorimeters. The high $p_T$ trigger requires a coincidence pattern using all three RPC stations. At $p_T$ of 20 GeV/c the momentum resolution is about 30 % and is limited by the axial length of the interaction region and by multiple scattering in the central calorimeters. The same logic is applied to the trigger scheme in the End-Caps. The $p_T$ threshold is defined by the width of the coincidence patterns and can be programmed. This width depends on the rapidity, and for a 20 GeV/c threshold it varies from about 40 cm in the Barrel to about 5 cm in the End-Caps.

### Thin Gap Chambers: TGC

The Thin Gap Chambers are multi-wire proportional chambers with a smaller distance between the cathode and the wire plane compared with the distance

between wires [33]. In fact, the distance between the cathode and the wires is 1.4 mm compared with the wires pitch that is 1.8 mm., while the wire diameter is 50 $\mu$m.

The gas mixture is 50% $CO_2$ and 45% n-pentane, which results in a highly quenching gas mixture that permits the operation in saturated avalanche mode (see next chapter for detailed description of the gas detectors operation modes). Due to this operation mode, these detectors are not very sensitive to small mechanical deformations, which is very important for large detector as ATLAS [34].The saturated mode has also two more advantage: the signal produced by a minimum ionizing particle has only a small dependence on the incident angle up to angles of 40 degrees; the tails of the pulse-height distribution contain only a small fraction of the pulse-heights (less than 2%). The chambers operate at high voltage of about 3 kV. The operating condition and the electric field configuration provide for a short drift time ($< 30$ ns), enabling a good time resolution. The readout of the signal is done both from the wires (which are grounded together in a variable number, according to the desired trigger granularity as a function of the pseudo-rapidity) and from the pick-up strips plane placed on the cathode. The wires and the strips are perpendicular to each other enabling the measurement of the orthogonal coordinates, however, only the wire signal are used in the trigger logic.

Test performed at high rate have shown single-plane time resolution of about 4 ns with 98% efficiency, providing a trigger efficiency of 99.6% [35].

### Resistive Plate Counters: RPC

The RPC are gaseous detectors providing a typical space-time resolution of 1 cm $\times$ 1 ns with digital readout. The active element of the RPC unit is a narrow gas gap formed by two parallel resistive Bakelite plates, separated by insulating spacers. The primary ionization electrons are multiplied in avalanches by a high, uniform electric field of typically 5 kV/mm. The gas mixture used has been selected in order to allow operating in saturated avalanche mode (see next chapter for the gas detector operation mode description) and is composed of three gases: 94.7% $C_2H_2F_4$, 5% $C_4H_{10}$, 0.3% $SF_6$. Tetrafluoroethane ($C_2H_2F_4$) has been chosen as main component since, in addition to satisfy safety requirements, exhibits moderately high primary ionization at low operating voltage. Moreover, the mixture contains isobutane ($C_4H_{10}$) as photons quencher and $SF_6$, in order to reduce the amount of delivered charge and inhibit the streamer development.

Amplification in avalanche mode produces pulses of typically 0.5 pC. Signals are readout via capacitive coupling by metal strips on both sides of the detectors. In ATLAS, RPC are mounted on MDTs with a mechanical structure that fix the relative position between RPCs and MDTs. In one readout plane strips ($\eta$ strips) are parallel to the MDT wires and provide the bending view, while in the other plane strips ($\phi$ strips) are orthogonal to the MTD wires, providing the second-coordinate measurement which is also required for the pattern recognition. RPC detectors will be extensively described in the next chapter.

# Chapter 3

# Resistive Plate Counters

## 3.1 Introduction

Resistive Plate Counters (RPC) have been developed in 1981 by R. Santonico and R. Cardarelli [36, 37]. They are gaseous resistive parallel plate detectors with a time resolution of $\sim$ 1 ns, consequently attractive for triggering and Time-Of-Flight applications.

Their main advantages, compared to other technologies, consist in their robustness, construction simplicity and relatively low cost of the industrial production. They are ideal to cover large areas up to few thousand square meters.

RPCs where originally used in streamer mode operation [38], providing large electrical signals, requiring low gain read-out electronics and not stringent gap uniformity. However, high rate applications and detector aging issues made the operation in avalanche [38] mode necessary. This was possible thanks to the use of new highly quenching $C_2H_2F_2$-based gas mixture instead of the traditional Ar-based mixture and to the development of high gain read-out electronics.

Streamers generation dynamics is difficult to study and the avalanche mode operation should open up the possibility of implementing detailed simulations, thus allowing for a better understanding of the physics processes in the RPC. In this chapter we will discuss RPC physics structure and operation.

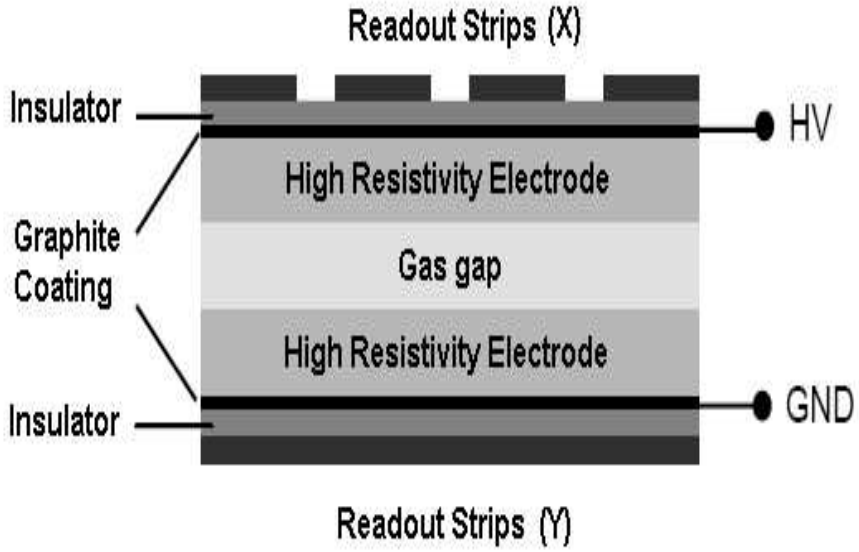


Figure 3.1: *Schematic image of the RPC.*

## 3.2 Resistive Plate Chambers

RPC, similarly to Spark Counters and Parallel Plate Avalanche Chamber [39, 36], consist of two parallel plate electrodes made of a material with high resistivity, typically glass or Bakelite. A charge $Q_0$ produced in the gas gap by an ionization event and reaching the electrode surface is locally removed from the electrode itself following an exponential law:

$$Q(t) = Q_0 e^{-t/\tau} \text{ with } \tau = \rho\varepsilon_0\varepsilon_r \tag{3.1}$$

where $\rho$ is the volume resistivity and $\varepsilon_r$ is the relative permittivity of the resistive material. $\tau$ is defined as the time needed for the electrode to get charged again and varies from $\tau \approx$ 1 s for glass resistive plates (for which the volume resistivity is $\rho \approx 10^{12}$ $\Omega$cm) to $\tau \approx$ 10ms for plastic-laminated plates for which $\rho \approx 10^{10}$ $\Omega$cm). We will refer from now on to Bakelite electrodes which are the ones used in the ATLAS RPC. Fig. 3.1 shows a schematic view of a typical RPC. Two parallel Bakelite electrode plates, having a volume resistivity $\rho \simeq 10^{10\pm1}\Omega\times$cm, delimits a 2 mm gas gap filled with a gas mixture at atmospheric pressure. These plates are coated, on

the external side, with a thin graphite layer with a surface resistivity ranging from 100 to 300 k$\Omega/\Box$. The graphite layer allows to uniformly apply the high voltage to the electrodes without screening the avalanche signal induced on metal strip readout panels. The readout panels are segmented into strips and simply pressed on the external electrode surface. The readout strips are on both sides of the gap and arranged in perpendicular directions in one side with respect to the other, allowing to measure the $x$- and $y$-coordinate of the ionizing particle. Strip panels are separated from the graphite coating by an isolating PET foil. Moreover, the assembled RPC gas volume is filled with linseed oil, which is then slowly taken out. The resulting effect is the deposition of a thin layer of polymerized oil [36] which smooth both inner Bakelite surfaces. This is done in order to strongly reduce the detector dark current and noise counting rate.

The fundamental processes underlying RPCs are well known: a charged particle produces free charge carriers in the gas, which drift towards the anode and are multiplied by an uniform electric field induced by an external high voltage applied to the electrode plates. The propagation of the growing number of charges induces an electric signal on the read-out strips, which is amplified and discriminated by the front-end electronics.

In the following sections, we will briefly describe the physics processes that produce a signal in the RPC detectors and, in general, in a gas detector, the transport properties of electrons in a gas when an electric field is applied, the electron avalanche generation and related phenomena. Finally, we will illustrate the mechanism of the signal induction by the avalanche.

## 3.3 Particle Energy Loss in the Matter

A charged particle crossing a material will loose energy by Coloumbian inelastic scattering with atomic electrons of the material. If the impact parameter is large compared to the size of the atom (a *distant collision*), the atom will react 'as a whole'to the variable electromagnetic field of the charged particle. The result can be excitation or ionization of the atom with the emission of an electron with small energy. Instead, if the impact parameter is of the order of the atomic dimension (a *close collision*), the interaction involves one of the atomic electrons. As a consequence, the electron is ejected from the atom with considerable energy (knock-on electrons or delta rays). If the collision energy is sufficiently large we can treat all close collision by

considering the atomic electrons as free particles.

The total energy lost by the charged particle is the sum of the two contributions: close and distant collisions. For distant collisions, it is important to take into account the binding energy of the electrons to the atoms, this mean to consider the average ionization energy $I$ [MeV] of the atom [40]. For close collision is necessary to consider the maximum transferable energy Emax, applying energy and momentum conservation principles. These leads to the following relation for the maximum kinetic energy transferable to a free electron by a particle of mass $m$ and velocity$\beta$ (in units of $c$)[41]:

$$E_{max} = \frac{2m_e c^2 \beta^2 \gamma^2}{1 + 2\frac{m_e}{m} sqrt1 + \beta^2\gamma^2 + (\frac{m_e}{m})^2} \tag{3.2}$$

which for relativistic particles becomes:

$$E_{max} \approx 2m_e c^2 \beta^2 \gamma^2 \tag{3.3}$$

The two contributions to the total energy loss by a heavy particles can be written as:

$$-\frac{1}{\rho}\frac{dE}{dx}\Big|_{coll} = \frac{k}{\beta^2}\frac{Zz^2}{A}\left[ln\frac{2m_e c^2\beta^2\gamma^2 E_{max}}{I^2} - 2\beta^2 - \delta\right] \tag{3.4}$$

where:

$\frac{1}{\rho}\frac{dE}{dx}\Big|_{coll}$ - the average energy loss [MeV cm$^2$/g],

$k$ - a constant defined by $k$=2$\pi$ N$_a$r$_e{}^2$m$_e$c$^2$ [= 0.1535 MeV cm$^2$/g],

$\rho$, $Z$, $A$ - the density, atomic number and atomic weight of the absorbing material,

$r_e$ - the classic electron radius $r_e$= 2.817$\times$ $10^{-13}$ cm,

$m_e$ - the electron mass,

$N_a$ - the Avogadro's number,

z, $\beta$ - the charge and the velocity of the particle in units of electron charge and $c$ respectively,

$\gamma$ - is given by $1/\sqrt{1-\beta^2}$ as usual.

The small correction $\delta$ is called density effect due to the material polarization, for which the electric field of the particle is partly screened. Therefore, even if in relativistic regime energy loss should increase as the electric field increases with the energy, due to $\delta$ the distant collision contribution to the energy is lower as expected.

Eq.3.4 is the *Bethe-Bloch* [42] equation for the energy loss due to ionization and excitation for charged particles heavier than electrons.

Considering electron/positron crossing the material the formula is different due to the fact that the incident electron/positron has a small mass and the assumption that the incident particle is not deflected during collision is not anymore valid. Moreover, in the electron-electron collision we have identical particles and their indistinguishability must to be taken into account. In this case $E_{max} = E_{kin}/2$, where $E_{kin}$ is the incident electron/positron kinetic energy and we obtain for the energy loss:

$$-\frac{1}{\rho}\frac{dE}{dx}\Big|_{coll} = \frac{k}{\beta^2}\frac{Zz^2}{A}\left[ln\frac{\pi^2\gamma^3(m_e c^2)^2}{I^2} - a\right] \tag{3.5}$$

where $a$= 2.9 for electrons and $a$=3.6 for positrons.

The quantity (- $\frac{dE}{dx}\Big|_{coll}$)$\delta x$ is the average energy loss due to ionization and excitation in a medium layer with thickness $\delta x$. The energy loss will fluctuate around this average value event by event according to the *Landau* distribution [43]. The distribution has a typical shape, with a maximum followed by a high energy tail due to the $\delta$-electron emission during the ionization. Only for thick layer, where energy loss exceeds one half of the original particle energy, the distribution becomes roughly Gaussian [41].

*Primary cluster* of free charge carriers (electron-ion pairs) are deposited along the trajectory of the particle. In the RPC gas volume they are collected and multiplied by a strong uniform electric field and the propagation of the growing number of charge induces a signal on the read-out electrodes. The primary ionization is characterized by the average number of clusters per unit length and by the cluster size distribution.

## 3.4 Fundamental Processes in Gas Detectors

The basic mechanisms underlying the gas detectors operation is the ionization generated by a charged particle crossing the gas and producing electron-ion

pairs (primary charge). In the following sections we consider the behavior of free electrons in a gas, with an electric field applied, and how they give rise to a detectable signal.

### 3.4.1 Electrons Diffusion

According to the equipartition law, the average thermal energy of a gas molecule with f degrees of freedom is $\epsilon_T \sim$(f/2)kT, where k is the Boltzmann constant ($\epsilon_T \approx 0.035$ eV for T = 273 $^o$K). The kinetic energy $\epsilon$ is also normally distributed according to:

$$F(\epsilon) = c\sqrt{\epsilon} exp - \frac{\epsilon}{kT} \tag{3.6}$$

with a mean velocity $u$ given by $u = \sqrt{3kT/m}$. Due to the thermal motion and to the molecular scattering, a localized charge distribution is diffused in the surrounding volume, whereby, there will be a dispersing Gaussian density distribution with increasing spread. The spread increases in time and is determined by the diffusion coefficient $D$ following the formula [44]:

$$\frac{dN}{N} = \frac{1}{\sqrt{4\pi Dt}} exp - (x^2/4Dt)dx \tag{3.7}$$

The standard deviation of the distribution along one coordinate is $\sigma_x = \sqrt{2Dt}$. The diffusion coefficient becomes larger with increasing thermal velocity $u$ of the molecule and decreases with the increasing mass of the particles. In addition, in absence of magnetic field, the diffusion coefficient decreases for increasing value of the mean free path $\lambda$ between collision. $\lambda$ is related to the collision cross-section $\sigma(\epsilon)$, which in general depends on the kinetic energy of the particles:

$$\lambda(\epsilon) = \frac{1}{n\sigma(\epsilon)} \tag{3.8}$$

where $n = \mathrm{N}_a \rho / \mathrm{A}$ is the number of molecules per volume, A is the molar mass, $\rho$ is the density of the gas and $\mathrm{N}_a$ is Avogadro's number.

The mean free path of electrons, $\lambda_e$, is considerably larger than the one for ions and the relation between the two is given by $\lambda_e = 5.66\ \lambda_{ion}$ which is approximately fulfilled for most gases. During the primary electron multiplication, i.e. the avalanche development in the gas described in

sec.3.4.4, the charge distribution diffuse laterally and longitudinally due to the electrons diffusion. In RPC counters the avalanche spread, before charge collection occurs, is of about few millimeters.

### 3.4.2 Electron Drift

Let's consider a swarm of electrons with thermal velocity $u = \sqrt{2\epsilon/m}$, localized at a point P at time $t$=0. The electrons move away from P in all directions isotropically for diffusion. In addition, an homogeneous electric field with strength $\mathbf{E} = (0, 0, \mathrm{E})$ in the $z$-direction is applied. Than, electrons will be accelerated by $\mathbf{a} = \mathrm{q}\mathbf{E}/\mathrm{m}$ along z, acquiring in average a drift velocity given by:

$$v_D \sim a\tau = a\frac{\lambda_e}{u} = \frac{qE}{m}\frac{\lambda_e}{u} \tag{3.9}$$

where $\tau$ is the mean time between collisions. Electrons can gain much more energy in an electric field between two collisions in a gas because their mean free path is longer than that for ions.

If the collision cross-section $\sigma$, and therefore the mean free path $\lambda_e$, are independent of the thermal velocity $u$, we get a proportional increase of the drift velocity with the field. For electrons this is true only at very low electric fields. In particular, the wavelength of electrons, for kinetic energies of about 1 eV, corresponds to the size electron orbits in an atom and due to quantum-mechanical effects the atoms became nearly transparent to electrons. This leads to a minimum in the electron-atom collision cross-section $\sigma$ as a function of $\epsilon$ ('Ramsauer effect') and to a steep increase of the drift velocity with the electric field. In real situations very complex behaviors are observed. Let try to give a simple description to this phenomena [45].

Under the influence of the electric field, electrons adjust their velocity to a constant drift. The energy gained in the electric field has to be compensated by the energy lost in collision with atoms. If we call $\Delta(\epsilon)$ the fraction of the electron energy $\epsilon$ lost in one collision, then:

$$qE(v_D\tau) = \Delta(\epsilon)\epsilon \tag{3.10}$$

where $v_D\tau$ is the average movement of the electrons swarm during $\tau$. Expressing $\tau$ in term of $\frac{\lambda_e}{u}$ and $\epsilon = \frac{u^2 m}{2}$ we get:

$$qEv_D \sim \frac{1}{2}\frac{\Delta(\epsilon)mu^3}{\lambda_e} \tag{3.11}$$

and, finally, using eq. 3.9, we have:

$$v_D \sim \sqrt{\sqrt{\frac{\Delta}{2}}\frac{qE}{m}\lambda_e(\epsilon)} \tag{3.12}$$

As approximations to the energy dependence we use simple power laws of the form $\Delta(\epsilon)\sim\epsilon^m$ and $\lambda_e(\epsilon)\sim\epsilon^{-n}$. The dependence of $v_D$ on the field strength $E$ comes out substituting the previous power laws in Eq.3.9 and Eq.3.12

$$v_D \sim E^{(m+1)/(m+2n+1)} \tag{3.13}$$

For low field strength, i.e. below the Ramsauer minimum, one obtains n $\approx$ -1, and with m $>$ 1 a rapid increase of $v_D$ with $E$ is obtained. At electron energies above the Ramsauer minimum, n $\approx$ +1, and the increase of $v_D$ with $E$ is expected to be much slower. Qualitatively, such behavior is observed in argon and other noble gases.

In molecular gas (e.g. $CO_2$, $CH_4$, Iso-$C_4H_{10}$) the inelastic collisions contribute significantly to the total cross-section, because of molecular energy oscillations and vibrations in the range from 0.1 to 1 eV. The fractional energy $\Delta(\epsilon)$ transferred from the electron to the molecule becomes very large in such inelastic collisions, but decreases again above the maximum excitation energy $\epsilon_{max}$, approximately as

$$\Delta(\epsilon) \sim \frac{\epsilon_{max}}{\epsilon} \tag{3.14}$$

For $\epsilon > \epsilon_{max}$, the exponent m $\sim$ -1, and eq. 3.13 gives a drift velocity independent of the electric field strength. If $\Delta(\epsilon)$ decreases with $\epsilon$ at an even greater rate, then m $<$ -1, and $v_D$ decrease with increasing $E$.

For which concerns diffusion, it's worth to notice that for some gases (e.g. argon), when an electric field is applied, the electron diffusion coefficient becomes not isotropic and the diffusion parallel to **E** is not equal to the one defined in Sec. 3.4.1.

### 3.4.3 Electron Recombination and Capture

The generated free ions and electrons can be neutralized in the gas before they are detected.

Recombination process of positive ions with negative ions or with electrons can occur. The density decrease of positive ions, $n^+$, with time can be described by the relation -d$n^+$/d$t$=$\alpha n^+ n^-$, where $n^-$ is the density of the negatively charged particles and $\alpha$ is called 'recombination coefficient'. In gases, like $O_2$ and $CO_2$, $\alpha$ can reach a value of $10^{-6}$ cm$^3$/s for recombination with negative ions, and values up to $10^{-7}$ cm$^3$/s for recombination with electrons.

Free electrons are removed from the gas also by the molecular capture. Gas molecules with several atoms are able to capture electrons of low (eV) energy and produce negative ions of lower mobility. The probability $p_a$ that this happens during one collision is negligibly small for noble gases and for $N_2$, $H_2$ and $CH_4$, but not for electronegative gases like $O_2$, $Cl^-{}_2$, $NH_3$ and $H_2O$. The mean time for electron capture is given by $t_a = 1/(p_a n_s)$ where $n_s$ the number of collisions per unit time. For strongly electronegative gases at normal conditions $t_a$ can be as small as 5 ns.

If an electric field is applied, the kinetic energy $\epsilon$ of the electrons increases and the probability $p_a(\epsilon)$ for electron capture varies with energy. In this case the mean free path of electrons relative to electron capture is

$$\lambda_a = \frac{v_D}{p_a n_s} \tag{3.15}$$

Considering this capture effect, it comes out that the free electrons intensity in the gas ($I_{e0}$) is reduced with the drift distance following an exponential law:

$$I_e = I_{e0} exp(-\beta x) \tag{3.16}$$

where $\beta$ is named "attachment coefficient ", which depends strongly on the energy of the ionizing particle and on the presence of an electric field. A similar strong dependence, but of opposite sign, is related to the electron avalanche development which is the topic of the next section.

### 3.4.4 Electron Multiplication

The amount of charge collected by the electrodes depends on the electric field intensity in the gas detector. From Fig. 3.2 we can see that if the electric field is too low (A-B region in Fig. 3.2) the charges created by ionization recombine and no signal is detected. Increasing the electric field

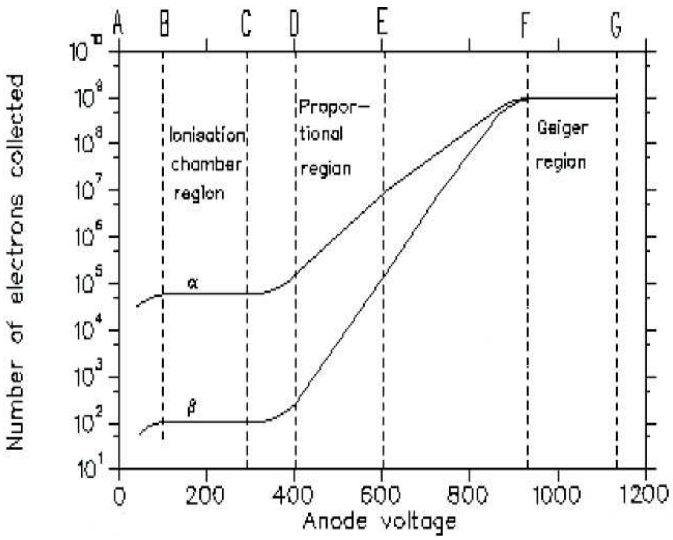


Figure 3.2: *Gas electron amplification as a function of the applied electric field.*

(B-C region in Fig. 3.2), the primary charges is collected to the electrode, but no secondary ionization takes places. This is the operation region of the ionization chambers.

At higher electric field (D-E region in Fig. 3.2) we have the operation region of proportional and drift chambers. In this detectors, primary electrons are under the influence of an electric field of a strength ($10^4$-$10^5$ V/cm) large enough that they can gain a kinetic energy larger than the energy ionization of the other atoms or molecules in the gas and then induce *secondary ionization* processes. A chain of such reactions leads to an avalanche of electrons and ions ('Townsend avalanche'). The free charge formed in the primary ionization $n_e$ is amplified by a factor $A$, which represents the gas gain or *gas amplification factor*. In this regime the amplification factor $A$ is independent of the amount of primary ionization and the measured pulse is proportional to the primary charge (*proportional region*, A ranging from $10^4$ to $10^6$).

The number of electron-ion pairs formed by an electron along a path of 1 cm length is called the *first Townsend coefficient* $\alpha = 1/\lambda = n\sigma_{ion}$, where $\sigma_{ion}$ is the ionization cross-section for collisions and $n$ the atomic density of the gas. If the number of primary electrons is $n_0$, the number $n(x)$ of electrons

after a path length $x$ is obtained as:

$$n(x) = n_0 exp(\alpha x) \tag{3.17}$$

to be compared with Eq. 3.16.

Photons originated by the atomic de-excitation, during the multiplication process, give rise to secondary phenomena. They produce, in fact, photo-electrons in the gas or extracted from the electrodes. This phenomenon is quantified by the *second Townsend coefficient* $\gamma$, i.e. the probability to have a generated photo-electron for each electron belonging to the avalanche. If an avalanche started by $n_0$ primary electrons, $n_0 A$ electrons are produced in secondary ionization and, at the same time, $(n_0 A)\gamma$ photo-electron are produced in connection with ultraviolet photons from radiative processes. These photoelectrons are then amplified producing $n_0 A^2 \gamma$ secondary electrons. In this avalanche $n_0 A^2 \gamma^2$ photoelectrons are formed again, and $n_0 A^3 \gamma^2$ electrons are liberated, etc. Adding the number of electrons from the sequential steps, one obtains:

$$n_0 A_\gamma = n_0 \sum_{n \geqslant 0} (A\gamma)^n = \frac{n_0 A}{1 - A\gamma} \tag{3.18}$$

This $A_\gamma$ is the gas amplification factor including the energy transfer by photons. If $A\gamma \rightarrow 1$ and quenching mechanism are nor present, than the gas gain became infinite. This region of operation is called *Geiger-Muller region* (F-G region in Fig. 3.2). In the Geiger-Muller region the avalanche spreads over the whole counter and leads to a complete discharge. The gas amplification in this case is $A \sim 10^8$-$10^{10}$ and the signal output no longer depends on the primary ionization.

In a detector not operating in Geiger-Muller mode, the propagation of the ultraviolet photons is prevented, in order to avoid the discharge, by adding quenching gas which absorbs energetic photons. Usually this is an organic gas like isobutane ($C_4H_{10}$) that is efficient in absorbing photons in the relevant energy ranges.

In the region between the proportional and the Geiger-Muller regime there is still a *limited proportionality* (E-F region in Fig. 3.2) between primary ionization and total liberated charge. This region is given approximately by $\alpha x \sim 20$ or $A \sim 10^8$. RPC detectors in avalanche mode, as the ones in ATLAS and CMS muon spectrometers, operate in this region ("saturated avalanche"regime) that is characterized by space charge phenomena and gas

gain increasing only linearly with the external field. The space charge effects are mainly due to local electric field deformation caused by avalanche charge carriers. In fact, at the tip and tail of the charge distribution the electric fields become higher than the applied one. Instead, in the avalanche center the field is lower. This electric field distortion modifies the avalanche growth and secondary and non-linear effects can take place.

## 3.5 Signal Readout in RPC

We will start considering a single electron of charge -$e$ moving inside the gas volume under the influence of a constant electric field and we will evaluate the electric signal induced on an external conductive plane.

### 3.5.1 Ramo's theorem: the 'k factor'

A charge $q$(t) moving with velocity $v_D$(t) induces an instantaneous current $i(t)$ according to the formula (Ramo's theorem [46]):

$$i(t) = q(t)v_D(t)\frac{E_w}{V_w}, \tag{3.19}$$

where $E_w$ is the so called $weightingfield$, which is obtained by applying $V_w$=1 V at the pick-up strip and grounding all the other electrodes. It is important to notice that the weighting field is a fictitious field, different from the real electric field, which determines the drift velocity $v_D$(t) of the electron. It turns out that in the RPC detector the readout plane weighting field is given by the equation:

$$\frac{gE_w}{V_w} = k = \frac{\epsilon_r g}{\epsilon_r g + 2d} \tag{3.20}$$

where $d$ is the electrode plate thickness, g the gas gap thickness and $\epsilon_r$ is the electrode relative dielectric permittivity. Equation 3.20 shows that, due to the presence of the high resistivity electrodes, the induced signal is reduced by the factor k (ranging from 0.5 to 0.7 for $\epsilon_r$ ranging from 5 to 10).

In the RPC detector the electron drift velocity is uniform and the induced current is constant until the electron is collected by the electrode. In the real device the readout plane consists of metal strip of 3 cm pitch as in figure 3.3. Just underneath the strip the electric field is quite uniform and the

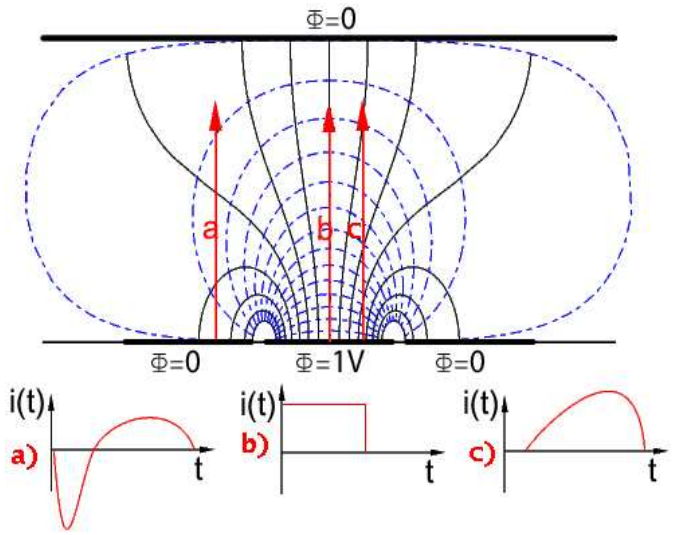


Figure 3.3: *A schematic view of the weighting field in a RPC detector (and, generically in strip detector) and the induced signal.*

previous formula is approximately valid (plot b). Instead, moving aside from the middle strip point, the weighting field is not uniform anymore (plot c) and the induced signal is distorted. When the charge is collected by the nearby strip (plot a) the weighting field changes sign and the induced signal is bipolar.

The induced signal is also partially modified by the presence of the thin graphite layer, which is not full electrostatically transparent. The graphite layer, located between the resistive electrodes and the metal strips, tends to differentiate the signal with a time constant $\tau_{grap}$ given by [47]:

$$\tau_{grap} = R\epsilon_0(g+d) \approx 100k\Omega \cdot 8.8 \cdot 10^{-12}\frac{F}{m}4 \cdot 10^{-3}m = 3.52ns \qquad (3.21)$$

where $\epsilon_0$ is the vacuum permittivity, $g$ and $d$ are the thickness of the gas gap and of the electrodes respectively, and R the graphite surface resistivity. If T is the charge collection time a strong distortion of the signal shape happen for $\tau_{grap} << 0.1$ T until to became a bipolar signal (see [47]). In Bakelite RPC where T is of the order of few ns the effect of the graphite layer is small on the induced signal.

The avalanche electrons collected by the anode resistive plate must be quickly removed in order to restore the initial local electric field. The electrode recovery time $\tau_r$ is related to its volume resistivity $\rho_b$:

$$\tau_r = \rho_b \epsilon_0 (\epsilon_b + \frac{d}{g}) \approx 12 \rho_b \epsilon_0 \tag{3.22}$$

where $\epsilon_b \approx 5$ is the Bakelite relative permittivity. Assuming a volume resistivity of about $10^{10} \Omega cm$ we obtain a RPC recovery time of about 1 ms, which correspond to a rate capability of $f_r = \frac{1}{\tau_r} = 1$ kHz.

### 3.5.2 Signal Induced by an Electron Avalanche

In presence of an avalanche multiplication process the induced signal increases directly like the avalanche charge, according to the formula:

$$i(t) = v_D E_w q(t) \tag{3.23}$$

where $v_D$ is the electron drift velocity in the gas and q(t) the evolution of the avalanche charge. In proportional regime we have an exponential growth of the signal which terminate when the electrons are absorbed by the anode:

$$i(t) = -e v_D E_w e^{\eta v_D t} \tag{3.24}$$

where $\eta = \alpha - \beta$ is the effective Townsend coefficient and is given by the difference between the first Townsend coefficient ($\alpha$) and the attachment coefficient ($\beta$). If the avalanche saturates (see Fig. 3.4), because space charge effects occur, its growth is not exponential anymore (e.g. linear as in ref aielli) and it may even stop growing (e.g. in ref riglher). In any case using Eq. 3.23 and knowing the electron drift velocity $v_D$ we can estimate the total charge of the avalanche from the maximum of the induced current.

Instead, the relation between the total induced charge and the total avalanche charge is more difficult to extract. In fact, integrating eq 3.23 we get the total induced charge. In proportional regime the relation between total charge $Q_{coll}$ developed by the avalanche and collected by the anode with the induced charge is simple:

$$Q_{ind} = \frac{k}{\eta g} Q_{coll}, \tag{3.25}$$

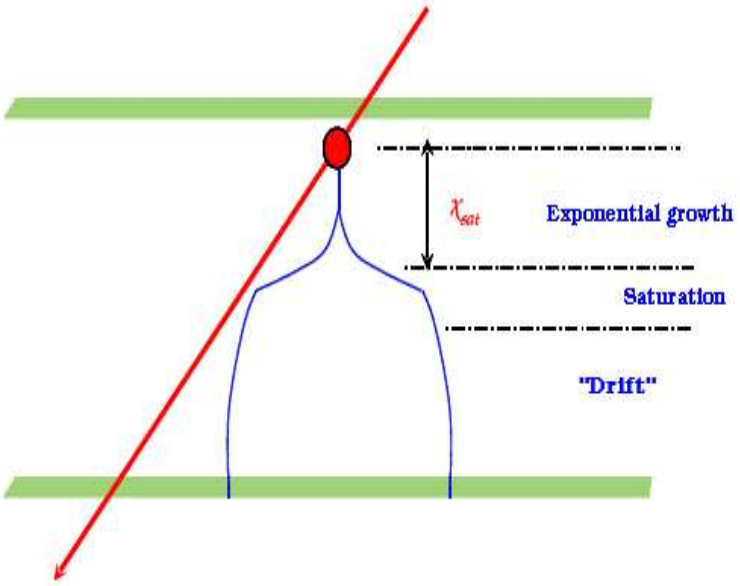


Figure 3.4: *Electron avalanche evolution in a strong uniform electric field.*

but in a saturated avalanche regime, the direct proportionality is lost. In particular, due to the slower charge multiplication the induced charge is less suppressed with respect to the collected charge [48].

### 3.5.3 Single Electron Avalanche Fluctuation

The simple picture described in previous paragraph is complicated by the statistical fluctuations of the avalanche growth. The final distribution which describes also these fluctuations is a controversial issue. In literature different empirical models have been considered and the most popular ones are: the exponential and the Polya distribution.

Assuming that the ionization probability is independent of the history of previous collisions we obtain an exponential distribution. This assumption is valid for low values of the electric field $E$ (Furry's law) [49]. The probability dp to find n+1 electrons in x+dx is proportional to the number n of electrons in x: $dp = \eta n dx$. Integrating over a path of length $l = g - x_0$ the probability

that n electron are produced after the path l is given by the :

$$p_{exp}(n) = \frac{1}{< n >} e^{-\frac{n}{<n>}} \tag{3.26}$$

where $< n >= e^{\eta(g-x_0)}$ is the mean of the exponential distribution.

For high values of $E$ the assumption is not valid anymore and the probability dp to find n+1 electrons in x+dx is not proportional to the number n of electrons in x: $dp = \eta n(\frac{1}{1+\theta} + \frac{\theta}{(1+\theta)n})dx$. Integrating along the path we obtain the Polya distribution:

$$p_{Polya}(n) = [\frac{n}{< n >}(1+\theta)]^{\theta} e^{-\frac{n}{<n>}(1+\theta)} \tag{3.27}$$

which depends on the phenomenological parameter $\theta$ and presents a peak in the shape. Unfortunately, the parameters $\theta$ characterizing the Polya distribution are not directly related to a physical picture. The Polya distribution is reduced to the exponential distribution by requiring $\theta \to 0$.

In reference [1] a parameter $r$ is introduced in order to separate the low and the high electric field cases. This parameter is defined as:

$$r = \frac{E}{\alpha U_{ion}(eV)} \tag{3.28}$$

where $U_{ion}$ is the ionization potential of the gas expressed in eV. For r >> 10 avalanche fluctuation is expected to follow the exponential distribution. In typical Bakelite RPC we have E = 50 kV/cm, $\alpha \approx 100$ cm$^{-1}$ and $U_{ion} \approx 12.5$ eV which correspond to r$\approx$ 40 and the charge spectra is expected follow an exponential decreasing curve and don't present a maximum. Whenever higher electric field are applied strong charge space effect can completely saturate the avalanche development and a more Gaussian like shape of the distribution should be expected.

# Chapter 4

# Experimental Set-up and Measurement Technique

## 4.1 Introduction

The main goal of this thesis was to characterize, by measuring transport and amplification parameter in a prototype RPC filled with the ATLAS RPC gas mixture (94.7% of tetrafluorethane $C_2H_2F_4$, 5 % isobutane $C_4H_{10}$ and 3 % sulphur hexafluoride $SF_6$). We performed this study by using a technique in which a strongly focused UV laser beam induce ionization in a very small spatial region inside the RPC gas gap. Exploiting the same technique, similar studies have been already performed but without introduction of $SF_6$ [50] in the mixture. Adding even very small percentage of this gas modifies significantly the gas mixture properties and in particular inhibits the streamers rising in a large working point interval of the RPC detector [51].

The already existing facility for the study of the electron transport parameters in gas detectors, present in Lecce INFN laboratory [52], was used. Most of its instrumentation has been upgraded and a new acquisition and data control system has been developed.

## 4.2 Gas Ionization by UV Laser

The laser light is a very useful calibration and diagnostic instrument for gas detectors, due to the capability to simulate charged particle tracks in the gas

[53]. For this to occur, there must be molecules in the gas with appropriate ionization potential and the laser energy and energy density must be enough to ionize them. Ultra Violet (UV) laser sources are employed, while laser sources with higher wavelength (in the visible or infrared spectrum) are excluded because the ionization probability decreases rapidly with the increasing wavelength. The advantages of using this ionization technique are:

- the possibility to ionize in a very small region inside the gas gap and, therefore, to know with high precision (depending only on the laser focus and intensity) the ionization point;
- the ionization probability follows the Poisson distribution;
- the possibility to originate ionization clusters from one up to hundreds of electrons, depending on the laser intensity.

The laser ionization mechanism can happen also through multi-photons ionization of the gas molecules. The detecting gases usually used as active medium have an ionization energy higher than the photon energy of the laser commonly used. For example the ionization energy is 15.7 eV in Ar, 14.4 eV in $CO_2$, 13.1 eV in $CH_4$, 12.64 eV in $C_2H_2F_4$ [54] and 10.57 eV in $C_4H_{10}$, while the the photon energy of a Nitrogen laser (which was used for this thesis) is 3.68 eV. Actually, the ionization occurs via two or $n$-photons absorption process by small quantities of low ionization potential impurities always present in the gas volume.

For this to occur, the $n$ photons need to be incident on the molecule during the lifetime of molecular intermediate states. Due to the fact that the photons act incoherently on the gas, the ionization rate varies as the $n$th power of the photon flux. In fact, the probability of $n$ photons to arrive in a given time interval is equal to the $n$th power of the probability of each one of them, and it is therefore proportional to the $n$th power of the photon flux $\phi$. In particular, in a gas volume $V$ containing gas molecules with density $N$, the ionization rate $R$ is given by:

$$R = \phi^n N V \sigma^{(n)} \tag{4.1}$$

where $\sigma^{(n)}$ is the $n$th order cross section for $n$-photon collisions.

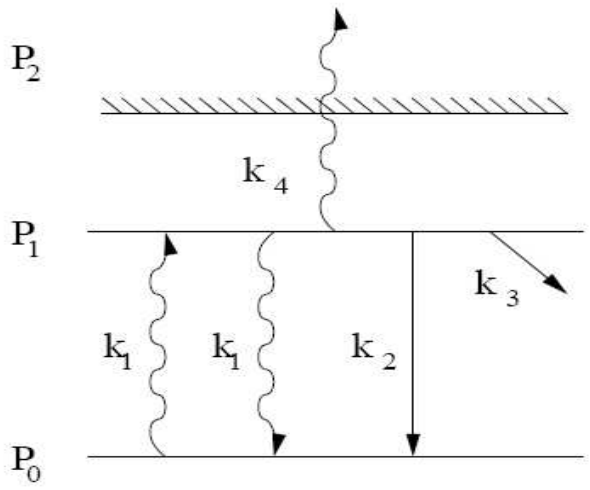


Figure 4.1: *Transitions involved in the two photons ionization process.*

For a light pulse containing $m$ photons, with area $A$ and duration $T$, the flux $\phi$ and the energy $E$ are given by:

$$\phi = m/(AT) \tag{4.2}$$

$$E = mh\nu = mhc/\lambda \tag{4.3}$$

In a gas volume V=AL, the specific ionization per unit track length for the $n$-photon process is:

$$\frac{RT}{L} = \frac{m^n}{(AT)^{n-1}} N\sigma^{(n)} = \Big(\frac{E}{AT}\Big)^n ATN\Big(\frac{\lambda}{hc}\Big)^n \sigma^{(n)} \tag{4.4}$$

where (E/AT) is the power density of the laser beam.

Let's see now in more details what happens in the gas when two-photon ionization occurs. Let's suppose to distinguish three electronic energy levels in the gas molecules: the ground level $E_0$, the intermediate level $E_1$, and the continuum ionization level $E_2$; being $P_0$, $P_1$, and $P_2$ the population density of the three levels in the gas. The incident radiation induces transitions $0\rightarrow1$, $1\rightarrow2$, and $1\rightarrow0$. This last transition can be also a spontaneous transition (see Fig. 4.1). There may be also losses from level 1 into other channels.

The transition rates per molecule are denoted by $k_1$ (0→1,1→0 stimulated), $k_2$ (1→0 spontaneously), $k_3$ (1→ other channels), and $k_4$ (1→2 ionization). They are determined by the incident flux and by the internal transition mechanism.

The differential equations that rule the level populations can be written as follow (the primes denote time derivatives):

$$\begin{aligned} P_0^{'}(t) &= -k_1 P_0(t) + (k_1 + k_2) P_1(t) && (4.5) \\ P_1^{'}(t) &= +k_1 P_0(t) - (k_1 + k_2 + k_3 + k_4) P_1(t) && (4.6) \\ P_2^{'}(t) &= +k_4 P_1(t) && (4.7) \end{aligned}$$

The rate per molecule $k_1$ is taken to be proportional to the incoming flux $\phi$ of photons through the cross-section $\sigma_{01}$ for the process 0→1:

$$k_1 = \sigma_{01}\phi \tag{4.8}$$

The transition rate $P_2^{'}(t)$ give the rate of ionization. From Eq. 4.7, it results to be proportional to the density $P_1(t)$ of the intermediate state and to the corresponding rate per molecules, $k_4$ given by:

$$k_4 = \sigma_{12}\phi \tag{4.9}$$

The first two equation, 4.5and 4.6, are a system of homogeneous linear differential equation. In order to solve the system we have to do a variable transformation that separates the equations. The eigenvalues $s_1$ and $s_2$ of the coefficient matrix are given by zeroing the determinant:

$$\begin{vmatrix} -k_1 - s & k_1 + k_2 \\ k_1 & -(\sum k) - s \end{vmatrix} = 0 \tag{4.10}$$

where $\sum k = k_1 + k_2 + k_3 + k_4$. Solving the equation we get:

$$s_{1,2} = -\frac{\sum k + k_1}{2} \pm \left[ \left( \frac{\sum k + k_1}{2} \right)^2 - k_1(k_3 + k_4) \right]^{1/2} \tag{4.11}$$

These two eigenvalues are real and negative and we assume $s_2 < s_1 < 0$. At this point we can find the solutions of the differential equations 4.7 applying

the initial condition $P_1(0) = 0$ and $P_2(0) = 0$:

$$P_0(t) = \frac{P_0(0)}{s_1 - s_2}[-(k_1 + s_2)e^{s_1 t} + (k_1 + s_1)e^{s_2 t}] \quad (4.12)$$

$$P_1(t) = \frac{P_0(0)k_1}{s_1 - s_2}[e^{s_1 t} - e^{s_2 t}] \quad (4.13)$$

$$P_2(t) = \frac{P_0(0)k_1 k_4}{s_1 s_2}\Big[1 + \frac{s_2}{s_1 - s_2}e^{s_1 t} - \frac{s_1}{s_1 - s_2}e^{s_2 t}\Big] \quad (4.14)$$

The last equation 4.14 presents the general solution to the problem. It describes the concentration of ionization electrons as a function of the time and of the molecular rate transition coefficients $k_1$, $k_2$, $k_3$ and $k_4$. For small time $t$, we can develop the exponentials up to the second order in $s_1 t$ and $s_2 t$ and we get:

$$P_2(t) \to \frac{1}{2}k_1 k_4 P_0(0)t^2 \quad (4.15)$$

For a laser pulse of duration T and using Eq. 4.8, 4.9, last equation becomes:

$$P_2(t) \to \frac{1}{2}\sigma_{01}\sigma_{12}P_0(0)\phi^2 T^2 \quad (4.16)$$

from which the quadratic dependence of the electron ionization concentration due to the photon flux $\phi$ and the pulse duration $T$ is derived. From Eq. 4.15 we get a second order effective cross-section. In fact, for a laser shot of duration $T$ and considering $R/V = P_2/T$ we have:

$$\sigma^{(2)} = \frac{1}{2}\sigma_{01}\sigma_{12}T \quad (4.17)$$

(which has the dimension of $L^4T^{-1}$).

## 4.3 Experimental Set-up

The experimental set-up used to perform all measurements and realized in the Lecce INFN laboratory is shown in Fig. 4.2. In this set-up two lasers ($N_2$ and one He-Ne), a photo-tube, the metal box containing the RPC prototype and all the optical device fundamental to align and focus the laser beam on RPC were housed (lens, beam splitter, optical filters, mirrors). All set-up components will be described in details in this section.

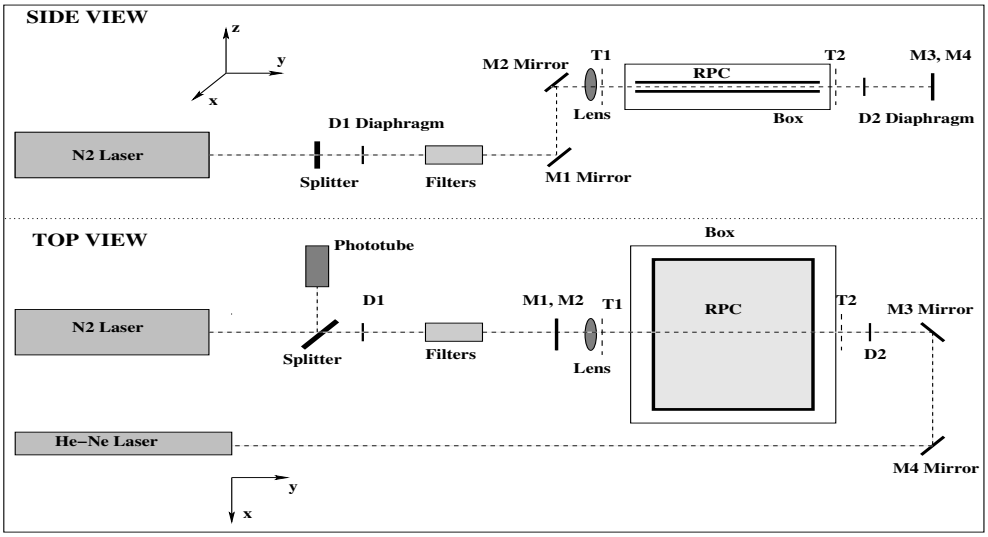


Figure 4.2: *Experimental Set-up scheme: side view and top view*

### 4.3.1 RPC Prototypes

For the work described in this thesis two RPC prototypes have been used. Each prototype, with dimensions 10 × 20 cm$^2$, has a 2 mm gas gap delimited by two 2-mm-thick linseed-oil-treated Bakelite plates. The main difference between the two prototypes consists in the Bakelite resistivity of the electrodes. In the first prototype (see Fig. 4.3), that we'll call RPC I, the resistivity was about 1.4 $\times 10^{11}$ $\Omega cm$ at 20 $^o$C, while for the second prototype, RPC II, the Bakelite resistivity was about 1.71 $\times 10^{10}$ $\Omega cm$ at 20 $^o$C about one order of magnitude lower and very close to the ATLAS RPC Bakelite resistivity.

In RPC II two circular spacers (of 1 cm diameter) were introduced in the gas gap in order to ensure an higher uniformity in the gap height. Two apertures (2×50 mm$^2$ for RPC I and 2× 30 mm$^2$ for RPC II) were placed in the center of the longer edge of the RPC's to allow for the passage of the laser beam. The external electrode surfaces were covered with a thin layer of graphite for high voltage distribution. The signal was read out by 1 cm pitch strip connected to a pre-amplifier Phillips Scientific 6954 (1.8 GHz bandwidth, 220 ps rise time ) with an amplification factor of 100. The readout planes were separated from the Bakelite electrodes by isolating PET

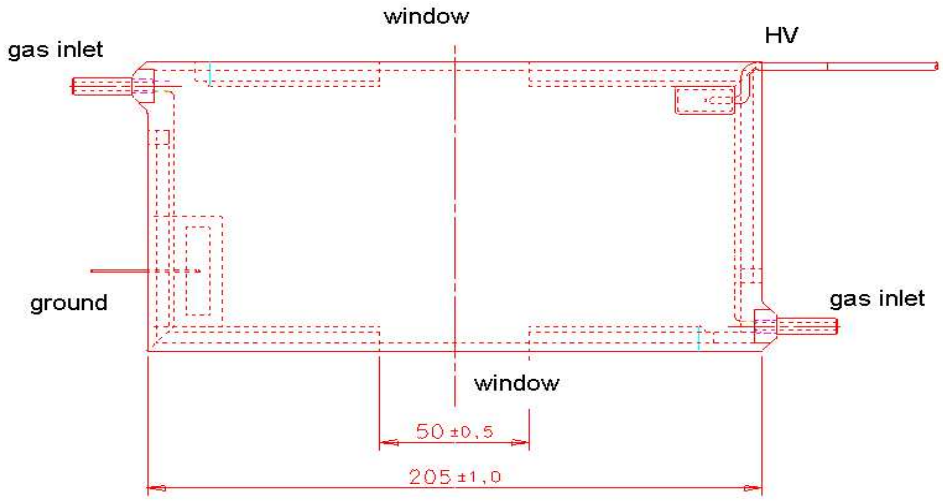


Figure 4.3: *Schematic view of the RPC I detector.*

foils.

The detector was hosted in a metal box ($40 \times 20 \times 10$ cm$^3$) with two UV-silica windows transparent to the laser beam (see Fig. 4.4). It was aligned in the horizontal plane by mean of three supports that allow for micro-metric adjustment.

On the box cover were placed the connectors for HV supply and for signal readout, together with two gas inlets and two gas outlets. Through the gas inlets the gas mixture was directly flushed inside the RPC and filled the entire box volume with a rate of 50 sccm (standard cubic centimeter per minute), corresponding to about one volume exchange every 1.5 hours. The RPC signal after pre-amplification was sent to a digital oscilloscope (HP 54522 A) of 2 Gsa/s sampling rate and 500 MHz bandwidth.

### 4.3.2 Optical System and Laser Alignment

Along the Nitrogen laser optical path, several components were placed to align the beam on the RPC. The first component was a quartz beam splitter (Laseroptik) whose attenuation factor was depending on the angle with respect to the incoming beam. The splitter was positioned at $45^o$ respect to the beam and reflected a fraction of the laser beam towards a fast photo-

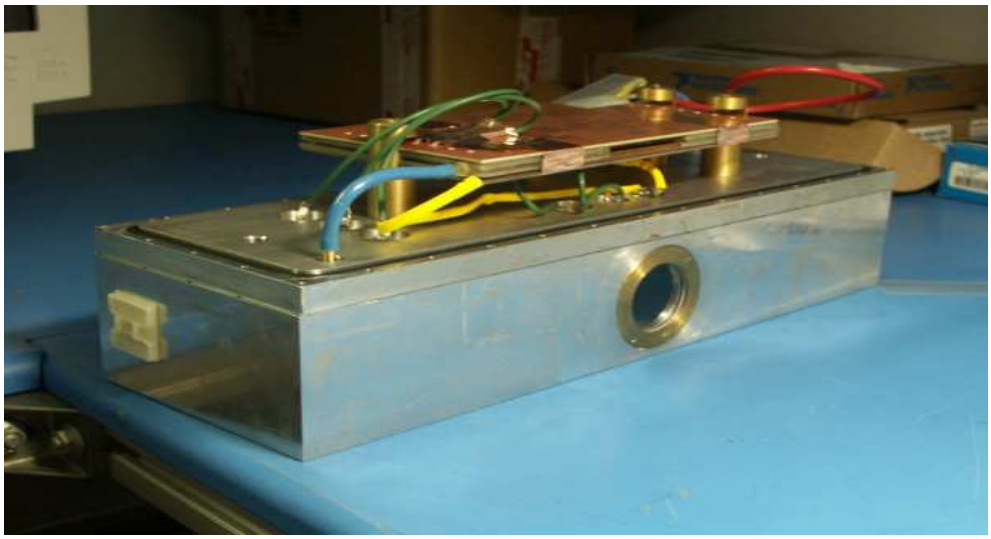

Figure 4.4: *The RPC prototype mounted on the metallic box cover, before insertion in the box.*

tube (Hamamatsu, Mod. R1328U-52, 60 ps rise time) that provided the trigger signal. The transmitted beam fraction went through a diaphragm $D_1$ and a series of optical attenuators that provided a controlled reduction of the beam intensity. After this a periscope, that consisted of two mirrors $M_1$ and $M_2$ (Fig. 4.2), was placed at $45^o$ respect to the incoming beam. It was possible to adjust the $M_1$-$M_2$ relative orientation through micro-metric screws. The $M_2$ mirror was mounted rigid with a 10 cm focal lens on a mobile arm, that allowed to move the lens focus along the $z$ axis.

Behind the metal box were placed two mirrors ($M_3$ and $M_4$ in Fig. 4.2) and a diaphragm ($D_2$ in Fig. 4.2) that, together with the He-Ne laser, were used to perform and monitor the optical alignment.

### Alignment Procedure

The relative alignment UV laser-RPC detector is a crucial point for all the measurements described in the following. the first step of the alignment procedure consists in the horizontal positioning of the RPC electrodes. This has been done just once, when the detector has been housed inside the box. The electrodes have been positioned horizontally by using a system of three

props that allowed micro-metric movements of the RPC in the box.

Then the alignment of the laser beam, by using optical components, has been done every day before starting any set of measurements.

The laser beam alignment procedure consists on two phases:

- Alignment of the He-Ne laser[1] on RPC.

  Two diaphragms with a 1 mm hole in the center are located respectively (see Fig. 4.2) in front of the lens ($T_1$) and behind the box quartz window ($T_2$). A third diaphragm $D_2$, $T_1$, $T_2$ and the gas gap center have been previously aligned at the same height. The He-Ne laser, by mean of the $M_3$ and $M_4$ mirrors, is reflected on the $T_2$ diaphragm. Through micro-metric movements of the mirrors it is possible to align the He-Ne laser with $T_1$, $T_2$ and $D_2$, placed between the box and the $M_3$ mirror. Then, acting on the micro-metric screws that regulate the position of the periscope mirrors ($M_1$ and $M_2$) it was possible to align the $D_1$ diaphragm (whose center is mechanically positioned at the same height of the UV laser shutter) and with the UV laser;

- Alignment of the UV laser on RPC.

  The UV laser was turned on and acting only on the laser positioning it was possible to align this laser with the He-Ne laser. After this step the He-Ne laser was turned off.

### 4.3.3 Gas System

The gas system is shown in Fig. 4.5. It allowed to mix the different gas components and continuously control the total flux and the single gas component percentages.

As specified in the previous sections the mostly analyzed gas mixture was the ATLAS RPC gas mixture: 94.7% of tetrafluorethane ($C_2H_2F_4$), 5 % isobutane ($C_4H_{10}$) and 3 % sulphur hexafluoride ($SF_6$). The three gases purity guaranteed from the provider was $\sim$ 99.97%.

The single gas components arrive from independent lines to different mass flow meters, each one characterized by a maximum flux value calibrated in Nitrogen gas. The maximum flux value for a gas different from Nitrogen is

[1]For the alignment has been used a He-Ne laser because this is a continuous and visible laser unlike the UV laser that is pulsed and not visible.

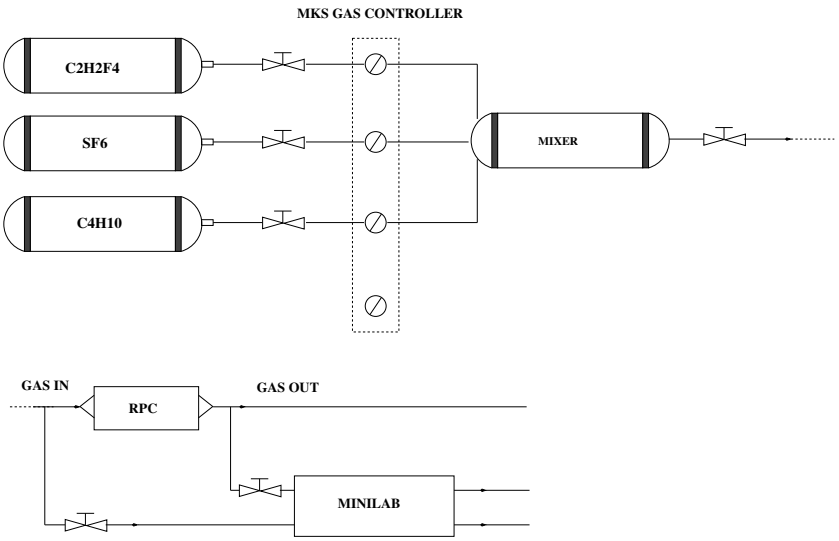


Figure 4.5: *Gas system scheme.*

settable using the corresponding correction factor supplied by the provider. For the tetrafluoroethane, isobutane and $SF_6$, the mass flow meters used were MKS Mod 1259, MKS Mod 1179 and MKS Mod 330 respectively. The accuracy of the mass flow meters is 1% FS (Full Scale) being 180 sccm, 13 sccm and 1.3 sccm the full scales for the three gases respectively. The mixture was flushed in the box containing the RPC with a total flux of 50 sccm.

Mass flow-meters were controlled by a digital controller (MKS Multi Gas Controller 647C ) that allowed, through GPIB protocol, to set the percentages and the fluxes of the different gases in the mixture and to monitor constantly the actual values.

Gases are mixed from the mass flow-meters into a mixer, from which the final mixture flows inside the metal box and the RPC in a continuously way (a volume change every 1.5 hours).

A mass spectrometer (MINILAB, shown in Fig.4.5) has been inserted in the gas system. to allow an on-line analysis of the gas mixture coming in and out of the RPC during its operation. This analysis can be used to track concentration of gas components over a wide dynamic range (parts per billion, ppb, to percent level). The inlet design ensures a rapid response to change in gas composition. An essential feature is that it should not contaminate or alter the gas sample in any way. For this reason, the MINILAB inlet

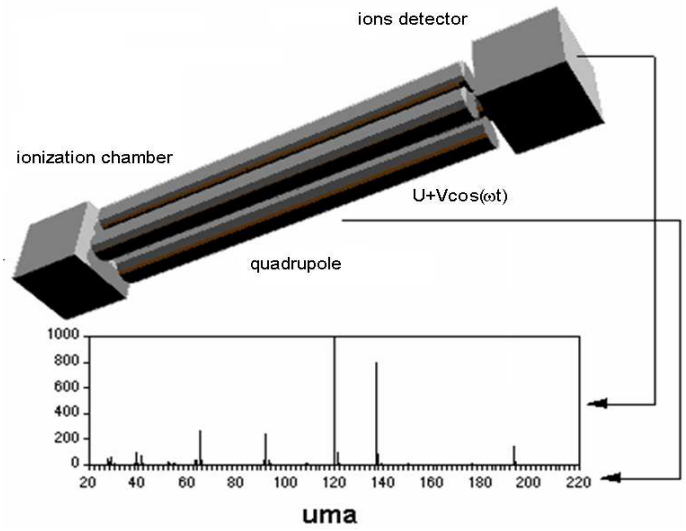


Figure 4.6: *Schematic view of the MINILAB quadruple.*

assembly incorporates an inert glass lined capillary, which can be heated to a constant temperature.

The main components of a mass spectrometer are an ionization chamber, an ions analyzer and an ion detector. Inside the instrument, the gas molecules are ionized by an electron beam. The fragmentation products are separated depending on the mass/charge ratio by an analyzer. For the MINILAB it is used a *quadrupole* as shown in Fig. 4.6.

Knowing the fragmentation spectra of a gas it is possible to trace all the components in the gas mixture. This was very useful in our case since we could check the gas mixture components coming in and out of the RPC during operation thus verifying the purity of the mixture and preventing contaminations. Fig. 4.7 shows, for example, the fragmentation spectra for the three gas components as given by *NIST* (National Institute of Standards and Technology) Standard Chemistry Webbook Database [55], that were taken as reference spectra.

The knowledge of the environmental parameters like atmospheric pressure, temperature and gas humidity, were crucial for the measurements here described. They were referred to standard condition of pressure and temperature (1013 mbar and $20^o$), then we decided to correct every minute the voltage applied to the RPC electrode in order to take into account

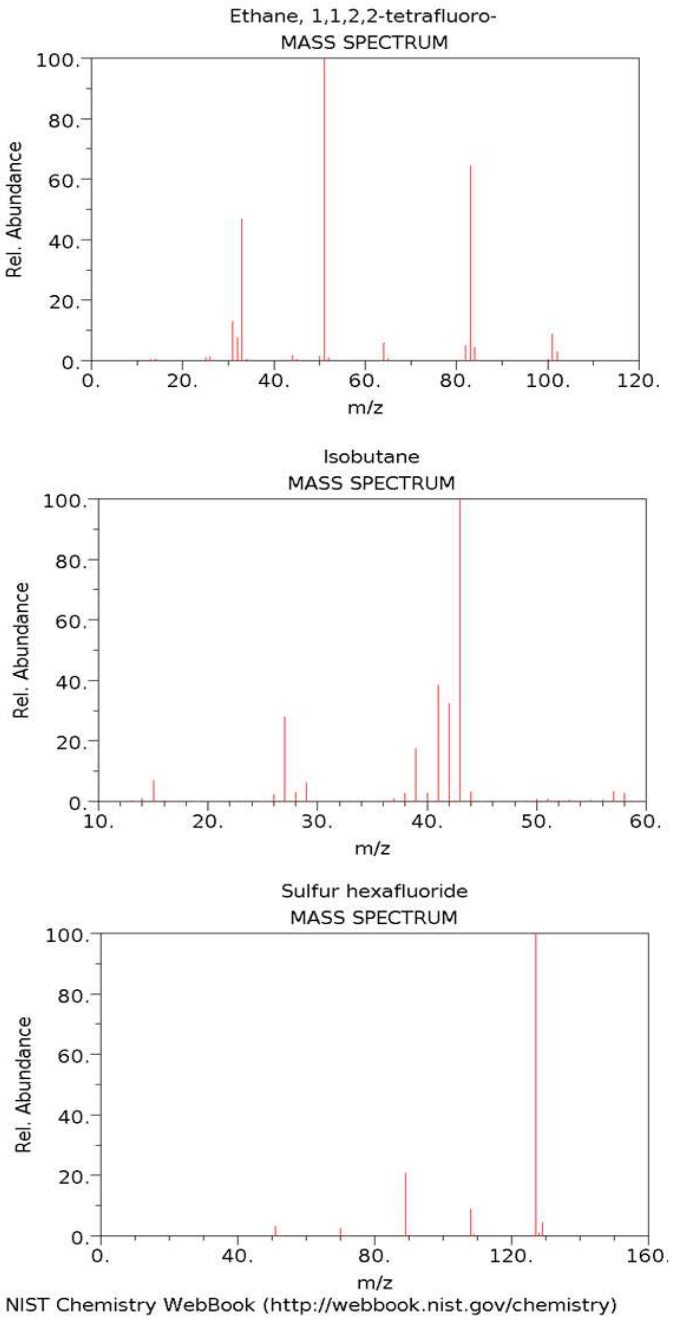


Figure 4.7: *NIST reference fragmentation spectra for the three gas mixture components.*

any change of pressure and temperature. The voltage $V_{corr}$ really applied was obtained by the voltage value set ($V_{set}$) by the HV system and by the measured values of pressure and temperature ($P_{meas}$,$T_{meas}$) as follows:

$$V_{corr} = V_{set} P_{corr} T_{corr} \quad (4.18)$$

$$P_{corr} = \frac{P_{meas}}{1013} \quad (4.19)$$

$$T_{corr} = \frac{293.15}{T_{meas} + 273.15} \quad (4.20)$$

Temperature and humidity were measured by two commercial probes. The probe measuring the temperature (Mod. IH-3602C) consists in a RTD sensitive to the temperature variations. Applying a constant current value and reading back the voltage, a temperature value can be obtained by a calibration formula given by the provider. The temperature is readout inside the experimental area. The humidity probe (HONEYWELL, MOd. HIH-4000-001) was inserted directly inside the metallic box and can therefore measure the gas mixture moisture. Also in this case we got back a voltage value from the probe which was converted in relative humidity by a calibration formula. The atmospheric pressure was measured by mean of a transducer (MKS Baratron) with an accuracy of $\Delta P/P \sim 10^{-4}$ mbar.

The two probes and the barometer were powered and read back by a VXI (Tektronix VX1410 Intelliframe), composed by a crate and several modules intercommunicating using a VXI protocol: a multichannel DAC module (Digital to Analog Converter), Mod. AO-48XDC, supplied the voltage and the current necessary to power the probes and the Baratron, an ADC module (Analog to Digital Converter), Mod. MIO-64XE-10, performed the measurements, finally a module VXI-MXI allowed the connection of the bus (that housed all the module) to the computer. The connection to the computer was realized through a serial interface MXI terminated with a PCI board compatible with the computer.

### 4.3.4 High Voltage System

High voltage (HV) for the photo-tube and the RPC operations was supplied through the system SY127 provided by CAEN [56]. The system is composed by one standard crate that houses a Control Unit and several HV plug-in channel modules. It can be locally monitored and controlled via on-board

alpha-numeric keypad and display. Remote control is also possible via RS-232-C port and it was the one used, by developing a dedicated software written in C++ language. Over-current and over-voltage protections where implemented in the software development phase together with channel trip detection and switch-off control.

Two HV modules have been used: a 4 channels module Mod. A333, providing 4/3 kV voltage with positive polarity used to power the photo-tube and a 2 channels Mod. A329, providing 15 kV voltage with positive polarity, used to apply HV to the RPC.

### 4.3.5 Micro-metric Movements System

Movements along the direction parallel to the laser beam ($y$ in Fig. 4.2) and perpendicular to the beam ($x$) were performed through a very high precision motorized bench VISIONCONTROL Mod. MC 841/1, Service Motor-control. It is composed of a marble bench on which two arms are positioned; the one perpendicular to the beam direction is fixed to the bench and supports the second arm (in direction parallel to the beam). These two arms were equipped with step motors and linear digital measuring rod. The linear precision of the axis, as provided by supplier, was $\delta S = (3 + 2 \times L/1000)$ $\mu$m, where $L$ is the distance in mm of the positioning point from the starting point.

The focal lens was mounted on a micro-metric motor that allowed to move along the $z$ direction the focus inside the gas gap with a precision of $2\mu$m/100mm. This motor is a Physic Instrument Mod. 415DG and allows movements up to 150 mm. It was remotely controlled by a Motor Control board Mod. C842.40 DC that can interface up to four different micro-metric motors.

From the provider specification, the high voltage module riproducibility is 1% of the set value at half full scale and 0.4% in all other ranges.

### 4.3.6 Nitrogen Laser

Ionization inside the RPC gas gap was induced by mean of the Nitrogen laser Mod. MNL 200 LD from Lasertechnik (Berlin) that produces UV radiation with $\lambda = 337$ nm. The main parameters characterizing the laser are reported in table 4.1. The laser is controlled via RS232 port. The software that allows

| | | |
|---|---|---|
| Peak Power | (kW) | 200 |
| Pulse Energy | ($\mu$ J) | >100 |
| Pulse Duration | (ps) | <700 |
| Wavelength | (nm) | 337.1 |
| Pulse Stability | % | $\pm$ 3 |
| Max Repetition Rate | (Hz) | 20 |
| Beam Divergence | (mrad) | 1.2 $\times$ 1.7 |
| Beam Dimension at the outlet | ($mm^2$) | 2 |

Table 4.1: $N_2$ laser main parameters as provided by constructors

to control the laser is called WINLAC and is supplied by the constructor. Fig. 4.8 show the user interface of WINLAC.

Laser was operated in continuous flow mode, therefore it was important to monitor the Nitrogen pressure, needed to be always around 2300 mbar in order to not compromise the laser operation stability. During the laser operation we constantly monitored the Nitrogen pressure and temperature in order to avoid damages to the instrument. Each time these two parameters exceeded maximum set values a pop-up window appeared with a "warning"message.

From the user interface it was also possible to set the repetition rate of the laser pulse by selecting the "repetition"mode on the control panel. The repetition rate could vary from 1 Hz to 20 Hz. It was also possible to operate in external trigger mode.

Before starting the measurements with RPC, a complete characterization of the laser was performed by measuring the laser pulse energy as a function of the Nitrogen pressure and repetition rate, the pulse duration and the beam dimension at the focal point of the lens.

The pulse energy was measured by mean of a JOULEMETER (Mod. J3S-09, MOLECTRON), which generates a signal that can be sent to an oscilloscope and whose pulse amplitude is proportional to the pulse energy. The proportionality factor was supplied by a calibration performed by MOLECTRON.

Fig. 4.9 shows the laser beam energy as a function of the repetition rate. Measurements were performed positioning the joule-meter just in front of the laser beam outlet and no substantial differences were observed in the beam energy varying the repetition rate. The maximum energy value per pulse was found to be $E_{max} \sim 122$ $\mu$J. Similarly we found that varying the Nitrogen

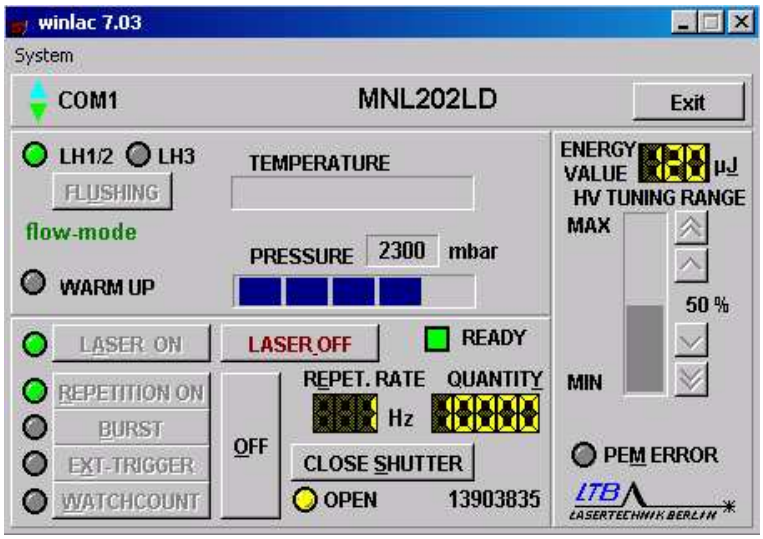


Figure 4.8: *User interface for the laser control.*

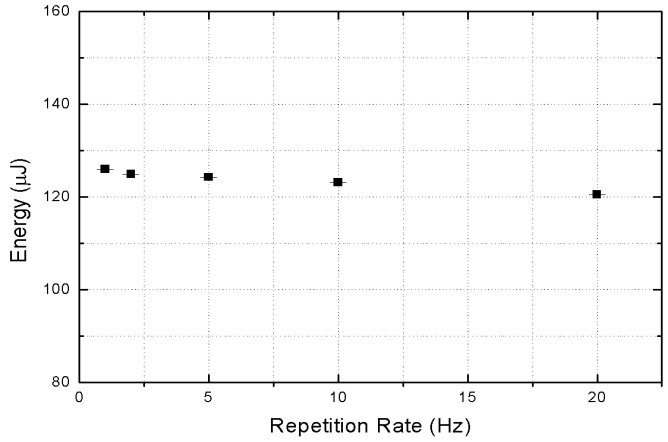


Figure 4.9: *UV laser pulse energy vs repetition rate.*

pressure of few hundred millibar around 2300 mbar the energy was stable.

FWHM (Full Width Half Maximum) of the pulse duration measurements, performed with the fast photo-tube used to provide the trigger signal, gave a value of $\leq$ 600 ps, similar to the one supplied by the laser constructors. This parameter is crucial since the pulse duration affects the drift velocity measurements due to the fact that introduces an indetermination on the ionization starting time. In fact, the ionization can occur at any time during the pulse duration and this uncertainty contributes to the drift time distribution width from which we get the electron arrival time. The smaller is the pulse duration, the higher will be the precision of the drift velocity measurements.

The drift velocity and gas amplification measurements were performed with an average of an electron ionization per laser pulse. In order to reach this condition, the beam intensity has been attenuated by mean of optical filters. As specified in Sec. 4.2, the gas ionization probability depends quadratically on the laser pulse intensity and the average number of ionizations scales quadratically with the optical filter transmittance coefficient T (see laser characterization measurements in Sec. 5.3).

### Laser Beam Width in the Focus

In order to fully exploit the possibility offered by the laser to ionize in "almost "puntiform region, it is fundamental to reduce as much as possible and to know with high accuracy the dimension of the beam in the lens focus.

The transverse dimension of the beam in several points along the $y$ axis (see Fig. 4.2) and around the focal lens distance (10 cmm from the lens) has been evaluated. To perform this measurements, we measured the laser beam energy by mean of the joule-meter by using a cup that allowed to shade half of the joule-meter sensible part. Positioning the joule-meter at a fixed position in the $y$ axis, we scanned the beam energy profile moving the lens (therefore the beam) along $z$. In more details the applied method was:

- in a fixed position along $y$, we measured the beam profile. This has been done by moving the beam along $z$ (few micrometer step) and therefore increasing the beam fraction reaching the Joule-meter. In Fig.4.10 we show, on the right, the signal amplitude as a function of $z$ in three different position along $y$;

- from the beam profile we calculated the spatial derivative of the

experimental points. The derivative has been fitted with a Gaussian whose $\sigma$ can be considered as half of the beam dimension (see Fig.4.10);

- we put in a graph the laser spot values as a function of the distance from the lens (Fig.4.11). The minimum ($\sim 8$ $\mu$m) has been assumed to be half of the beam dimension in the focal lens, which represent half of the error in the ionization position in our drift velocity measurements.

### 4.3.7 Signal Acquisition

By mean of the UV laser, controlled ionization was induced inside the gas gap at different positions (along the $z$ axis) from the RPC anode. As specified in the previous chapter, ionization electrons drifted and got multiplied towards the anode inducing on the readout strips a voltage signal. In our case the ionization was induced in a position that is around the center of the RPC electrode plate ($10 \times 20$ cm$^2$) and the signal was readout by the central strip perpendicular to the beam direction (the long edge of the electrode plates). This signal was sent to a digital scope HP54522A with 2 Gsa/s sampling rate and 500 MHz bandwidth set to provide time measurements with the best achievable resolution on single-shot signal (0.5 ns). Together with the signal from the RPC (already pre-amplified), the signal coming from the photo-tube was recorded. From the analysis of these waveforms:

- the electron *drift time* was obtained as the difference between the *start* time (trigger), given by the photo-tube, and the *stop* time given by the RPC. The start time was obtained by the photo-tube signal in correspondence of a trigger level set at 300 mV. The stop time was obtained by the determination of the peak of the signal coming from the RPC;

- the RPC signal amplitude was measured from which we studied the gas amplification and the charge spectra.

The two digitized signals were sent from the scope to a computer through a GPIB port and were saved in a file to be analyzed offline.

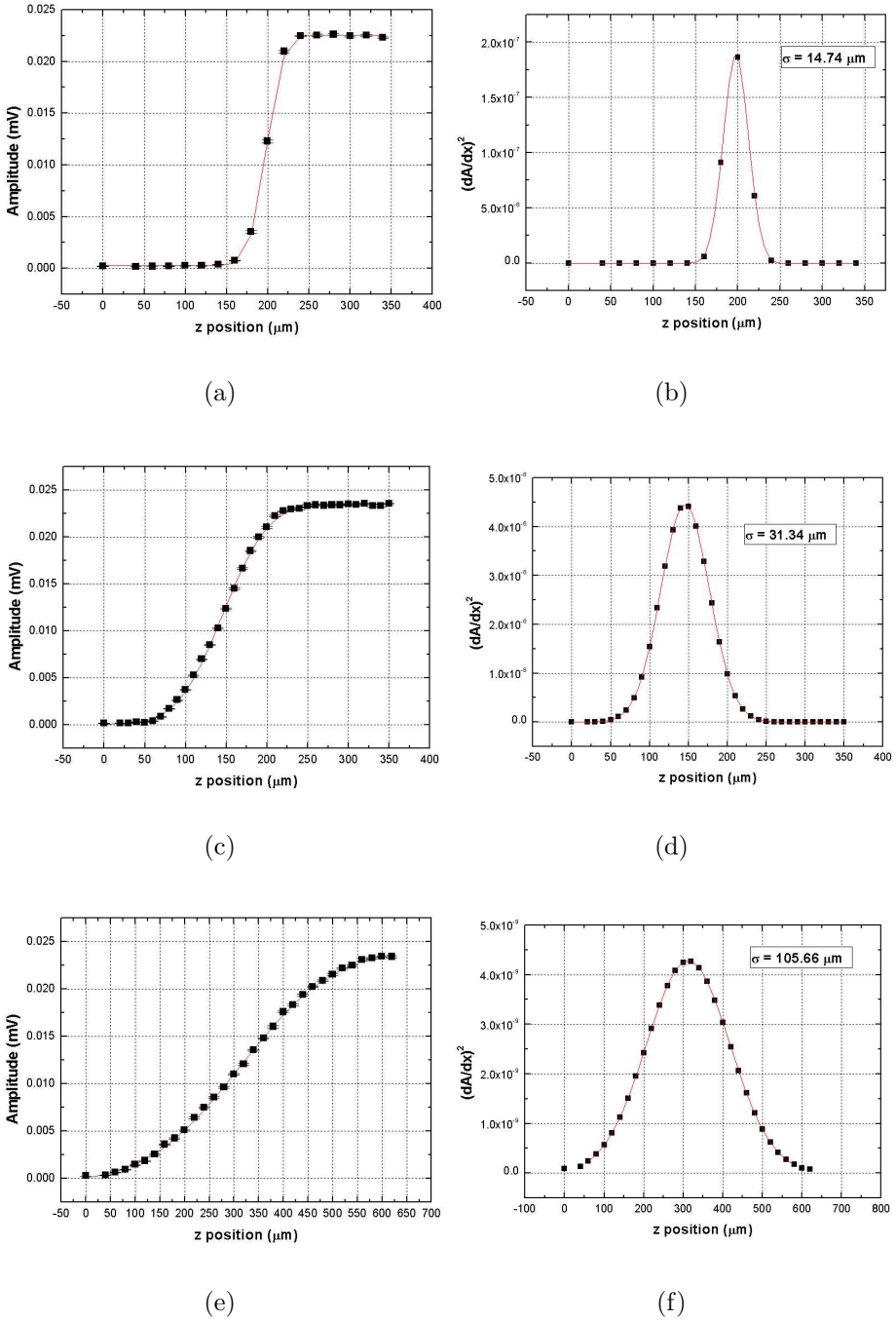


Figure 4.10: *Beam profiles and corresponding spatial derivatives in three different positions from the lens.*

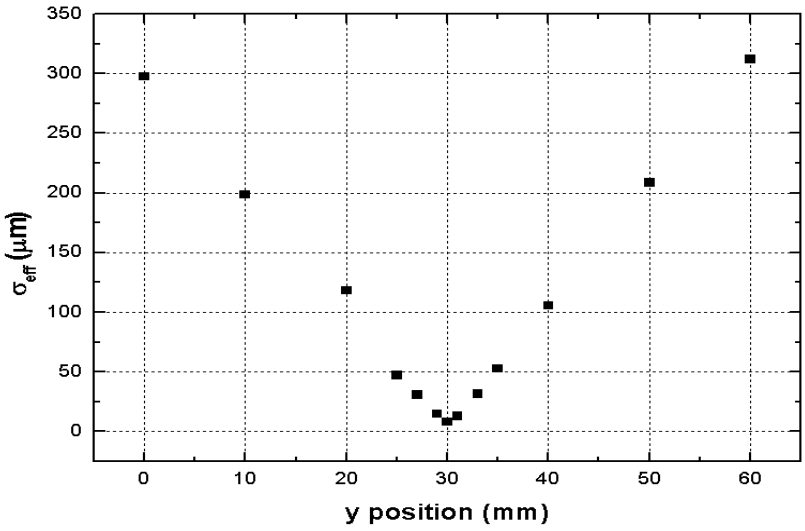


Figure 4.11: $\sigma_{eff}$ *of the laser beam at different positions along y axis. Measurements started at* $\sim$ *7 cm from the lens (point zeroin the graph)*

## 4.4 Acquisition and Control System

In Fig. 4.12 a scheme of the Data AcQuisition System (DAQ) and Data Control System (DCS) is shown. DAQ and DCS have been designed in order to ensure the maximum flexibility with respect to changes in hardware arrangements and measurement strategies. For this reason, their functionalities were separated into distinct software parts: one running on a windows-PC, which was directly interfaced to the hardware components (*DCS-DAQ loop*), and the second one running on a Linux-PC, which implemented the Graphical User Interface (*GUI*) and could be executed remotely from any PC. The communication between the GUI and the DCS-DAQ loop were realized by command strings using an on-line MySQL database as a buffer.

The main components of the acquisition and control system, i.e. the GUI, the MySQL database and the DCS-DAQ loop, are described in more details in the following.

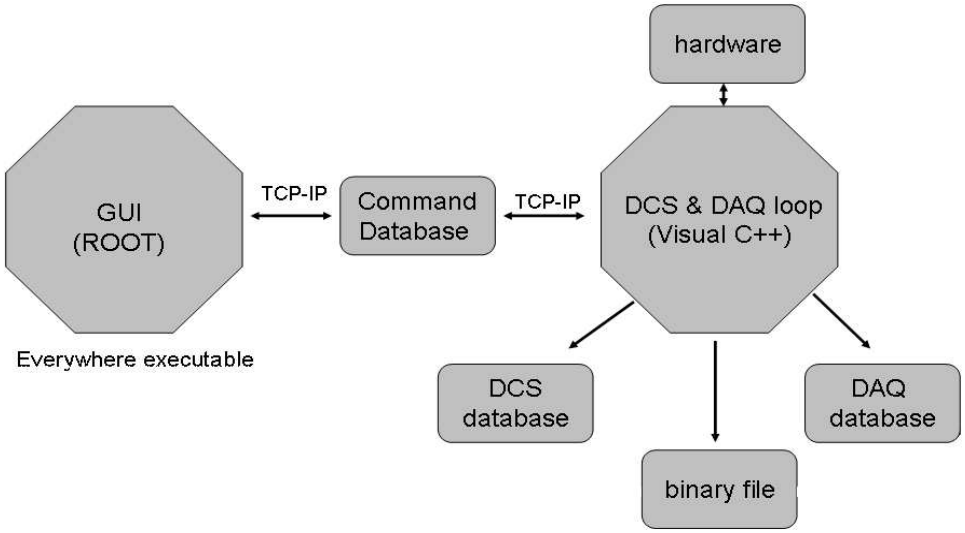


Figure 4.12: *DAQ and DCS system scheme.*

### 4.4.1 The Graphical User Interface GUI

The graphical user interface was an easy and useful instrument that allowed in principle to anybody to run a set of measurements. It was like a control panel provided of buttons and switches through which it was possible to execute a series of operations. By using these buttons and switches, the user could sent a series of command to a database, that was continuously read out by the DAQ-DCS loop that executed the command communicating directly with the instrumentation.

The GUI was realized by using the CERN software package known as ROOT [57]. ROOT is a framework implemented in *C++*, an "Object-Oriented"language, which offers a common set of features and tools for different application domains like: data acquisition, data analysis, event reconstruction, detector simulation and event generators.

Fig. 4.13 show the GUI how it appears to the users. It was decided to organize it in different "TAB", each one dedicated to a particular task:

- the **RUN** tab was used to execute a run. The user needed to insert the string "comment"to the run and the number of required events in the specific text boxes and then push the button "Run". In the same tab the button "Sleep"and "Stop"allowed, respectively, to sent

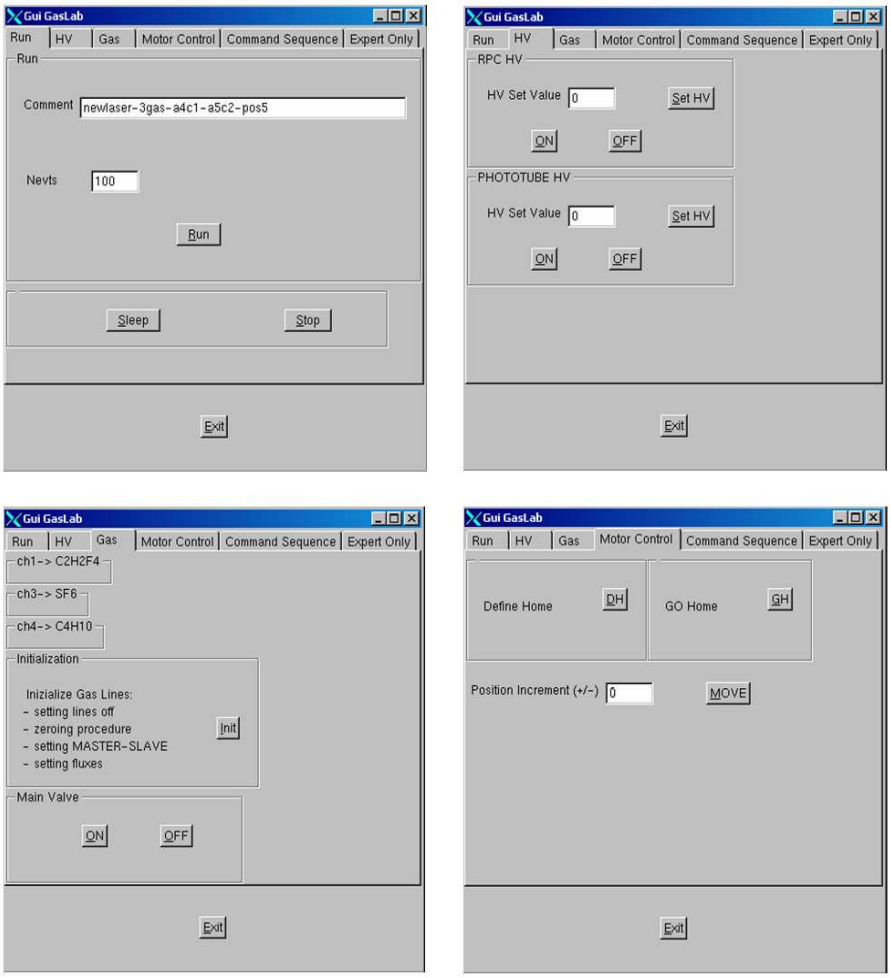


Figure 4.13: *Some tabs of the GUI interface.*

the DQA-DCS loop in line waiting for new command or to stop the run;

- the **HV** tab controlled the HV channels for the photo-tube and the RPC. For each HV channel there was a text box where it was possible to write the required HV value. Other three buttons were also present, one in order to set the chosen HV value and the others two to turn on and off the HV;

- the **Gas** tab interacted directly with the Multi Gas controller (see Sec. 4.3.3). The "Init"button started the instrument initialization procedure that was consisting in a series of step:

  1. switch off all the gas lines;
  2. execute a zeroing procedure for each line;
  3. set the "MASTER"(i.e the gas to which all the other gases are referred for the mixture percentages setting) and consequently the "SLAVE"gas (in our case a total flux of 50 sccm was set with the tetrafluoroethane as master gas);
  4. set the desired fluxes for each gas components.

  The "ON"and "OFF"buttons, finally, switched on and off the main valve of the instrument starting the flux;

- the **Motor Control** tab controlled the micro-metric motor allowing to move the lens focus along the $z$ axis inside the gap. Here it was possible to write in a text box the increment to get with respect to a defined position. Moreover, there were three buttons: to start the motor, to define a zero position along the $z$ axis ("DH"Define Home) and to go back to the zero position after several movements ("GH"Go Home);

- from the **Command Sequence** tab it was possible to start a command sequence. In fact, clicking on the "Run Seq"button all the commands listed in a dedicated file were run sequentially. The file name had to be inserted in the dedicated text box present in this tab. Through this file, we could execute in sequence any kind of operation;

- with the tab **Expert Only** it was possible to directly execute an operation connected with the other tabs by writing the command to be

sent to the database in dedicated windows. This tab was introduced in debugging phase.

### 4.4.2 The MySQL Database

A MySQL database was used to make possible the communication between the GUI and the DAQ-DCS loop and to record all the informations concerning the measurements. The database was resident on a local server and it was available through the TCP/IP protocol by mean of an username and password.

In this database data were organized in tables where every column was a "*field*" and each row was a "*record*". Using a "*query*" command it was possible to modify or to add a record and to select a data group for analysis. There were three tables: *flags*, *dcs*, *data*.

The **flags** table consisted of four fields that were modified by the GUI and readout by the DAQ-DCS loop. The fields were: "keyflags", "DAQtodo", "DAQstatus", "DAQcommand". The "keyflags" is a primary key whose value can not be changed and univocally identify every row respect to the others. This table has only one record that is identified by the primary key.

The field "DAQtodo" identifies the instrument to be controlled. Here, we could insert the following commands: *HVRPC* or *HVPHOTO* for the HV channels, *OSCILL* for the oscilloscope, *GAS* for the gas controller, *MOTOR* for the micro-metric motor and *STOP* for the loop closing. Finally, the "DAQstatus" and "DAQcommand" fields were used for the command strings.

In the *data* and *dcs* tables all the data collected by the DAQ-DCS loop were recorded. In the **dcs** table there were 30 fields where all the informations coming from: the HV channels (ON, OFF, TRIP Status, HV set, HV readout), the gas controller (ON, OFF, gas percentage), the environmental parameters probes (pressure, temperature, humidity), the micro-metric increment along the $z$ axis, etc could be recorded.

In the **data** table the informations regarding the first and the last event of a data acquisition run were stored. For each run the recorded information were: date and time, oscilloscope setting, waveforms, run number, comments and the output file name where the informations of all the events of the run were recorded.

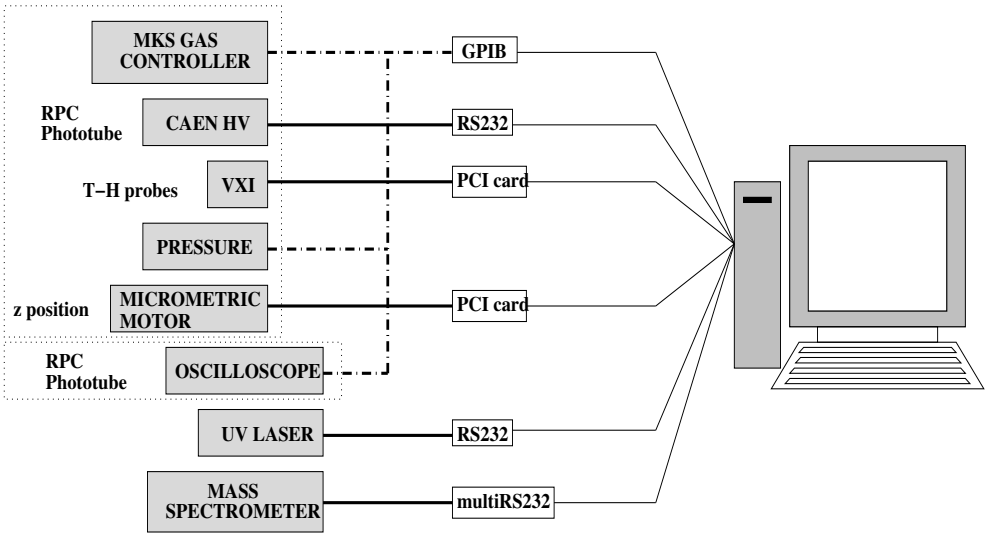


Figure 4.14: *Hardware components connection to the PC.*

### 4.4.3 The DAQ-DCS Loop

As said before, the DAQ-DCS loop runs on a Windows-PC and it is interfaced directly to the hardware components through the computer itself by mean of dedicated boards. In the computer, in fact, some slots are present where it was possible to locate different boards for instrumentation control. In Fig. 4.14 is presented a scheme that shows the connection between hardware components and the computer. The Multi gas Controller, the pressure controller and the oscilloscope communicate with the computer through a GPIB board (General Purpose Interface Board), the HV crate and the UV laser through a RS232 card and finally the VXI and the micro-metric motors are controlled through a PCI card.

The DAQ-DCS loop was reading out continuously the command from the database in "flags" table. Every time it was finding new strings, it executed the command of the corresponding instrument. This program, written using the *C++* language, was executable from Windows by using the Microsoft Visual C++ platform. At the program startup, a connection with the MySQL server and to the hardware components was performed. At this point the program started an infinite loop waiting for database commands. When, from the GUI, a new run command string was ready (see Sec. 4.13), the

DAQ-DCS loop read it and saved the oscilloscope waveforms in a file. In this data file, event by event, all the informations needed for the correct decoding of the signals were recorded. This was done in order to allow for an easy off-line data analysis. The file was consisting of several blocks. An *Haeder Run* described the run itself and held the oscilloscope *preamble* containing all the setting parameters needed to correctly decode the waveforms in the off-line analysis. This was followed by the event-blocks. Each event consisted of an *Haeder Event* with the oscilloscope channels information and an *Haeder Channel* followed by the signal sampling vector. As specified in the previous sections, the informations from the first and the last event were also saved in the "data"table of the database.

During the data acquisition, the DAQ-DCS loop saved in the "dcs"database table all the useful informations coming from the instrumentation. This procedure was performed each minute to take into account the pressure and temperature variations in order to adjust the HV applied to the RPC electrodes.

### 4.4.4 The Off-line Software Analysis

The DAQ-DCS loop produces a binary file that is saved for the off-line analysis. In order to study the parameters of the gas mixture, we needed to derive the drift time and the RPC signal amplitude. This was done by using a custom software written in *C++* and using the *ROOT* package consisting of two distinct parts: signal decoding and waveforms analysis.

The first part decoded the waveforms of the binary files acquired during the run and recorded the informations in histograms that can be read out by a *ROOT* macro. Using this macro, it was possible, after performing a Fourier analysis of the signals, to remove a noise correlated with the pulse laser that we could not shield, to obtain the drift time and the signal amplitude for each ionization event in the RPC. The filter was applied by using the Discrete Fourier Transform (DFT) through the Fast Fourier Transform (FFT). Form the FFT frequencies spectrum, only frequencies lower that a chosen cutoff were selected. At this point the inverse Fourier transformation (IFFT) was applied. The filter cutoff value was 280 MHz and it was chosen after a dedicated preliminary analysis in order to not to introduce any signal distortion.

# Chapter 5

# Experimental Results

## 5.1 Introduction

In this chapter we describe the measurements of the basic ATLAS RPC gas mixture parameters, such as electron drift velocity and gas amplification and we analyze and discuss charge spectra. The gas mixture consists of 94.7%$C_2H_2F_4$+5%$C_4H_{10}$+0.3%$SF_6$ and it was studied for the first time by direct measurements using the localized laser spot as ionization source.

The experimental results reported in this section have been obtained with the RPC II prototype. In a dedicated section measurements performed on RPC I prototype are shown and compared with results from RPC II.

As already mentioned in Sec. 4.3.3 all measurements refer to high voltage corrected, in real time, for the environmental temperature T and pressure P changes.

## 5.2 Electron Avalanche Signal

As discussed in chapter 3, the induced current $i$(t) on the RPC readout strip is the charge image of the avalanche charge $q$(t) which grows in the gas and drifts towards the anode. The two quantities are related by the formulas 3.19 and 3.20, discussed in chapter 3:

$$i(t) = k\frac{v_D}{g}q(t) \tag{5.1}$$

where $k$ is the "k-factor", $g$ = 2 mm is the gas gap thickness, $v_D$ is the electron drift velocity and $q$(t) is the total avalanche charge at time t.

We consider negligible the longitudinal avalanche spread, due to the electron diffusion, and the contribution to the induced current of the positive and negative ions drift. In this approximation the current should abruptly terminate when the avalanche reaches the anode. Consequently, from the current maximum is possible to estimate the total avalanche charge $q(t_D)$ and the drift time $t_D$:

$$q(t_D) = \frac{g i_{peak}(t_D)}{k v_D} \tag{5.2}$$

It's possible, considering the amplifier gain $G$ and its termination $R$, to calibrate the peak voltage $v_{peak} = v(t_D)$, measured by recording the signal waveform, in term of the total avalanche charge $q(t_D)$:

$$q(t_D) = \frac{g}{k v_D} \frac{v_{peak}}{GR} \approx 5.52 \left[\frac{pC}{V}\right] v_{peak} \approx 3.4 \times 10^7 \left[\frac{e^-}{V}\right] v_{peak} \tag{5.3}$$

where we have assumed $v_D = 145$ $\mu$m/ns according to the drift velocity results presented in Sec. 5.4. The electronic noise at the output of the amplifier was about 10 mV which corresponds to about 0.05 pC ($= 3.4 \times 10^5$ e$^-$) equivalent noise charge, at least two order of magnitude below the Raether limit of about $10^8$ e$^-$ and well below the saturated avalanche charge of about $10^7$ e$^-$, characteristic of signal in our operating regime.

Fig. 5.1 shows a typical signal waveform corresponding to an avalanche initiated by a laser pulse in single ionization condition reached by finely reduce the beam intensity as described in Sec. 4.3.6. It is possible to notice how the signal follows, approximately, a simple exponential law in the rising part. The electric signal doesn't change abruptly after the maximum is reached. This can be due to several factors as for example, to the transfer function of the readout system, which is a complicated interplay between different parts: the graphite layer, the metal strips and the amplifier. Actually, an exhaustive and detailed explanation of the waveform features involves complex phenomena, but these phenomena have a modest impact on the extraction of the electron transport properties.

## 5.3 Laser Ionization Source Set-up

Fig. 5.2 shows the geometrical configuration of the RPC irradiated with the laser light. The laser beam light was focused inside the 2 mm height gas gap

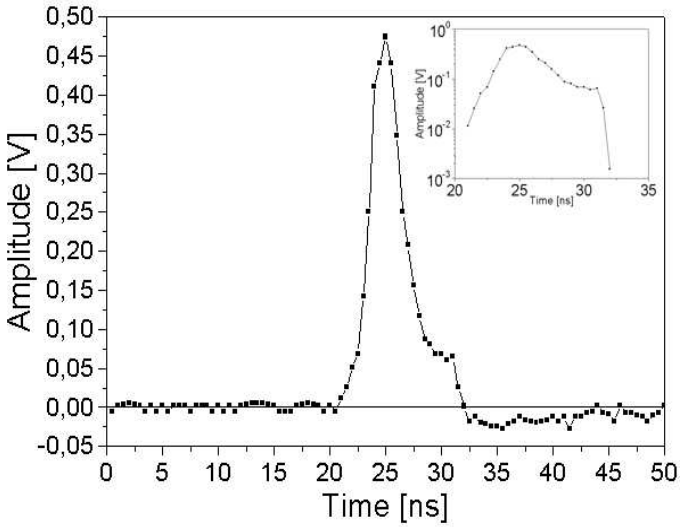


Figure 5.1: *Typical signal waveform. The plot in the inset shows the same waveform in semi-logarithmic scale. The nominal position respect to the anode is 1.5 mm and the applied high voltage is 10700 V.*

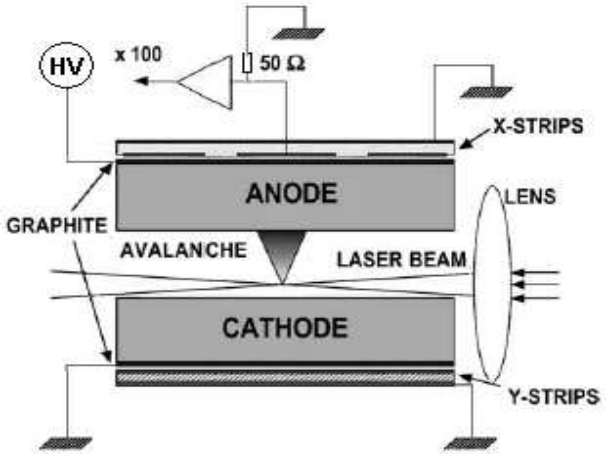


Figure 5.2: *Side view of the RPC laser irradiation setup.*

into a $\sim$ 20 $\mu$m spot. The lens focus was positioned in the RPC center and this could limit the vertical spot excursion ($z$ axis in Fig. 4.2) of the laser spot up and down from the gas gap center. In fact, the beam light could touch the Bakelite electrode and photo-electrons could be extracted from the RPC boundary. The pick-up strip used to readout the avalanche signal was orthogonal to the beam light and located in the RPC center, in order to avoid pick-up signals induced by phenomena along the beam light but far away from the spot center, such as photo-electrons released in the gap.

Electron-ion pairs were generated in the gas gap with a probability proportional to the square of laser light intensity (see section 4.3.6), than the ionization rate decreased quickly with the distance from the lens focal point. For small enough laser light intensity a measurable ionization rate was obtainable only in the light spot position, i.e. a well localized ionization in the gas gap. A possible disadvantages of having such localized ionization in presence of high gas amplification was that we collected electron avalanches always in a very small area of the detector electrodes, just above the laser light spot. This could compromise the RPC rate capability, by generating a local reduction of the electric field, which changes the detector working conditions in proximity of the detection point. In fact, the Bakelite electrode has a recovery time of $\sim$ 1 ms (see Eq. 3.22), which is related to the finite Bakelite volume resistivity. If the hit rate is very high, the Bakelite electrodes can not completely recover the electric field between two consecutive electron avalanche multiplication. A new stationary condition is obtained where the effective electric field is lower with respect to the electric field applied to the electrodes.

However, the reduction of the collected charge makes the lowering of the effective electric field less pronounced and the fine tuning of the laser light intensity by mean of optical filters, described in Sec. 4.3.6, to work in single ionization regime had also this purpose. Finally, in average, one ionization per pulse should be generated and the signal must exceed the electronic noise levels. Analogously, alternative way to avoid to reduce the local electric field is to limit the laser repetition rate. Using a set of optical filter it was possible to reduce the laser beam intensity to prevent systematic errors in the gas parameter measurements.

During the laser conditions setup procedure, the average signal amplitude and the measured electron arrival time have been measured as a function of the laser repetition rate and using an optical filters characterized by a transmittance T. Fig. 5.3 shows the results of this measurement. The optical

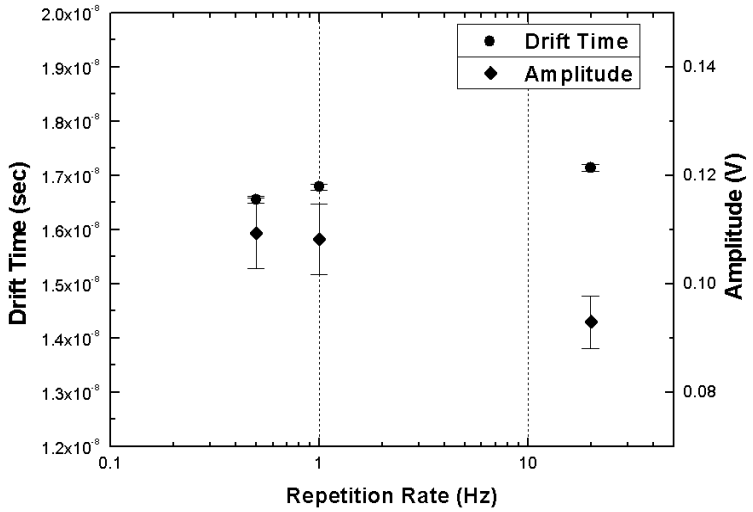


Figure 5.3: *Average signal amplitude and measured electron arrival time as a function of the laser repetition rate, for HV = 10300 V and ionization spot position in the gap center. The optical transmittance of the optical filter used for these measurements was 10%.*

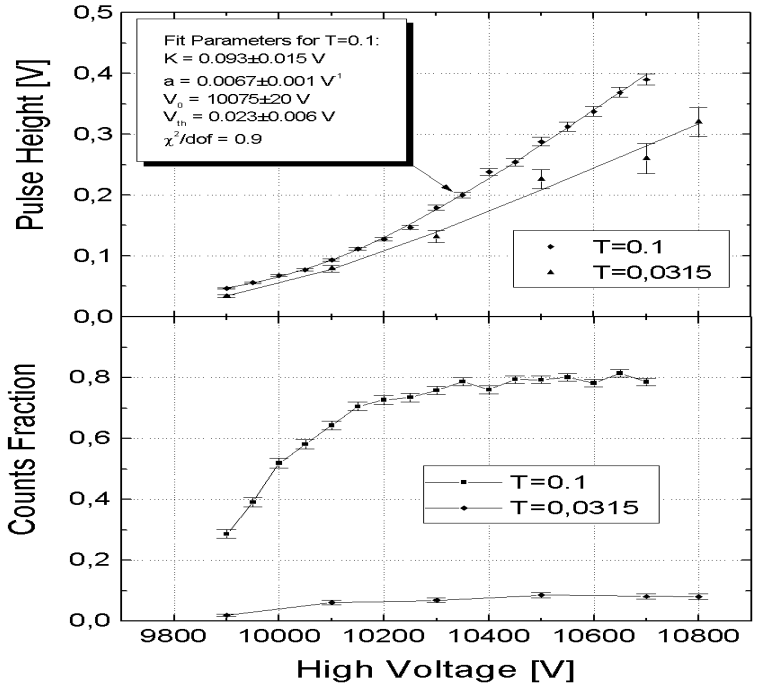


Figure 5.4: *RPC mean pulse height (upper plot) and RPC counts fraction (lower plot) versus applied high voltage for two different optical filters with optical transmittance T. Superimposed are the fits obtained by the logistic cumulative function described in Sec. 5.6.1. Data are taken with ionization spot located at 1500 µm from the anode.*

filter used in this case had a 10% optical transmittance and the position in the gap was the same for all the measurements. Increasing the repetition rate we observed a decrease of the signal amplitude and an increase of the measured arrival time. This can be easily explained assuming that the local effective electric field gradually decreased with increasing laser repetition rate thus producing a lower gas gain and larger drift time of the electrons to the anode.

Fig. 5.4 shows (lower plot) the fraction of events where an avalanche was detected using a 10% and a 3.5% trasmittance optical filter, for different values of the applied high voltage. For both optical filters is possible to notice a plateau in the counting fraction for large enough high voltage values. The plateau counting fraction was interpreted as the product of the RPC

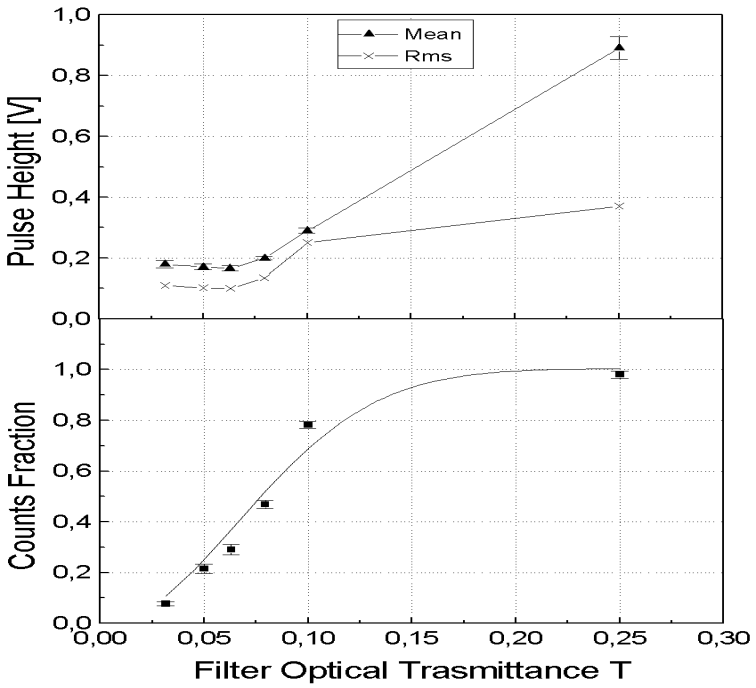


Figure 5.5: *RPC mean pulse height and rms pulse height (a) and RPC counts fraction (b) versus optical filters transmittance T. Superimposed is the fit related to the Poisson's statistics (Eq. 5.4). Data are taken with HV = 10500 V and ionization spot located at 1500 $\mu$m from the anode.*

collection efficiency and probability to have at least one laser pulse ionization. Since we expected a RPC full collection efficiency of about 1, we concluded that the missing counting fraction was the probability that a laser pulse didn't ionize.

For completeness, Fig. 5.4 shows (upper plot), for the same set of runs, also the mean of the pulse height distribution versus the high voltage, for both filters.

Assuming that the probability P(n) to have n ionization per laser pulse is Poisson distributed:

$$P^{\mu}(n) = \frac{e^{-\mu}}{n!}\mu^{n} \tag{5.4}$$

where $\mu$ is the average number of ionization, which is a characteristic of the laser, optical system set-up and gas mixture (it can also depend on gas impurity types and concentration). Since the two-photons ionization process scale quadratically with the light intensity, $\mu$ can estimated by the following formula:

$$\mu = \mu_0 \times T^2 \tag{5.5}$$

where $\mu_0$ is the average number of ionizations without optical filters and T is the filter optical transmission coefficient. The probability to have no ionization is $P^{\mu}(0) = e^{-\mu} = 1 - f$ where $f$ is the probability to have at least one ionization.

To characterize the laser source for our purposes we have to estimate experimentally the number of ionizations produced by the laser spot. To extract this value we work with the RPC at HV = 10500 V, which from Fig. 5.4 correspond to full efficiency detection. Fig. 5.5 shows (lower plot) the counts fraction as a function of the optical filter transmittance with the fit of $f$ = 1 - $P^{\mu}(0)$ = 1 - $e^{-\mu}$ superimposed. It turn out from the fit that the average ionization rate of the source is $\mu_0 = 115 \pm 20$ $e^{-}$ per pulse. For completeness, Fig. 5.5 shows (upper plot), for the same set of runs, also the mean and the root mean square of the pulse height distribution.

As suggested by Fig. 5.3 and Fig. 5.5, we finally decided to perform all the drift velocity measurements setting the laser repetition rate to 1 Hz and using an optical filter with 10% transmittance. This choice has been

motivated by a compromise between the necessity do not bias the electric field in the gas keeping rate capability, together with the need of performing a complete set of measurements in a reasonable time ($\sim$ 10 hours for each electric field value).

## 5.4 Electron Drift Velocity Measurements

The method is based on the determination of the electron drift time distribution $\Delta$t, given by the difference $T_1$ - $T_0$ , where $T_1$ is the time of the pick-up strip signal maximum (which is related to the arrival time of the electron avalanche on the anode) and $T_0$ is the photo-tube trigger time (which is related to the arrival time of the laser in the ionization region).

For each fixed electric field value, five measurements have been performed varying the ionization position along the $z$ axis inside the gap (see Fig. 5.2 and Fig. 4.2). The ionization region along the gap spanned by the measurements was 400 $\mu$m long with step of 100 $\mu$m between two different measurement points. The spanned region has needed to be accurately chosen. In fact, the avalanche signal grows as a function of the distance from the anode, due to the longer amplification path. Therefore, the ionization occurring in a region too much close to the anode produced a signal that can not be resolved from the amplifier noise. On the other hand, it was not possible to ionize in a region too much close to the cathode because undesirable board effects can raise, as for example, photo-emission electrons from the electrode. The drift measurements were performed in a region between 1400 $\mu$m and 1800 $\mu$m from the anode, for a high voltage value of 9900 Volts, and between 900 $\mu$m and 1300 $\mu$m from the anode, for a high voltage value of 10700 Volts.

The high voltage applied to the electrodes ranged from 9900 V to 10700 V, referred to standard condition of temperature and atmospheric pressure. Within this high voltage range, we could scan from RPC low efficiency regime up to RPC full efficiency regime (see Fig. 5.4).

Fig. 5.6 shows the monitored temperature, atmospheric pressure and applied high voltage during a typical run. The applied voltage was slightly lower than the set voltage (in this case the normalized voltage is 9900 Volts) due to the temperature and pressure correction.

By performing the waveform analysis, for each run, we got the drift time and the signal amplitude on event by event basis. Fig. 5.7 shows

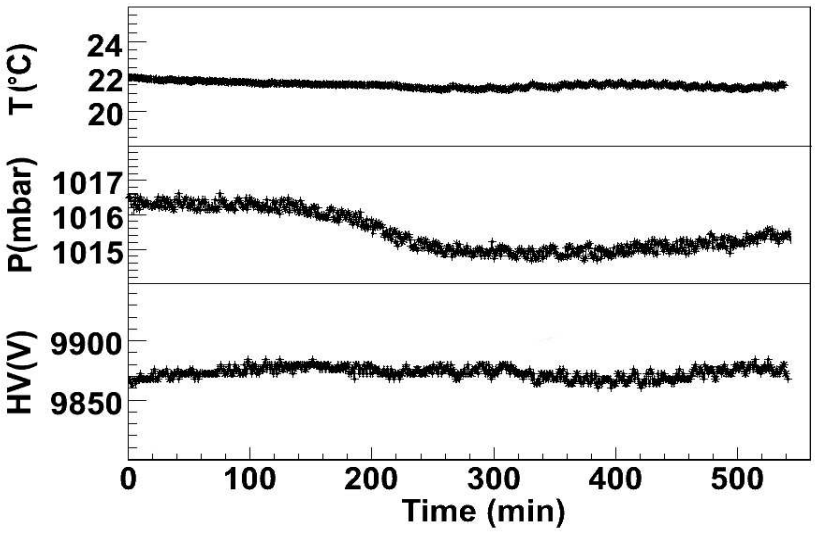


Figure 5.6: *Environmental temperature, atmospheric pressure and applied high voltage evolution during a run. The normalized high voltage was here set at a value of 9900 V.*

the obtained drift time and amplitude during a typical run. It is possible to see that the drift time and the pulse hight values appear stable and uniformly spread around a constant mean value. This is a further confirmation that no long term effective electric field reduction effects were present. Completely different conclusions have been reached by analyzing results from RPC I prototype (see Sec. 5.5).

### 5.4.1 Results and comparison with MAGBOLTZ

For each applied high voltage five runs have been collected, corresponding to five different positions of the laser spot from the anode. For each run we determined the drift time distribution. Fig. 5.8 shows three of these distributions obtained at two different positions, but at the same high voltage, and at two different high voltage, but at the same position. It is worth noticing that the time distributions were almost perfectly Gaussian, with no relevant tails.

The time resolution was mainly due to the electron diffusion. Other contributions come from the time resolution of the oscilloscope, the laser

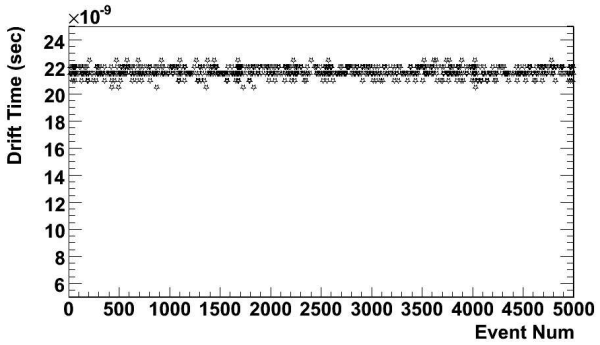


(a)

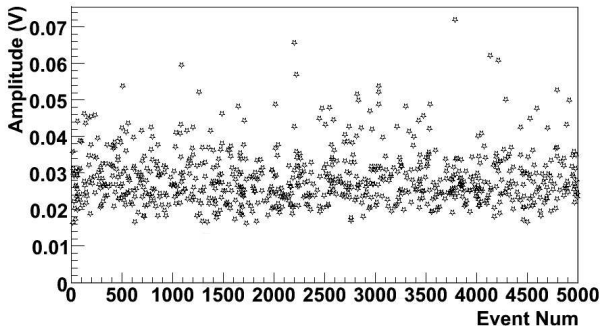


(b)

Figure 5.7: *Electron drift time (a) and signal pulse height (b) during a run. The high voltage applied was 9900 V.*

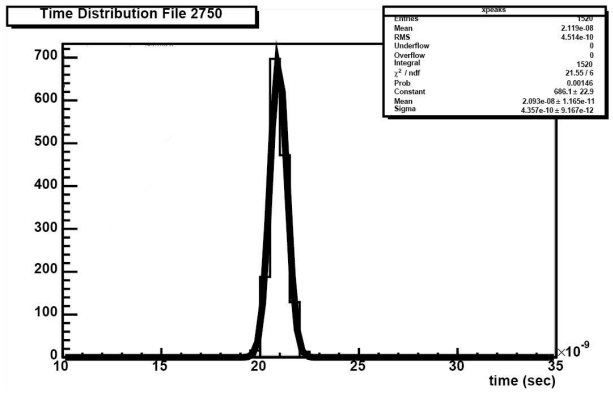


(a)

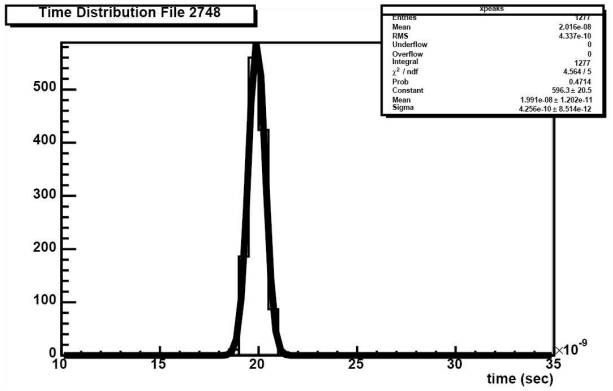


(b)

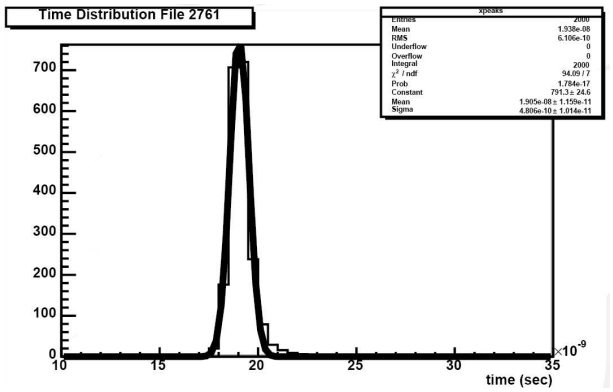


(c)

Figure 5.8: *Distribution of the electron drift time. (a) 1500 µm from the anode and HV = 10300, (b) 1300 µm from the anode and HV = 10300 and (c) 1300 µm from the anode and HV = 10700.*

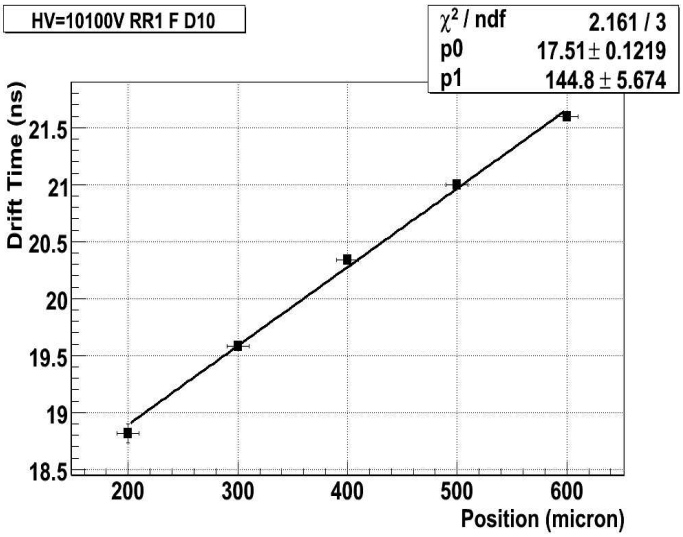


Figure 5.9: *Electron drift time versus drift distance for HV = 10100 V. The drift velocity is obtained from a linear fit to the experimental points.*

pulse duration, photo-tube resolution and electronic noise. The Gaussian fit of the distributions together with the fit parameters are also presented in Fig. 5.8. From the mean of the Gaussian fit we got the time taken by the avalanche to drift from the ionization point to the anode. The values of these drift times were plotted versus the corresponding ionization positions. The drift velocity, for any given value of the drift field, was measured by the slope of the linear fit to the experimental points. One of these linear fits is shown in Fig. 5.9, where it is possible to see that the straight line nicely interpolate the experimental points. The resulting drift velocity values as a function of the applied electric field are shown in Fig. 5.10.

As a meaningful test of stability and reproducibility of the drift velocity measurements we also repeated the measurements for two values of the electric field after several months. The two set of measurements, corresponding to an electric field value of 51.5 kV/cm and 52.5 kV/cm respectively, are plotted on Fig. 5.10 as well (EXPERIMENTAL RESULTS II), showing a satisfying consistency with the previous ones.

In the same plot the MAGBOLTZ results from the calculation of the drift velocity are also reported, in order to facilitate the comparison. As we can see there is a good agreement between simulation and experimental results.

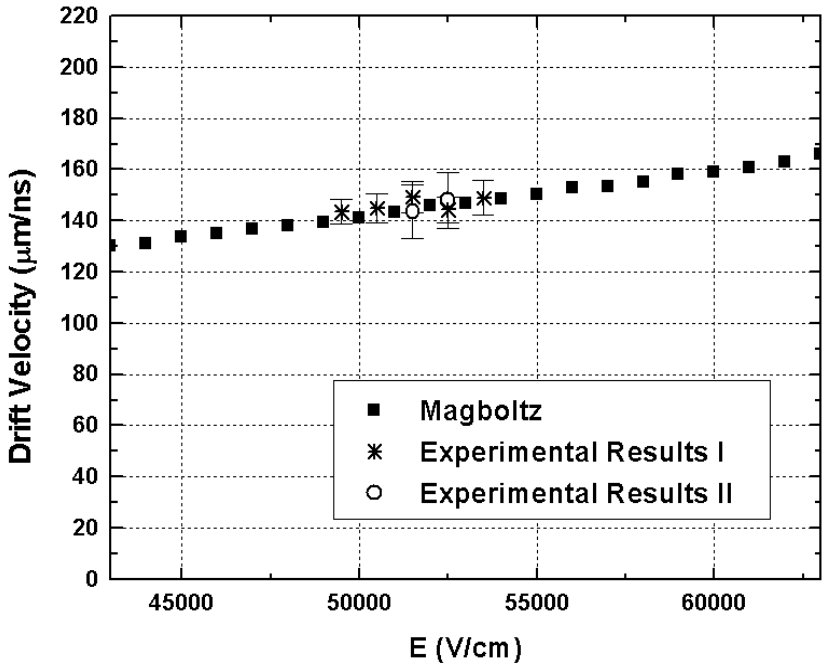


Figure 5.10: *Comparison between the drift velocity measurement results and the ones computed by the program MAGBOLTZ. The composition of the gas mixture under study was 94.7%$C_2H_2F_4$+5%$C_4H_{10}$+0.3%$SF_6$.*

The contributions to the error in determining the drift velocity come from:

- error coming from the linear fit that takes into account the statistical uncertainties on the mean of the drift time distributions, which includes also the spread of the ionization position;
- error propagation on the electric field;
- error propagation on the atmospheric pressure and temperature measurements

All these contributions were quoted and finally quadratically summed to get the error on the drift velocity determination. It was found that the contribution coming from the statistics is ∼3-4% while the one coming from the electric field and the environmental parameter is ∼2%.

## 5.5 RPC I prototype measurements: a good lesson

A similar set of drift velocity measurements has been performed also using the RPC I prototype. In this case, the voltage applied to the electrodes has been varied from 10500 V to 11100 V.

All measurements described in the previous section were performed for the RPC I prototype with the same laser setting described before. In particular, also in this case the time distributions were almost Gaussian, with no relevant tails. The drift velocity results as a function of the electric field are shown in Fig. 5.11, together with the MAGBOLTZ calculations. We can observe that the results are not in good agreement with the calculations, no the absolute values neither the trend with respect to the electric field. We related this behavior to two different mechanisms: the large volume resistivity and the low content of humidity in the Bakelite electrodes of RPC I.

As specified in the previous chapter, one of the difference between the two prototypes was the fact that the RPC I prototype had a Bakelite resistivity one order of magnitude higher than the RPC II. This means that in the RPC I prototype case the Bakelite recovering time was much more longer. The time needed to the electrodes to get charged again was so long with respect to the ionization rate that it was impossible to have a stationary condition for the electric field. In this case, also for very low laser repetition rate the electric field get locally reduced. In Fig. 5.12 the drift time and the amplitude values obtained event by event during a run for the RPC I prototype are shown. We can easily observe that during the run the average drift time increased, while the average amplitude decreased. This is the typical effect we expect to find in case of electric field reduction.

It is important to underline that the conduction mechanism of melamine-phenolic sheet [58], from which the Bakelite is made of, is likely based on $OH^-$ carriers. The Bakelite concentration of $OH^-$ is related to the humidity of the surrounding environment and in particular condition can be very low (dry Bakelite). In this case, the good functionality of the detector is compromised. Often, to avoid this, a 1% water vapor content is added to the gas mixture [59], and the environmental air humidity is kept to about 40 % of relative humididy [60].

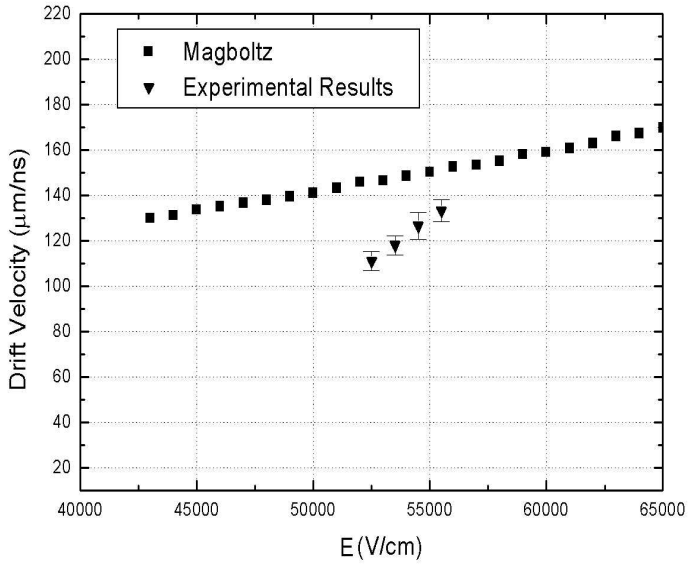


Figure 5.11: *Comparison between the drift velocity values measured with RPC I prototype and the ones computed by MAGBOLTZ for the gas mixture under study.*

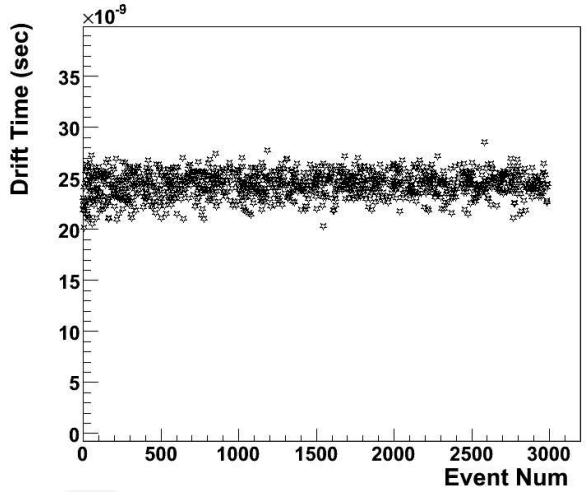


(a)

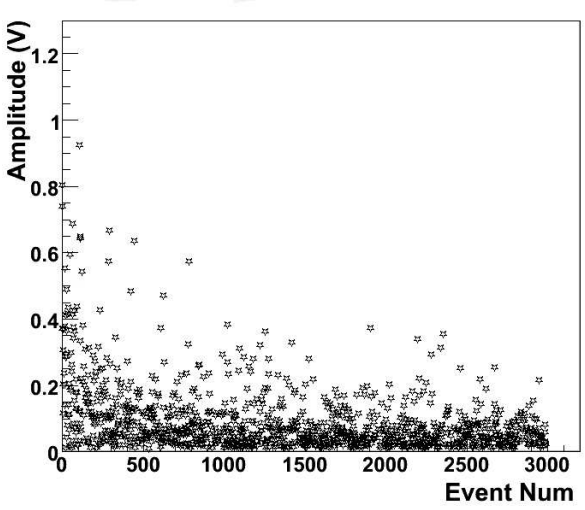


(b)

Figure 5.12: *Electron drift time (a) and signal pulse height (b) during a run for RPC I prototype. The applied high voltage was 10700 V.*

## 5.6 Gas amplification Study

In literature several works are devoted to simulate the RPC behavior changing gas parameters and gap geometry. The main goal is to predict the RPC efficiency and time resolution in detecting minimum ionizing particles ([1], [2], [61]). Some basic input parameters to the simulations are the electron drift velocity and the effective Townsend coefficient. In particular, time resolution is related to the first parameter, and detection efficiency to the second one.

In this section we report on the gas gain amplification and charge spectra measurements in RPC II prototype. Similar measurements have been done by several authors using cosmic rays ([2], [51], [62], [63]). In our setup we had the unique feature to accomplish these studies in a simpler condition than with cosmic ray. In fact, the laser source generates electron avalanche in a well localized position, while with cosmic rays the signal is given by the contribution of several avalanches initiated by primary ionization electron clusters. The clusters are released in the gap following the Poisson's distribution with average $\lambda$ ($\approx 9.5 \frac{clusters}{mm}$ for ATLAS RPC gas mixture), thus giving a large fluctuations in the readout signal just because the avalanches starting position fluctuates.

### 5.6.1 Saturated Avalanche Regime

In Fig. 5.4 (upper plot) the mean and the root mean square of the signal pulse height have been shown with respect to the high voltage and for two different average ionizations ($\mu \approx 1$ and 0.07). The mean pulse height increase with the electric field exponentially for small value, but it begins to saturate (linear growth) for large electric field, just before the efficiency knee. The effective gas amplification change from an exponential growth to a linear growth is attributed in literature [44] to space charge effects induced by the avalanche itself, which start to perturb the external electric field.

Following ref [48] we interpolated the gas amplification with respect to the high voltage using the primitive of the Logistic function:

$$Q(V) = Kln(1 + e^{a(V-V0)}) + Q_{th} \tag{5.6}$$

where K, a, $V_0$ and $Q_{th}$ are fit parameters. We introduced the thresholds charge $Q_{th}$ in order to take into account a positive shift in the average pulse height induced by the software electronic noise suppression (see Sect. 4.4.4).

The meaning of the other fit parameters are explained in quoted reference. Here, we take a more phenomenological approach, but it is important to see how the results of our fit is reasonable good. Also the low gas amplification curve, performed in single ionization mode shows saturation effects (the probability to have more than one ionization is negligible with an optical filter with T = 0.0315). The resulting fit is statistically compatible with the fit of the curve obtained with T = 0.1.

The saturation phenomena defines the so called avalanche saturated regime (see Sec. 3.4.4). It is remarkable how this regime can be described similarly in three apparently different situations: cluster avalanche distributed along a track, few localized electron avalanches and average one localized electron avalanche.

### 5.6.2 Avalanche Charge Spectra

The distribution of the avalanche charge is of paramount importance in order to understand the basic phenomena of the avalanche saturation. In the above mentioned RPC simulation works the charge spectrum of a single avalanche is obtained by theoretical motivated curves or evaluated by Montecarlo simulations with reasonable but "ad hoc"prescriptions. For the first time, by our experimental setup-up, a direct measure is feasible in a controlled environment.

Fig. 5.13 shows the charge spectra measured by changing the optical filter in such a way to compare multiple avalanches spectra with single electron avalanche spectra. The charge spectrum of avalanches generated by several electrons presents an evident and broad maximum. In our example (Fig. 5.13 plot in the inset) the average ionization is about 7 with an RPC efficiency near to one (see efficiency curve of Fig. 5.4 for the same spot location but related to single electron avalanches).

The presence of a peak in the charge distribution is a manifestation of saturation phenomena in charge multiplications. In fact, in a proportional regime an exponential decreasing distribution is expected [64], which can became a similar to the tail of a Polya distribution [65, 66]. Reducing the average number of overlapping avalanches has the effect to produce charge spectra more "clean"and similar to the expectations. In particular, in Fig. 5.13 with an average of one avalanche per pulse the distribution peak disappears and the shape is similar to a Polya distribution. In addition, no change in shape is apparent going from 0.25 to 0.1 average number of

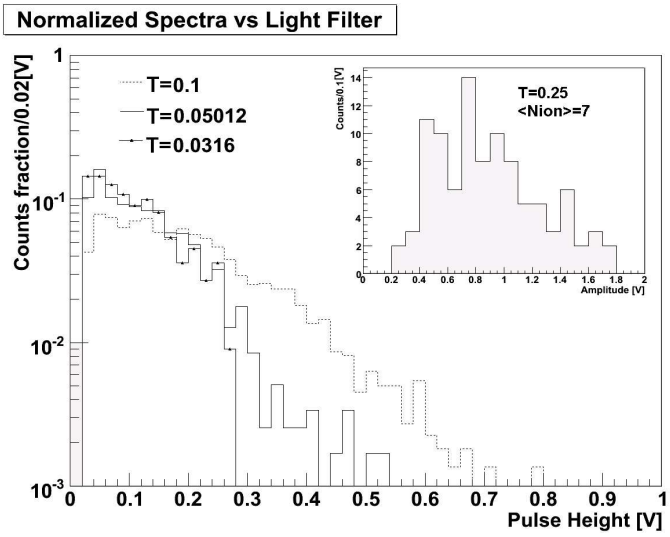


Figure 5.13: *Normalized Pulse Height Spectra for decreasing optical filter transmission coefficient T. The plot in the inset corresponds to an average of about 7 ionizations per laser pulse. The main plots correspond to an average of about 1, 0.25 and 0.1 ionizations per laser pulse. Data were taken with HV = 10300 V and at 1500 $\mu$m from the anode.*

ionization, which is another way to confirm that the single ionization is reached with optical filters with T equal or less than 0.51.

### 5.6.3 Single Avalanche Charge Spectra

From the experimental results shown in the previous section it turns out that the spectrum is strongly altered if we reduce the number of overlapping avalanches. It is important to understand if the multiple avalanches spectrum is the incoherent sum of the single avalanche signals or non linear phenomena take place. It is possible to distinguish between the two cases studying the charge spectra in single avalanche mode for increasing value of the electric field.

In the plots of Fig 5.14 such spectra are shown for 5 increasing value of the gas amplification. According to these measurements the single avalanche charge spectrum changes gradually from an exponential decreasing shape to a Polya distribution. For a further increases of the gas amplification, from the

RPC detection efficiency knee at HV = 10300 V up to full efficiency at HV = 10700 V, the charge distribution becomes relatively flat. The apparency of a flat region in charge distribution is very similar to what exhibited by the spectra of one or two overlapping avalanches (see plot of Fig. 5.13 with T=0.1).

From such a qualitative analysis is possible to conclude that the distortion of the charge spectra is induced by space charge effect. The same charge spectrum distortion is exhibited by the total avalanche development, irrelevantly of the number of initiated avalanche. Likely, for large enough electric field also the single avalanche charge spectra becomes peaked as the spectrum shown in the inset of Fig. 5.13 were the average number of started avalanches were 7.

In order to confirm the previous statement we plotted in Fig 5.15 the spectra obtained in high ionization and multiplication conditions, but gradually reducing the drift space, which means to decrease the total charge. It is possible to see that for small enough drift space, i.e for small enough total charge, the flat spectrum shape follows gradually an exponential decreasing shape. The consequences of this result is that the single avalanche charge spectrum changes moving inside the gas gap. This aspect was not taken into account in the above cited RPC simulations work.

### 5.6.4 Charge Spectra Characterization

In order to characterize in a more quantitative way the three different charge spectra (exponential-like, Polya-like, "flat-region"-like) we collected a sample of high statistics for each one at a fixed laser transmittance (0.1 %) and distance from the anode (1500 $\mu$m) of the laser ionization spot. Fig. 5.16 reports the measured pulse height spectra increasing progressively the applied high voltage value. The plots are shown in log scale, in order to easily identify deviation from an exponential shape.

According to the final consideration of chapter 3 we expect that the charge distribution of a single avalanche in proportional regime, without saturation and secondary effects, has an exponential shape. Taking into account the threshold cut at about 15 mV, which is visible on all the spectra, is possible to see that, for a high voltage value of about 9700 V, the pulse height spectra follow quite well an exponential decreasing shape. Increasing the high voltage up to 9900 V, than increasing the gas gain, the spectra shape deviate from a simple exponential law and a second negative slope in log scale appears

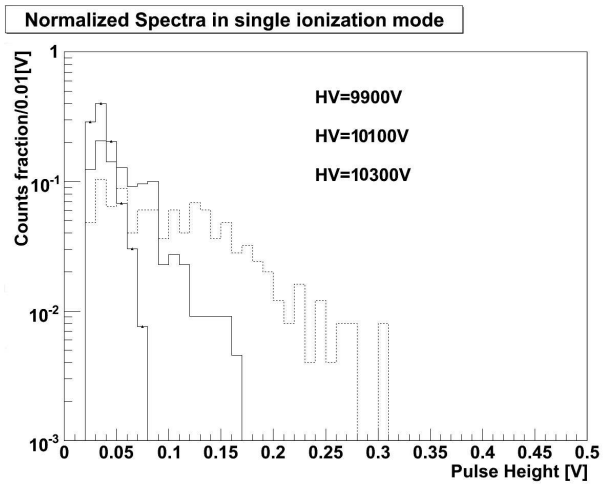


(a)

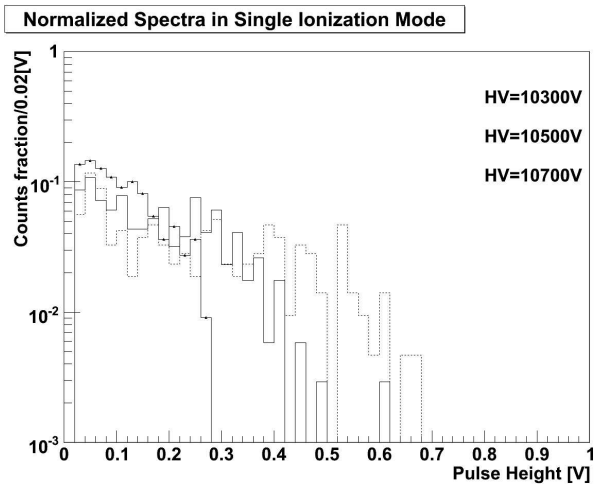


(b)

Figure 5.14: *Normalized spectra in single ionization mode for several value of the high voltages. The upper plot corresponds to lower high voltage values and the lower plot corresponds to higher high voltage values. The data are taken with an average of 0.1 ionizations per laser pulse and ionization spot located at 1500 $\mu m$ from the anode.*

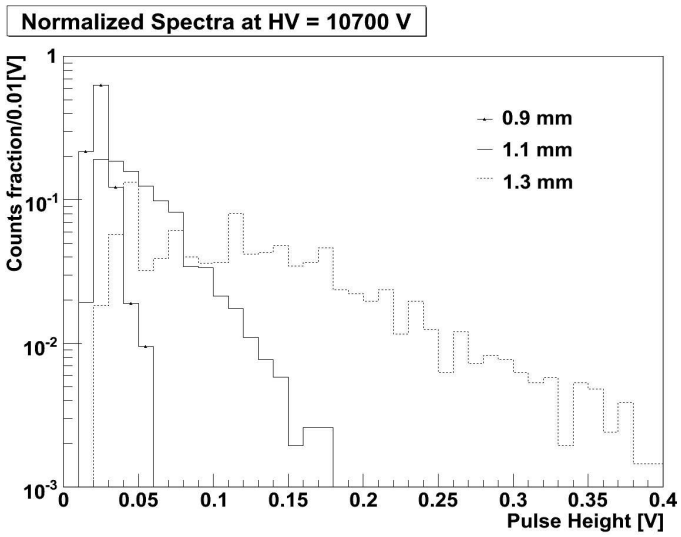


Figure 5.15: *Normalized Pulse Height Spectra for different distance of the ionization spot from the anode. Data were taken with HV = 10700 V and with an average of 1 ionizations per laser pulse.*

clearly. In this regime a deficit of large pulse height avalanche is manifest, which is typical of space charge effects bringing the avalanche to saturation. The change in slope happens at a pulse height of about 0.1 V, corresponding to 0.552 pC ($3.4 \times 10^6$ $e^-$), which is in agreement with expectation.

A further increase of the gas gain, with a high voltage value up to 10300 V, changes qualitatively the spectra shape with an excess of large pulse height avalanche. This is an indication of secondary phenomena. Nevertheless, a concentration of small charge avalanches following an exponential decreasing law is still visible. Likely, these are avalanches which didn't saturate in size, because, due to the statistical fluctuation of the process, they started later to increase. The spectra change drastically after a pulse height of about 0.08 V, becoming almost flat. For pulse height higher than 0.3 V the spectra follow again an exponential decreasing law. It is apparent an accumulation of avalanche charge around 0.3 V where a very loose maximum could be seen. This maximum should become manifest with more total avalanche charge.

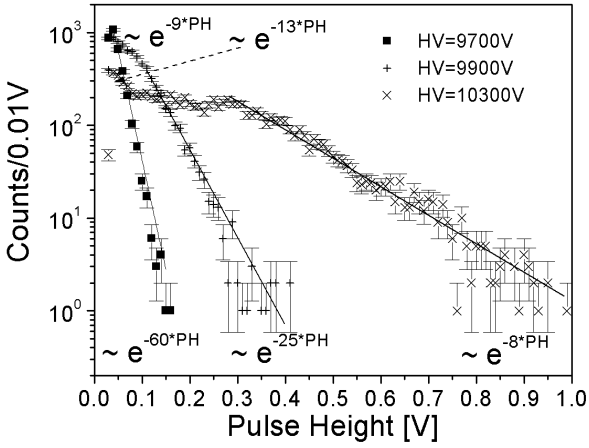


Figure 5.16: *High statistics avalanche charge spectra for different applied high voltages. The avalanche starting distance from the anode is about 1.5 mm.*

### 5.6.5 Measurements of the effective Townsend coefficient

We evaluated the effective Townsend coefficient $\eta = \alpha - \beta$, where $\alpha$ is the first Townsend coefficient and $\beta$ is the attachment coefficient. We began following a traditional method to obtain the charge multiplication coefficient, which can rigorously applied only in a proportional regime. In Fig. 5.17 (a) the mean of the pulse height distribution for each high voltage and ionization spot position used for the drift velocity measurements are shown, together with the counts fraction of each run (Fig. 5.17 (b)). The set of data points corresponding to the same high voltage increase exponentially for larger distance from the anode. Exponential growing curve fits are superimposed on the plot for each data set. In a similar way the detection efficiency increases as well, but of course the counts fraction saturate to about 70 % for the employed optical filter having T=0.1 .

The curve used to fit the average pulse height $< V >$ versus the distance from the anode of the ionization source is given by:

$$< V >= V_{th} + V_0 e^{\eta x} \tag{5.7}$$

where the parameter $V_{th}$ takes into account the threshold cut in pulse height, $V_0$ is the average pulse height at position $x = 0$ and $\eta$ is the effective charge multiplication coefficient. The coefficient $\eta$ extracted with such a method is relatively insensitive to the electric field (see Fig. 5.18 method I). Moreover, its value is about half the effective Townsend coefficient evaluated by MAGBOLTZ. Of course, we are in presence of a saturation effect related to the space charge. Although the average pulse height increases with the electric field the growth is not so fast as expected. In Fig. 5.17 (a) each data point was labeled with the corresponding type of charge spectrum obtained experimentally. It is possible to notice that all curves go through two transitions: the first one to about 0.04 V of average pulse height (exponential to Polya-like spectrum) and the second one to about 0.08 V of average pulse height (Polya to "flat-region"spectrum).

The second method to extract the parameter $\eta$, to compare with MAGBOLTZ calculations, consisted into extract the gas gain in condition where avalanche saturation doesn't occur by fitting the pulse height distribution. This corresponds to use the pulse height distributions corresponding to the data points of Fig. 5.17(a) labeled with "exp". Usually, for each high voltage, there were two position whose data showed an exponential-like spectrum, then in the plot of Fig. 5.18 the results of method II are kept separated for the two positions.

These data points are characterized by small amplitudes and the accuracy in pulse height determination is unsatisfactory. As explained in [66], [67] and [44] a better estimation of the average charge is measuring the slope in semilogarithmic scale of the normalized spectrum. In fact, in this case the spectrum is $\approx \frac{q}{<q>} e^{-\frac{q}{<q>}}$ and from the slope you can extract $< q >$ which is related to $\eta$ by the Townsend multiplication law: $< q >= e^{\eta x}$. The absolute position $x$ of the ionization spot from the anode is known with an uncertainty of about $\pm 0.1$ mm and this introduce a systematic eror in the measurements not repoted in the plot. The coefficient $\eta$ extracted with this method is consistent with the value calculated by MAGBOLTZ (see Fig. 5.18 method II).

### 5.6.6 Avalanche Charge Spectra with no $SF_6$

It was instructive to study the charge spectra of the RPC gas mixture without $SF_6$ in order to learn more about streamer suppressions, even if only qualitative considerations have been drawn out.

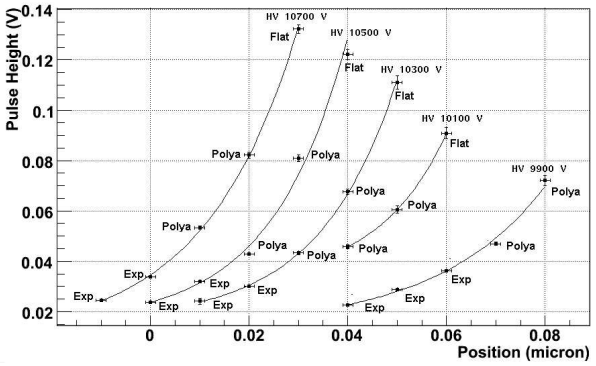


(a)

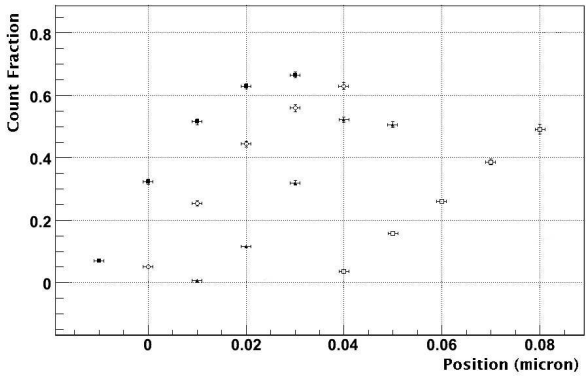


(b)

Figure 5.17: *Mean pulse height (a) and counts fraction (b) for different high voltages and ionization spot distances from the anode. An exponential growing fit is superimposed to the data points. Data were taken with an average of 1 ionizations per laser pulse*

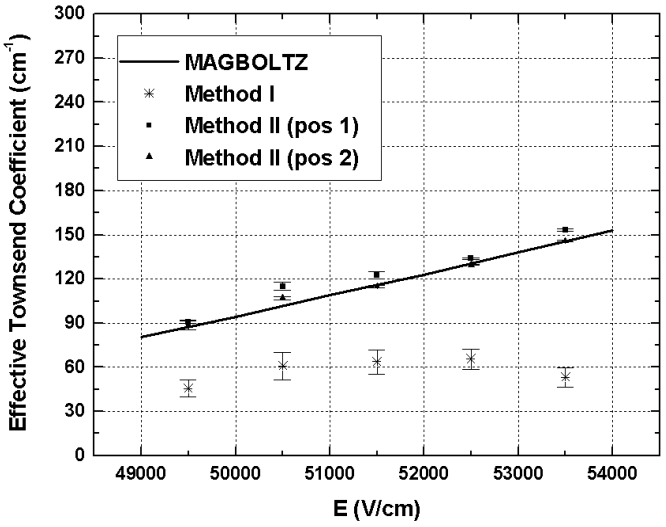


Figure 5.18: *Effective Townsend's coefficient as a function of the electric field, measured according to techniques described in the text. The error reported are statistical only.*

Normalized spectra for such a gas mixture are shown in Fig. 5.19 for a range of high voltage value going from low efficiency to full efficiency. It is possible to see that around the efficiency knee (at about 9700 V) the charge spectra is still Polya like. The data do not show an apparent transition to "flat-region"spectra as observed in presence of a gas which suppress the transition from avalanche to streamers. This is maybe not surprising, since the change in charge spectrum was attributed to space charge effect also streamer suppression is related to the same cause.

## 5.7 Humidified Gas Mixture

All the experimental results presented up to now were referred to a dry gas mixture. The mixture was periodically monitored by mean of the mass spectrometer (see next section) and a negligible water content was detected.

The ATLAS RPC detectors will work with humidified gas mixture. The typical relative humidity will be about 50 % that, in standard conditions of pressure and temperature, corresponds to 12000-18000 ppm (part per million)

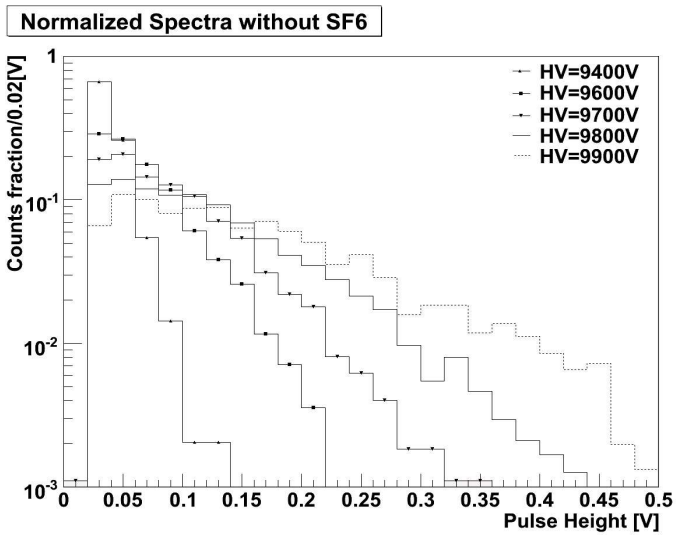


Figure 5.19: *Normalized spectra for several value of the high voltages in a gas mixture without $SF_6$. The data are taken with an average of 1 ionization per laser pulse and the ionization spot located in the gap center.*

of water (1.2-1.8 % absolute humidity). This is a crucial point for the RPC detector aging. In fact, it has been demonstrated that the Bakelite resistivity is very sensitive to humidity [59, 60]. At the very high rate expected in the LHC experiments, a change in the resistivity of the electrodes can noticeably shift the working point. The way proposed to stabilize the resistivity of the Bakelite was to add water vapor to the working gas [59], since flushing dry gas mixture for long time produces an increasing of the Bakelite resistivity bringing to an enlargement in the charge collecting time affecting the detector rate capability.

Very preliminary results on drift velocity with humidified gas mixture have been obtained and are discussed in this section.

To provide an environment with uniform humidity it was added small amount of water vapor. In order to achieve this, the gas mixture bubbled through water bubbler. The humidification system was introduced on the inlet gas line. This was split in two lines: one for dry gas mixture and one for humidified gas mixture, this last line going through a water bubbler. The fluxes of the two mixtures were set by flowmeters allowing to change the final gas humidity level.

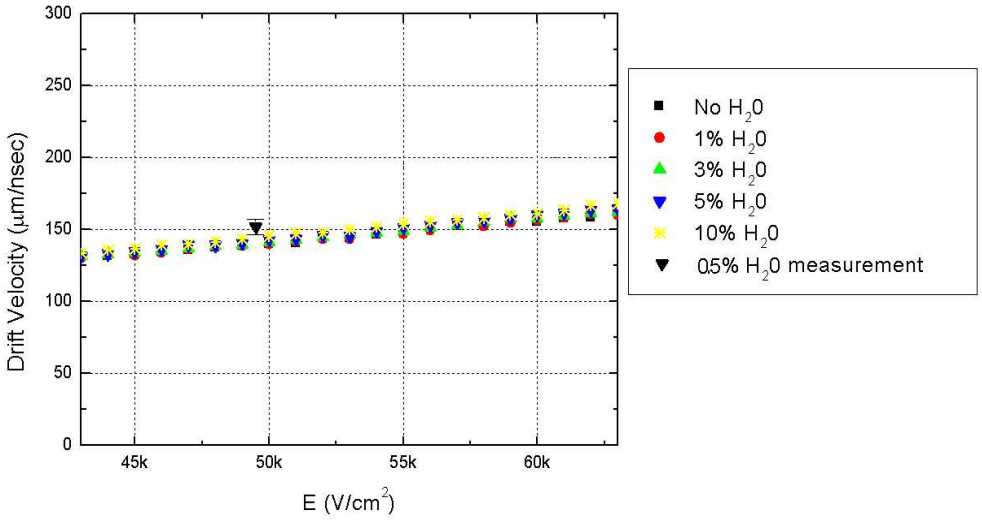


Figure 5.20: *Comparison between the drift velocity computed by MAGBOLTZ and the one measured using a humidified gas mixture. Data were taken with RPC II prototype at 9900V.*

As specified in Sec. 4.3.3, the relative humidity inside the box containing the RPC prototype was read by a probe. The humidity was monitored and the value saved in the database every minute. All measurements were performed using the RPC II prototype.

In Fig. 5.20 we show a drift velocity measurements performed at 99000V with a gas relative humidity of about 19 %. The experimental result is compared with the calculation performed using MAGBOLTZ program for different water content in the gas mixture. The MAGBOLTZ results show that there are not relevant change in the absolute value of the drift velocity up to an absolute humidity of 10%. This results seems to be confirmed by this preliminary measurement of drift velocity with humidified gas.

## 5.8 Mass Spectrometry Measurements

In Sec. 4.3.3, the MINILAB mass spectrometer, connected to the inlet and outlet gas lines of the box containing the detector under study, has been briefly described. A set of measurements in order to check the purity of the

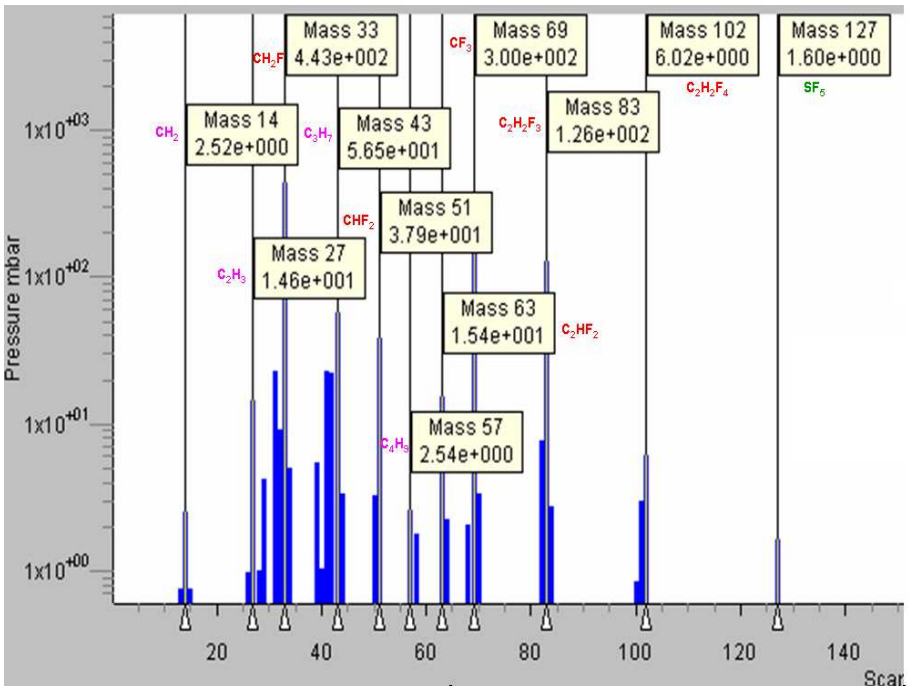


Figure 5.21: *Fragmentation spectrum for the gas mixture at the RPC inlet.*

gas mixture to prevent contaminations has been performed periodically.

In Fig. 5.21 the fragmentation spectrum of the RPC gas mixture is shown. The spectrum presents on the $x$ axis the mass/charge ratio values and on the $y$ axis the relative abundance of the ions. The mass spectrometer performs a full mass/charge scale scan (from 0 to 150 uma, atomic unit mass) repetitively and saves the relative percentages in a file. It is therefore possible to monitor pollution agents present in the mixture by looking for the rising of new peaks in the spectrum not directly related to the gases used.

All measurements performed on the RPC incoming gas have shown that no contaminations were present in the mixture due, for example, to leakages along the lines. All peaks present in the spectrum could be related to the peaks of the reference spectra of each single gas composing the mixture, showed in the previous chapter.

Similarly, the gas mixture coming out from the box has been investigated during the RPC operation. Also in this case no peak uncorrelated with the filling mixture were observed in the spectrum for many hours of normal

operation. than 8 hours of detector operation in normal condition. This technique could be actually used to monitor aging effects in RPC or the gas mixture in particular conditions, like high ionization rate for long period, atc.

In Fig. 5.22 (a) the fragmentation spectrum of the Nitrogen used for the laser is shown. The spectrum is perfectly compatible with the reference one from NIST (Fig. 5.22)(b) but it shows a peak at 18 uma related with the presence of water since to supply the laser gas plastic tubes, absorbing water, instead of stain-steel tubes have been used.

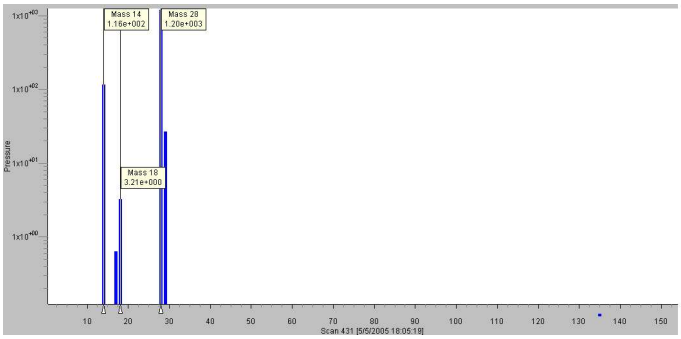


(a)

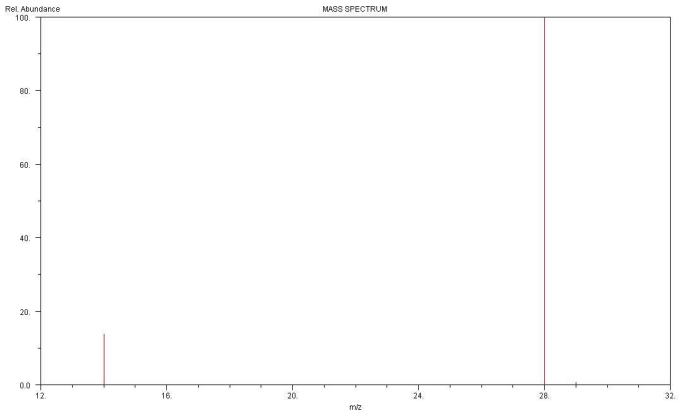


(b)

Figure 5.22: *Fragmentation spectrum for the Nitrogen used to supply the laser (a) and reference spectrum from NIST (b).*

# Conclusions

In this thesis extensive studies of electron transport and amplification properties in the gas mixture filling RPC ATLAS-like have been reported as a function of the electric field in saturated avalanche regime.

Measurements have been performed by using an existing facility exploiting a UV laser source to induce ionization in gas detectros, after a complete re-design of DAQ and DCS system and analysis software.

Results of drift velocity and gas amplification, for different values of the electric field in the mixture: 94.7% $C_2H_2F_4$ + 5% $C_4H_{10}$ + 0.3% $SF_6$ have been obtained. A small size ($10\times20$ cm$^2$) ATLAS-like RPC, having 2 mm gas gap thickness and inner surface linseed-oil-treated Bakelite electrodes with $1.71 \times 10^{10}$ $\Omega$ cm volume resistivity has been used as active detectror.

Electron drift velocities have been compared to the values calculated by the program MAGBOLTZ and a satisfying agreement was found.

The evaluation of the gas amplification was found to be complicated by space charge effects typical of the RPC operating regime of saturated avalanches. We found that the charge spectrum distribution follows an exponential decreasing curve ($\frac{1}{<q>}e^{-\frac{q}{<q>}}$) for electron avalanche charges less than $\sim 10^6 e^-$, while starts to saturate assuming a Polya-like curve shape ($[\frac{q}{<q>}(1+\theta)]^\theta e^{-(1+\theta)\frac{q}{<q>}}$) for larger amount of charge. Further increase of the electron avalanche charge distorts completely the charge spectrum, which exhibits a relatively flat region with a possible broad maximum.

The average signal pulse-height was measured for different distances from the anode of the laser spot and for several values of the electric field. An exponential growth of the average pulse-height was observed with the distance from the anode. The effective Townsend's coefficient, defined as the difference between the Townsend's coefficient and the electron attachment coefficient, was evaluated, as a function of the electric field, at distances small enough from the anode, for which an exponential behaviour of the

charge spectra was still reliable, thus avoiding saturation effects. The obtained effective Townsend's coefficients agree with the calculations from MAGBOLTZ.

Finally, a very preliminary drift velocity measurements has been performed with humidified gas mixture. This was performed in order to setup all devices for collecting systematic measurements with humidify gas mixture in the near future.

# Appendix A

# Special ATLAS RPC Chamber tests at CERN

The barrel muon spectrometer is made of 680 stations arranged radially at about 5, 7.5 and 10 meters from the beam line. Innermost stations are made of two "multi-layers"each housing four layers of MDT tubes. Middle stations are made of two multi-layers of 3 layers each of MDT tubes placed between two RPC planes (so colled Pivot and Low Pt planes). Outer stations are made of two multi-layers of 3 layers each of MDT tubes and one RPC plane (High Pt plane).

Muon stations are organized in 16 geometrical sectors along the azimuthal angle, following the eightfold layout symmetry of the magnetic barrel toroid coils. More precisely, the 16 sectors are subdivided in 8 small and 8 large, according to the position with respect to superconducting coils.

Fig. A.1 shows a typical middle muon station of a small sector. The regions around the coil ribs have a loss of muon coverage of $\sim 3\%$ of the full barrel acceptance for muons coming from the interaction region. This means a loss of efficiency of about 12 % for a full reconstructed four-muon decay of the Higgs boson. In ATLAS it has been decided to recover this acceptance loss by building special RPC units to be placed around the rib coils. The name "special"is referred to the fact that these RPC units are not joined with the corresponding high precision detectors.

In Fig. A.1 is possible to see how the special RPC units are mounted in doublets on aluminum frames and positioned on the rib coil by adjustable brackets. There are two typologies of chambers, S2 units (about $30\times100$ $cm^2$) and S3 (about $60\times100$ $cm^2$). Both units have holes to allow the passage

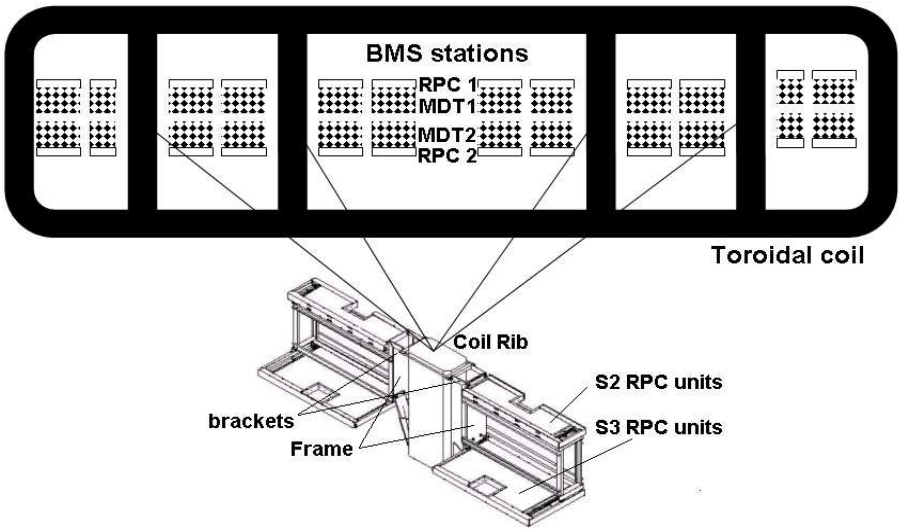


Figure A.1: *location of a special RPC assembly across the rib of the ATLAS superconducting barrel coil.*

of laser beam for spectrometer alignment. The special RPC chambers are located in 6 out of 8 small sectors, this correspond to have 72 S2 RPC units and 24 S3 RPC units. In fact, the inner rib coils are covered with two S2-S2 doublets and the outer rib coil with two S2-S3 doublets. In order to save on the number of electrical and gas connection channels, the low voltage, the high voltage and the gas line distributions are shared with the adjacent muon stations. In addition, the front-end channels reading out the azimuthal strips (non-bending view) are wired-or with the corresponding front-end channels of the adjacent muon station.

The limited access to the finally installed muon detectors in ATLAS imposed several steps of RPC quality assurance. The RPC single units were tested in three test-stands [68] built in Lecce, Naples and Rome "Tor Vergata", where a complete set of noise rate and efficiency measurements was performed using CRT's (Cosmic Ray Teststand) to certify gas volumes and readout strip panels.
All RPC units passing the cosmic rays tests were integrated at CERN in muon stations with the MDT detector and the final electronics.

In Fig. A.2 a special chamber tomography obtained by the Lecce cosmic ray test-stand is shown. It is possible to notice the high detection efficiency

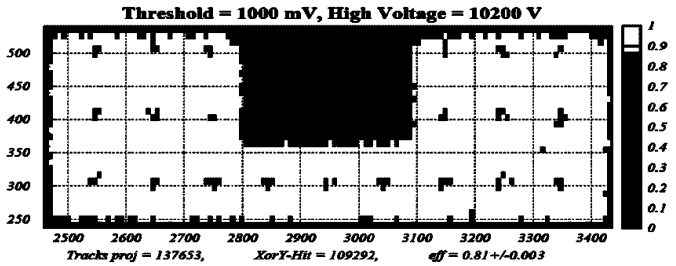


Figure A.2: *An example of a S2 RPC special unit tomography obtained by the Lecce cosmic ray test-stand.*

and the visible dead area are in correspondence of the electrode spacers and frame. Thus meaning that an high quality of the gas volumes is also achieved when shapes more complicated than the rectangular one are realized.

Even if not integrated with MDT chambers, special RPC units were carefully examined before installation to check gas tightness, high voltage isolation and ground stability. These quality assurance tests have been object of the work described in this thesis.

### A.0.1 Leakage Current Tests

The gas volume high voltage electrode is connected directly to the power supply, but the other one is connected to ground by a 100 k$\Omega$ shunt resistor, in such a way that the dark current can be monitored. The dark current $I_{gap}$ can be compared to the current generated by the power supply $I_{CAEN}$. A difference between the two currents is related to a current leak:

$$I_{leak} = I_{CAEN} - I_{gap} \tag{A.1}$$

due to a current path going from the high voltage electrode to ground plane (e.g. mechanical support or strip readout panels ).

The special RPC units showed a leakage current of about 1 $\mu$A at 10 kV. We discovered that this leakage was due to small electrical discharges happening between the inner corners of the gas gap cutout and the readout panel located on the ground electrode. We were able to avoid such a situation inserting a plastic foil between the gap inner corners and the readout panel.

At CERN we measured all the leakage currents applying 9600 kV to the gas gap after flushing gas corresponding to about 10 volume exchanges. In Fig. A.3 the results of these tests were reported for the S2 and S3 special RPC units. From these plots, in which the distribution of the leakage currents among the special units is shown together with the scatter plot between the high voltage power supply current and the gas volume current, it is possible to infer that a high level of electrical insulation was reached ($> 100G\Omega$) .

### A.0.2 Ground Stability Tests

As said in Chaper 3, the avalanche operation mode requires a high gain and high bandwidth front-end electronics. The ATLAS RPC front-end electronics consists of a fully custom VLSI chip in GaAs technology [69, 70]. The readout chip is an eight-channel device where each channel contains a three-stage voltage amplifier and a comparator. The comparator has an adjustable equivalent physical threshold $V_{ph} > 0V$, which is related to the external voltage threshold $V_{th} < 0V$ and to its voltage power supply $V_{ee} = -6V$ by the following formula:

$$V_{ph} = (V_{th} - \frac{V_{ee}}{3})\frac{1}{2A} \tag{A.2}$$

where A is the amplifier gain (about 850) and the factor 2 is due to an input transformer turns ratio. The input transformer is realized directly on a multilayer printed circuit boards, where the chip is bonded unpackaged, and it allows both to invert the signal polarity if needed and to match the input impedance. The acceptable minimum threshold of the comparator is about 50 mV which results in a 50 $\mu$V minimum detectable signal amplitude.

Fig.A.4 shows a schematic representation of the terms involved to determine the minimum settable threshold in the real system. In addition to the intrinsic front-end electronic noise there are noise contributions coming from the surrounding environments such as radio-frequency pick-up and common mode noise (in the figure they are all referred to as 'grounding noise"). The level of the ground noise can be large after chamber integration, where two RPC units are mechanically integrated to realize a trigger plane. Moreover, the front-end channel reading out of pick-up strips of the non-bending view are wired-or together by flat cable in order to save trigger channels. This is possible because the comparator output is realized by an

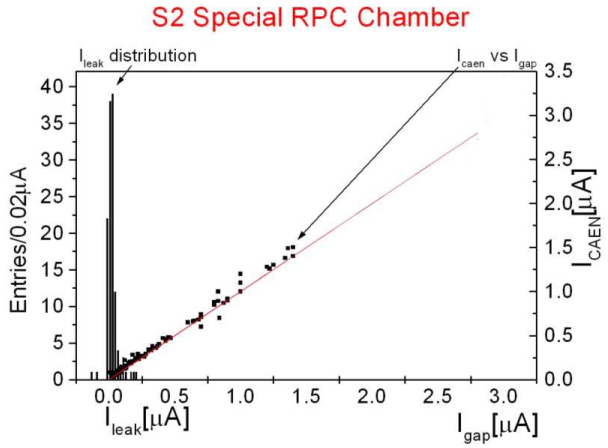


(a)

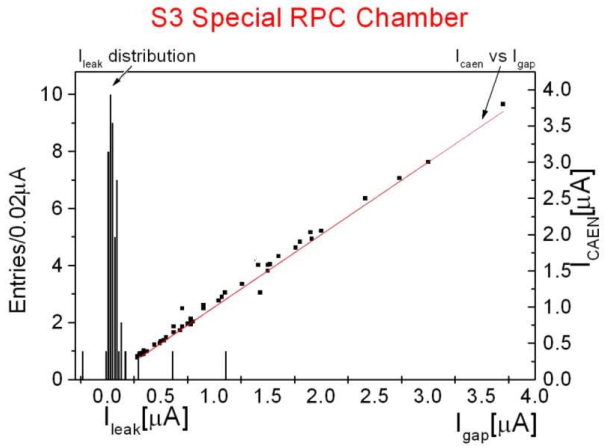


(b)

Figure A.3: *Gas volume leakage current ($I_{leak}$) distribution and power supply current ($I_{CAEN}$) vs dark current ($I_{gap}$) scatter plot for ATLAS RPC S2 and S3 special units. The data were taken at CERN before installation in ATLAS with a high voltage of 9.6 kV*

single ended open emitter configuration, which can drive up to few meter long flat cable. Unfortunately, the one meter long flat cable wired-or solution introduce a negligible grounding noise only if the inner single RPC unit grounding is robust. For this reason, a grounding stability test in a wired-or configuration before installation was necessary.

We did these grounding tests on special RPC units by realizing an 'ad hoc" wired-or configuration between two units and employing the real trigger electronics to terminate the output channels.

The grounding test consisted in the following steps:

1) Set the external threshold to -1.8 V, below the noise level. In this situation all the comparators are always turned on and drawing current, because of the open emitter output configuration.

2) Increase the external threshold at step of 0.1 V and record the $V_{th}$ value at which the excess of drawn current disappears. This mean that the comparators stop to fire.

The $V_{th}$ value at which the electronics stop to fire is an indication of the grounding stability reached by the chambers. We tested in such a way all the 96 special RPC units and we obtained that a the S2 units recover a stable situation at $V_{th} \approx 1.7V$. A value of about 1.5 V was instead obtained for the S3 units. We had to open and fix only 3 units, because we found a too low margin stability.

The ATLAS RPC detectors are fully efficient at $V_{th}$=-1V for minimum ionization particle (see Fig. A.4). Nevertheless, to have a large safety margin, in view of possible noise in the experiment and during p-p collisions, a very stringent test were requiring a $V_{th}$ recovery value not worse than 1.3 V. The special RPC units are well within the requirements.

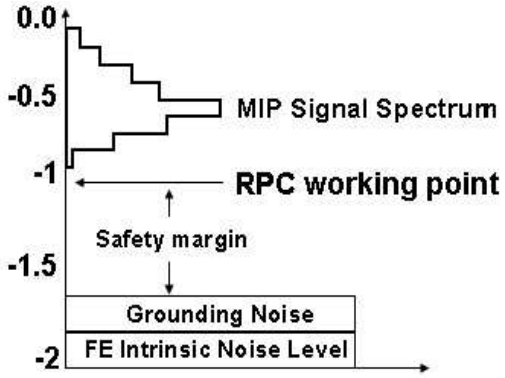


Figure A.4: *Relation between the external RPC voltage threshold $V_{th}$, the electronic noise and the signal of a minimum ionization particle with respect to the front-end discriminator input.* .

# Bibliografy


[1] W. Riegler et al., Nucl. Instr. and Meth. A500 (2003) 144-162.

[2] M. Abbrescia et al., Nucl. Instr. and Meth. A431 (1999) 413-427.

[3] S. Biagi, Nucl. Instr. and Meth. A421 (1999) 234-240.

[4] S. Biagi, MAGBOLTZ, program to computegas properties, version 7.8,, CERN.

[5] *LHC Technical Desing Report*, http://ab-div.web.ch/ab-div/Publications/LHC-DesignReport.html

[6] F. Halzen & A.D. Martin, *Quarks and Leptons: an introductory course in modern particle physics*, John Wiley & Sons, USA (1984).

[7] D. Treille, Physics Reports 403-404 (2004) 221-239.

[8] G. Altarelli, M.W. Grünewald, Physics Reports 403-404 (2004) 189-201.

[9] H.E. Haber, G.L. Kane, Phys. Rep. C117 (1985) 75.

[10] S. Abdullin, C. Kao and N. Stepanof, Univeristy of Rochester UR-1475, July1996.

[11] K.D. Lane hep-ph/9605257 (1996).

[12] S. Coleman, J. Mandula; Phys. Rev. 159, 1251 (1967).

[13] L. Alvarez-Gaume, J. Polchinski and M.B. Wise, Nucl. Phys. B221 (1983) 495.

[14] M. Dine, W. Fischler and M. Srednicki, Nucl. Phys. B189, (1981) 575.

[15] L.Randall and R. Sundrum, Nucl. Phys. B557, (1999) 79.

[16] ATLAS Collaboration. *ATLAS Technical Desing Report.* http://atlas.web.cern.ch/Atlas/Welcome.html

[17] I. Hinchliffe, F.E. Paige , Phys. Rev. D 60, 095002.

[18] W.M. Yao et al. (Particle Data Group); J. Phys. G33 1 (2006).

[19] G.F. Giudice, R. Rattazzi; Phys. Rep. 322 (1999) 419.

[20] CMS Collaboration. *CMS Technical Desing Report.* http://cmsdoc.cern.ch/outreach/

[21] LHCb Collaboration. *LHCb Technical Desing Report.* http://lhcb.web.cern.ch/lhcb/

[22] ALICE Collaboration. *ALICE Technical Desing Report.* http://alice.web.cern.ch/Alice/Alicenew/

[23] N. Ellis, T.S. Virdee, *Experimental challengesnin high luminosity collider physics.* Ann. Rev. Nucl. Part. Sci. 44 (1994) 609.

[24] I. Foster and C. Kesselman (editors), *The Grid: Blueprint for a Future Computing Infrastructure* Morgan Kaufmann Publishers, USA, 1999.

[25] http://lcg.web.cern.ch/LCG.

[26] ATLAS Inner Detector Comunity *Inner Detector Technical Desing Report* http://atlas.web.cern.ch/Atlas/GROUPS/INNER_DETECTOR/TDR/tdr.html

[27] ATLAS Collaboration. *ATLAS Muon Spectrometer Technical Desing Report.* CERN/LHCC/97-22, ATLAS TDR 10, (1997).

[28] ATLAS Collaboration. *ATLAS Detector and Physics Performance Technical Desing Report.* CERN/LHCC/99-124 (1999).

[29] W. Blum,*ATLAS Internal Note*, MUON-NO-24 (1993).

[30] D. Drakoulakos et al., XTOM2, Stereo-Measurements of the MDT Muon Chambers using high precision X-ray Tomograph. *ATLAS Note*, MUON-NO-155 (1997).

[31] V. Paschhoff and M. Spegel, Aging studies for the ATLAS MDTs using Ar-$CO_2$,*ATLAS Note*, ATL-MUON-2000-004 (2000).

[32] H. Groenstege, The RASNIK/CCD 3D alignment system. ATL-MUON-94-063.

[33] E. Duchovni et al. Possible Utilization of Thin-Gap-Chambers in the ATLAS Muon System; ATLA-MUON-93-023

[34] K. Nagai, Nucl. Instr. Meth. A 384 (1996) 219.

[35] V. Smakhtin, Nucl. Instr. Meth. A 494 (2002) 500-503.

[36] R. Santonico and R. Cardarelli, Nucl. Instr. Meth. 187 (1981) 377-380.

[37] R. Santonico and R. Cardarelli, Nucl. Instr. Meth. A 263 (1988) 20-25.

[38] W. Blum and L. Rolandi, *Particle Detection with Drift Chambers*, Springer, 1993.

[39] V.V. Parkhochuck et al., Nucl. Instr. Meth.93 (1971) 269.

[40] H.A. Bethe, Z. Physik, 76:293, 1932.

[41] K. Hagiwara et al., Physical Review. D 66 (2002).

[42] Particle Data Group, http://pdg.lbl.gov

[43] L.D. Landau, J. Exp. Phys. (URSS), 8:201, 1944.

[44] H. Raether, *Electron Avalanches and Breakdown in Gaseous*, London Butterworths, 1964.

[45] K. Kleinknecht *Detectors for Particle Radiation*, Cambridge University Press, 1986.

[46] S. Ramo, Proc. IRE 27 (1939) 584.

[47] W. Riegler, Nucl. Instr. and Meth. A491:258-271, 2002.

[48] G. Aielli et al., Nucl. Instr. and Meth. A508:6-13, 2003.

[49] H. Genz, Nucl. Instr. and Meth. 112 (1973) 83.

[50] A. Colucci et al, Nucl. Instr. and Meth. A425:84-91, 1999.

[51] P. Camarri et al, Nucl. Instr. and Meth. A414:317-324, 1998.

[52] V. Golovatyuk et al, Nucl. Instr. and Meth. A461:96-97, 2001.

[53] H.J. Hilke, Nucl. Instr. and Meth. A252:169-179, 1986.

[54] E. Marotta et al., J. Mass Sprctrom. 2004; 39:791-801.

[55] *NIST Chemistry WebBook*, Standard Reference Database Number, 69, June 2005. http://webbook.nist.gov/chemistry.

[56] http://www.caen.it/nuclear/products.php.

[57] B. René, http://root.cern.ch

[58] C. Chiri, Tesi di Lauea, Universita' di Lecce.

[59] I. Crotty et al., Nucl. Instr. and Meth. A360 (1995) 512-520.

[60] G. Aielli et al., IEEE Trans. Nucl. Sci. 53: 567-571, 2006.

[61] E.C. Zeballos et al., Nucl. Instr. and Meth. A396 (1997) 93-102.

[62] V.V. Ammosov et al., *Comparison between 2mm and 3.5 mm gap RPCs operated at low gas gain*, September 1996, Protvino, Russia.

[63] M.G. Alviggi et al., ATLAS Internal Note MUON-NO-131, 1 October 1996.

[64] F. Sauli, Nucl. Instr. and Meth. A553 (2005) 18-24.

[65] J. Va'vra, Nucl. Instr. and Meth. A371 (1996) 35-56.

[66] A. Buzulutskov et al., Nucl. Instr. and Meth. A443 (2000) 164-180.

[67] A. Bondar et al., Nucl. Instr. and Meth. A574 (2007) 493-299.

[68] A. Aloisio et al., Nucl. Instr. and Meth. A 435 (2004) 256-271.

[69] G.Aielli et al., Nucl. Instrum. and Meth. A409 (1998) 291-293.

[70] F. Giannini et al., Nucl. Instr. and Meth. A432 (1999) 440.